DISSERTATION | DOCTORAL THESIS

Titel | Title

Atmospheric retention distances: Finding planetary systems suitable to host rocky planets with atmospheres

verfasst von | submitted by

Gwenaël Van Looveren BSc. MSc. MSc.

angestrebter akademischer Grad | in partial fulfilment of the requirements for the degree of

Doktor der Naturwissenschaften (Dr.rer.nat.)

Wien | Vienna, 2025

Studienkennzahl lt. Studienblatt | Degree programme code as it appears on the student record sheet:	UA 796 605 413
Dissertationsgebiet lt. Studienblatt | Field of study as it appears on the student record sheet:	Astronomie
Betreut von | Supervisor:	Ass.-Prof. Dr. Sudeshna Boro Saikia Univ.-Prof. Dipl.-Phys. Dr. Manuel Güdel Ass.-Prof. Dr. Kristina Kislyakova PhD

“For a long while they sang only each alone, or but few together, while the rest hearkened; for each comprehended only that part of the mind of Ilúvatar from which he came, and in the understanding of their brethren they grew but slowly. Yet ever as they listened they came to deeper understanding, and increased in unison and harmony.”

- **J. R. R. Tolkien**, “The Silmarillion”

To those with their hearts set on a dream,
even though the road can be rough,
don't give up, you'll get there,
just be stubborn.

Kurzfassung

Bis heute ist die Erde mit ihrer Fähigkeit, Leben zu ermöglichen, ein scheinbar einzigartiger Planet im bekannten Universum. In dieser Arbeit untersuche ich Faktoren, die zur Entstehung des uns bekannten Lebens beitragen, sowie Aspekte der Habitabilität. Ein solcher Aspekt ist die Habitable Zone (HZ), traditionell definiert durch den Entfernungsbereich, in welchem die Oberflächentemperatur flüssiges Wasser erlaubt. Der Aggregatzustand des Wassers hängt jedoch auch vom Druck ab, was oft vernachlässigt wird.

Das Ziel meiner Arbeit ist es, den Verlust von Planetenatmosphären zu untersuchen und die daraus resultierende Verringerung des Atmosphärendrucks. Dies geschieht anhand eines Rasters von Modellen der oberen Atmosphäre, berechnet mit dem selbstkonsistenten thermochemischen Code Kompot. Die Modelle decken einen breiten Bereich von Planetenmassen, chemischen Zusammensetzungen der Atmosphäre und stellaren Strahlungsflussdichten ab. Für jede Parameterkombination kann der thermische atmosphärische Verlust berechnet werden, um zu bestimmen, welche Planeten eine Atmosphäre über eine längeren Zeitraum halten können. Diese Modelle zeigen dass Planeten mit höherer Masse und einem höheren CO_2-Mischungsverhältnis ihre Atmosphäre leichter halten können. Noch wichtiger ist, dass die Modelle es uns ermöglichen, die höchste stellare Strahlungsflussdichte zu bestimmen, die ein Planet aushalten kann, bevor er eine katastrophale Massenverlustrate für die Atmosphäre erreicht.

Anhand von Evolutionsmodellen der der stellaren Leuchtkraft und Strahlungsflussdichte, bei denen der katastrophale Verlust erreicht wird, definiere ich die Atmospheric Retention Distance (ARD). Planeten, die sich innerhalb dieser Grenze befinden, behalten ihre Atmosphäre höchstwahrscheinlich nicht. Die Evolutionsmodelle decken ein breites Spektrum an Sternmassen und anfänglichen Rotationsraten ab. Mit diesen beiden Modelltypen berechne ich die ARD für verschiedene Sterntypen und vergleiche sie mit der HZ. Daraus schließe ich, dass sich ARD und HZ nur bei Sternen mit Massen über 0,4 Sonnenmassen überschneiden. Weiters deuten die Modelle darauf hin, dass die Überlappung zwischen HZs und ARDs durch die anfängliche Rotationsrate der Sterne zusätzlich verkompliziert wird. Sterne mit einer höheren anfänglichen Rotationsrate benötigen länger, um ihre Rotation zu reduzieren. Bei Sternen mit geringerer Masse im Raster kann eine hohe anfängliche Rotationsrate dazu führen, dass sich ARD und HZ erst mehrere Milliarden Jahre später überlappen.

Im zweiten Teil meiner Arbeit untersucht Möglichkeiten die Berechnung von Atmosphärenmodellen zu beschleunigen. Die hier vorgestellte Lösung kombiniert neuronale Netze mit Atmosphärenmodellen, um sowohl eine höhere Berechnungsgeschwindigkeit als auch eine bessere physikalische Genauigkeit zu erzielen. Durch den Einsatz einer Kaskade neuronaler Netze kann das thermische Profil der Atmosphäre geschätzt werden. Diese Schätzung dient dann als Ausgangspunkt für die Berechnung des vollständigen chemischen und thermischen Profils, das der stationären Lösung deutlich näher kommt und somit weniger Iterationen erfordert. Tests dieses Ansatzes zeigen, welches er die Berechnungszeiten um den Faktor 1,2 bis 2 reduzieren kann.

Abstract

Up to the present day, the Earth is a seemingly unique planet in the known Universe with its ability to support life. In this thesis, I explore factors that contribute to the formation of life as we know it and aspects of habitability. The Habitable Zone (HZ), traditionally defined by the range of distances where the surface temperature is suitable for liquid water, is one such aspect. However, the phase of water also depends on pressure, which is often overlooked.

The aim of this work is to explore atmospheric loss and the consequent loss of pressure. This is done through a grid of model upper atmospheres calculated using the self-consistent thermo-chemical code Kompot. The grid covers a range of planetary masses, atmospheric compositions, and irradiances. For each combination of parameters, the thermal atmospheric loss can be calculated to determine which planets can hold onto an atmosphere. These models show, unsurprisingly, that planets with a higher mass and a higher CO_2 mixing ratio retain their atmospheres more easily. More importantly, the models allow us to determine the highest irradiance a planet can endure before reaching a catastrophic mass loss rate.

Through evolution models of a star's luminosity and the irradiances where the catastrophic loss is reached, I define the Atmospheric Retention Distance (ARD). Planets closer in than this distance are unlikely to retain their atmosphere. The evolution models cover a wide range of stellar masses and initial rotation rates. With these two types of models, I calculate the ARD for different types of stars and compare them to the HZ. From this, I conclude that the ARD and HZ only overlap for stars with masses larger than 0.4 solar masses. Additionally, the models indicate that the overlap between HZs and ARDs is further complicated by the initial rotation rate of the stars. Stars with a higher initial rotation rate need longer to spin down. For lower mass stars in the grid, a high initial rotation rate can cause the ARD and HZ to only overlap gigayears later.

A second part of this work looks at ways to accelerate the calculation of atmospheric models. The solution I present here combines the use of neural networks with atmospheric models to achieve both speed and physical accuracy. By using a cascade of neural networks, the thermal profile can be estimated. This estimate is then used as a starting point to calculate the full chemical and thermal profile, which is much closer to the steady-state solution, thus requiring fewer iterations. Tests of this approach show that it can reduce calculation times by a factor of 1.2 to 2.

Table of Contents

Acronyms

ARD	Atmospheric Retention Distance
DEM	Differential Emission Measure
EUV	Extreme ultraviolet
GCM	Global Circulation Model
GPU	Graphics Processing Unit
HZ	Habitable Zone
IR	Infrared
JWST	James Webb Space Telescope
XUV	X-ray and ultraviolet

Declaration of published work and thesis synthesis

This doctoral thesis is a result of the work I carried out in the course of my PhD at the University of Vienna. My work resulted in two first-author publications and conference proceedings. Therefore, parts of this thesis overlap with published work. The list below summarises which Chapters were based on which published or submitted works. Together with the published work, this dissertation includes yet unpublished results and analysis.

- The work presented in chapter 3 was carried out in collaboration with Manuel Güdel, Sudeshna Boro Saikia, and Kristina Kislyakova and has been published as: "Airy worlds or barren rocks? On the survivability of secondary atmospheres around the TRAPPIST-1 planets" in A&A (Van Looveren et al. 2024).

- The work presented in chapter 3 was carried out in collaboration with Sudeshna Boro Saikia, Oliver Herbort, Simon Schleich, Manuel Güdel, Colin Johnstone, and Kristina Kislyakova and has been published as: "Habitable Zone and Atmosphere Retention Distance (HaZARD) Stellar-evolution-dependent loss models of secondary atmospheres" in A&A (Van Looveren et al. 2025).

- The work presented in chapter 4 was carried out in collaboration with Axinya Tokareva as part of her Master's thesis (Tokareva 2024) and will be published in an upcoming work.

Gwenaël Van Looveren
Vienna, April 2025

Chapter 1

Introduction

"Observe the light and consider its beauty. Blink your eye and look at it.
That which you see was not there at first, and that which was there is there no more."

\- **Leonardo da Vinci**

1.1 Atmospheres

Most people have asked or have been asked: "Why is the sky blue?" (or green, depending on the language you speak). The usual answer to this question in our time is that air is made up of nitrogen and oxygen. A particularly inquisitive person might continue asking how the evening and morning sky are red then. This draws out the more complicated answer that different wavelengths, or colours, are scattered differently by the particles in the air. Longer wavelengths, such as red light, are less affected by scattering by air particles than the shorter wavelengths. When the Sun is close to the horizon, the light passes through more air and more of the 'blue' light is scattered away by the time it reaches us. This seemingly simple question illustrates that the air we breathe and the sky we look up to are complex and not only impact but also form the world we know today. In this introductory chapter, using 'why' and 'how', we will build up the components required to study Earth's air and the atmospheres of other planets.

Let us start with a more formal definition of an atmosphere: a layer around a celestial body made primarily of material in the gaseous state. As with many definitions in astronomy, this definition can be rather loose as it also includes concepts such as stellar atmospheres. Though they share many processes, this work focuses on planetary atmospheres. Looking at the Solar System, we can already see many different types of atmospheres. Mercury, the closest planet to the Sun, has an extremely thin atmosphere composed mostly of particles from the solar wind (Leblanc et al. 2007). In comparison, Venus forms a stark contrast with its very dense CO_2 atmosphere (e.g Limaye et al. 2017). The third planet in the Solar System is Earth, which has an atmosphere dominated by N_2 and O_2 (e.g. Lammer et al. 2019). Mars is again characterised by a thin CO_2 atmosphere (e.g. Franz et al. 2017).

Moving away from the rocky inner planets, we find the two gas giants in the Solar System: Jupiter and Saturn. These two planets are primarily made up of hydrogen and helium. However, several moons orbiting these planets also have interesting atmospheres, in particular, Titan with its N_2 and CH_4, and Io with its tenuous SO_2 atmosphere. Lastly, we find the so-called ice giants Uranus and Neptune. A lower temperature and hydrogen, helium and methane composition characterise these planets' atmospheres. These differences in composition and density reflect the various formation and evolutionary paths planets follow.

1.1.1 Planet formation

First, to understand the different types of atmospheres, we must take a quick look at how planets are formed. It is believed that planets form through one of two processes: gravitational instability and pebble accretion (e.g. review by Drążkowska et al. 2023). In the gravitational instability scenario, planets are believed to form in a manner similar to stars. When a molecular cloud collapses, gravity pulls the material of the cloud together, forming an increasingly heavy object. When enough material is gathered, the pressure due to gravity can cause the fusion of light elements, such as hydrogen or lithium atoms, to ignite, creating a star. If such an instability does not gather enough material to start fusion, it can form a giant planet instead (Mayer et al. 2002). It is believed that this pathway leads to planets with at least several times the mass of Jupiter. This mechanism is believed to explain super-Jupiters at wide separations (Schlaufman 2018). Planets formed through gravitational instability are believed to have atmospheric compositions similar to those of their host star and be dominated by hydrogen and helium.

The second pathway to form planets is through pebble accretion. For the purposes of this work focused on atmospheres, we will only look at several points of pebble accretion which influence atmospheres. For a more in-depth review of various theories and complications related to pebble accretion, we refer the reader to Drążkowska et al. (2023). When the star is still accreting mass, a disc is formed around it from the material of the molecular cloud due to the conservation of angular momentum. This so-called protoplanetary disc gathers material in a plane where it can collide and grow into grains, pebbles, and planetesimals. These planetesimals grow in mass and continue to collect more pebbles through their increasing gravity to form the building blocks of future planets. When such a planetesimal reaches a high enough mass before the star ignites, the gaseous material of the disc will become gravitationally bound to this planetary embryo. The gaseous material will cause a feedback loop where the mass of the nascent planet increases, causing a stronger pull on nearby material. This runaway growth allows planets to grow rapidly as long as there is gas in the disc. Depending on the availability of solids, location in the disc, and the time until the star disperses the gas, planets can grow from a fraction of Neptune's mass to several times Jupiter's mass in this way (e.g. Pollack et al. 1996; Piso & Youdin 2014). This formation path leads to atmospheres composed predominantly of hydrogen and helium, as these are the most abundant components of the disc.

The third category of planets of interest here is the rocky planets. These planets are also believed to have formed through pebble accretion. When the forming planet does not reach the mass required to hold onto a large envelope of hydrogen and helium by the time the star dissipates the gas, only the solid core is left. These planets can keep on growing after the dissipation of the gas in the disc (Raymond et al. 2009; Ogihara et al. 2018). Stökl et al. (2016) discuss how a core of one Earth mass could hold onto a thin primordial atmosphere. These hydrogen atmospheres, even if eventually lost, can influence these rocky planets by, for example, insulating the core. This can allow the planetary core and the magma ocean to remain hot for much longer (Kite & Barnett 2020). The primordial atmosphere can also act as a reservoir, since it is made up of lighter particles and thus depletes before the heavier particles of the secondary atmosphere are lost. This will be discussed in more detail in Chapter 3. Hydrogen-dominated atmospheres around rocky planets with magma oceans could also prove to be important in the formation of water (Young et al. 2023). The high pressure caused by a primary atmosphere can also help dissolve volatiles (such as water) into the magma ocean (Dorn & Lichtenberg 2021). The additional volatiles in the core could result in variations of radii up to 16%, which become particularly important when distinguishing different types of planets using bulk densities, as we will see in Section 1.1.2.

The location where a planet forms is also believed to have an impact on the composition of the planet and its atmosphere (e.g. Öberg et al. 2011). During the protoplanetary disc phase, various types of ices will form at different distances. If, for example, a planet forms within the water snow line, it would have a C/O ratio similar to its host star, as most ices are in the gas phase. If, on the other hand, a planet forms beyond the water snow line, it would have a higher C/O ratio because a part of the O reservoir is captured in the water ice. Unfortunately, as with most science, reality is not that simple. The star's evolution during the protoplanetary disc phase can move the location of the snow lines whilst the planets are forming (Eistrup et al. 2018). The snow lines are also sensitive to the opacities of the dust in the disc, adding an additional layer of uncertainty (Min et al. 2011). Finally, the pebbles, planetesimals, and planets can also migrate through the system, further mixing these ratios. Though we will not discuss the formation of planets in this work in depth, it is good to keep in mind that the different processes occurring during the disc phase can influence the initial conditions of the planets and the atmospheres we study here.

1.1.2 The exoplanet zoo

In the previous section, we discussed how very different types of planets can emerge. In our solar system, we see several examples of different types of planets, such as the gas giants and rocky planets. The solar system and its particular structure have long been the only reference to determine how planetary systems form. It was long believed that a planetary system would have its smaller rocky planets closer to the star, whilst larger planets would form farther out where the influence of the star is less and they could accumulate more material. Many models have been proposed for the origin of the Solar System, most famously the Nice model (e.g. Tsiganis et al. 2005; Morbidelli et al. 2007). This model demonstrates how much planets can migrate and disrupt other planets during the early phases of the solar system.

Struve (1952) proposed that Jupiter-sized planets could orbit their host stars much closer than our Solar System giant planets. These planets would cause a measurable shift in the radial velocity of the star. In 1995, such a planet was discovered to orbit around the star 51 Pegasi (Mayor & Queloz 1995). This planet, named 51 Peg b, has a mass of about 0.46 times the mass of Jupiter and is only 0.0527 au away from its star. Due to its proximity to its star, the planet is very hot and is estimated to have nearly twice the radius of Jupiter. This planet demonstrates that not all stellar systems are as neatly organised as the Solar System and that there are different types of planets for which we do not have a Solar System equivalent.

Figure 1.1 shows the semi-major axis and planetary masses of confirmed exoplanets. At the top of this figure, we can see the Brown Dwarfs, the most massive objects falling short of the mass required for hydrogen fusion. Next, the figure demonstrates that planets like 51 Peg b are not rare and form a particular type of planet called Hot-Jupiters. These planets tend to have larger radii than Jupiter and are more 'puffy' due to their proximity to their host stars. The higher irradiation of the star can also cause chemical changes in the atmospheres of these planets. Though we will not focus on these types of planets in this work, a lot of the effects we will discuss in the following chapters also apply to these hot giant planets, though often to lesser degrees. Further out in the high-mass range, we can see the classical giant planets. This category includes planets similar to Jupiter and Saturn. Though still dominated by hydrogen and helium, these planets tend to be denser than the previous category, as they are cooler.

Going towards lower masses, we find the category of sub-Neptunes. This group of planets, contrary to what its name would imply, consists of planets that are roughly the mass and or size of Neptune, though the exact boundaries of this category are still up for debate. These planets are characterised by densities that would imply the presence of large amounts of hydrogen, leading us to believe that they have a similar structure to Uranus and Neptune. Unfortunately, density measurements provide but a glimpse into the very complicated question of 'what are these planets made of'. Many assumptions need to be made to estimate the size and composition of different layers of the planet. A simple example of this would be a solid core made up of accreted planetesimals, an icy mantle, and a hydrogen/helium envelope. Additions of various states and compositions of these layers have been suggested, with some exotic suggestions like diamond rain (Kraus et al. 2017). Another proposed structure is that of the hycean (hydrogen-ocean) worlds (Madhusudhan et al. 2021). In this proposed scenario, rather than an icy mantle, the planet would have an extensive ocean underneath its hydrogen-dominated atmosphere. On the other hand, less organised structures have been proposed, where rather than well-defined layers, the planet would be composed of a large, miscible, diffuse interior, similar to the interior of Jupiter (Wahl et al. 2017). Returning to Figure 1.1, it is also interesting to note the relatively empty area of close-in Neptune-sized planets. This area is called the sub-Neptune desert (e.g. Fulton & Petigura 2018). These planets are believed to be close enough to their host star whilst not having enough mass, resulting in significant mass loss (see Section 1.3.2).

Lastly, there is the category of rocky planets. These planets are defined by high densities, indicating a composition of mostly solids. Just as in the Solar System, these come in a wide variety, ranging from farther-out planets like Mars, to planets irradiated many times more than Mercury. Within this latter group, a sub-category called lava planets has been proposed, which are so hot they maintain a molten surface (Henning et al. 2009). These planets could harbour unusual atmospheres made up of the vapour of rocks for which we have no equivalent in the Solar System. Rocky planets are of particular interest with regard to habitability, as the one example of life we know of occurs on a rocky world. In Section 1.3, we will look at the conditions for habitability in detail.

Throughout the previous sections, the density of the planet has emerged as an important parameter to distinguish between rocky planets and those with large hydrogen atmospheres. In Figure 1.2, we can see the distribution of the planetary radii. From this figure, we can see that planets with roughly Earth's radius are the most common size of planet. Going to larger radii, we can see a small decrease in the number of planets around 1.6 $R_\oplus$. This is followed by an increase in the number up to about 2.5 $R_\oplus$. This decrease has received several names but is usually described as the radius valley. Several reasons have been suggested for this dip in the distribution, from differences in the formation (Venturini et al. 2020), to photoevaporation (Owen & Wu 2016) or combinations of several effects. Figure 1.1 already demonstrated that there are very few close-in sub-Neptunes. Before we look into how atmospheres are lost, let us take a look at their formation.

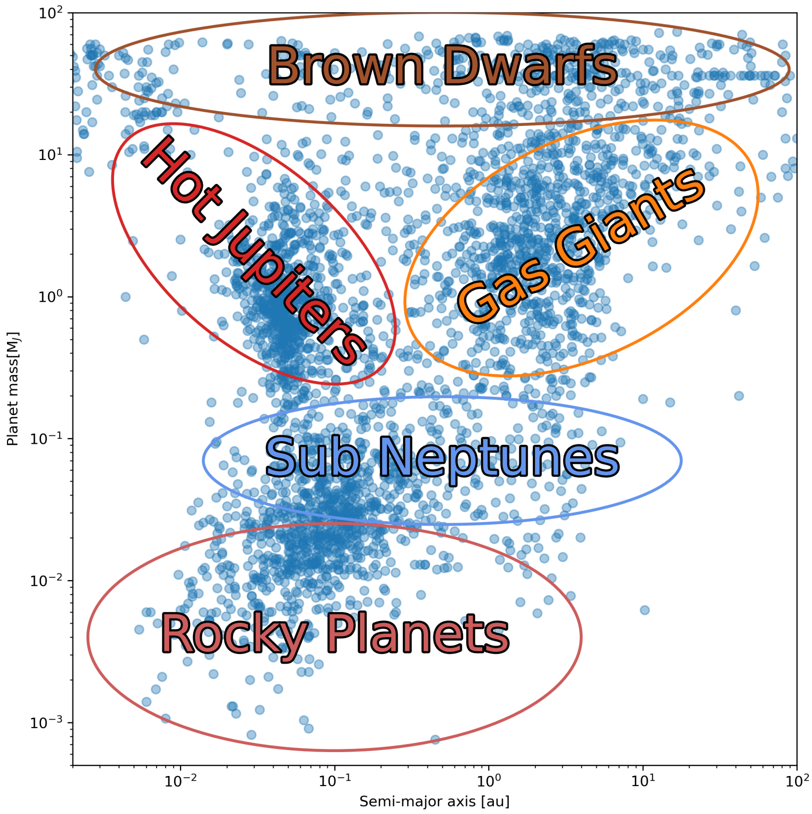

Figure 1.1: The semi-major axis against the planetary mass of confirmed exoplanets as retrieved from exoplanet.eu on 13/12/2024. This figure indicates the loosely defined parameter space that several types of exoplanets cover.

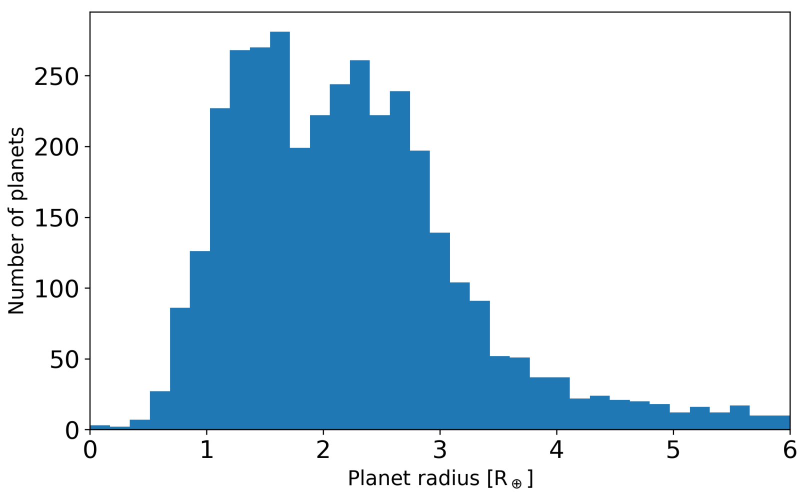

Figure 1.2: The distribution of radii of confirmed exoplanets as retrieved from exoplanet.eu on 13/12/2024. This figure demonstrates a noticeable gap in the number of planets around 1.6 Earth radii.

1.2 Atmospheric formation

1.2.1 Primordial atmospheres

Primordial atmospheres are atmospheres made up primarily of hydrogen and helium. As we already saw in Section 1.1.1, they are formed during the disc phase of a young stellar system when a planetary embryo gravitationally binds gas from the protoplanetary disc. The lifetime of a protoplanetary disc is typically 1-10 Myr, though it can be longer (Pfalzner et al. 2014). The lifetime is the main constraint on how much material a planetary core can accumulate. Stökl et al. (2016) show in their work how only planetary cores above 4-5 Earth masses experience runaway growth, where the planet grows rapidly. The same study also shows that even planetary cores as small as 0.5 $M_\oplus$ could hold onto some of the gas from the disk. The authors argue that if atmospheric losses are taken into account, these models fit the observational analysis by Rogers (2015), which places the difference between rocky planets and sub-Neptunes at 1.6 $R_\oplus$. These primordial atmospheres could play a crucial role in the evolution of rocky planets, even if they are short-lived.

In the Solar System, the 4 outer planets have primordial atmospheres. The masses of these planets range from 14.5 $M_\oplus$ for Uranus to 318 $M_\oplus$ for Jupiter. These planets also have semi-major axes ranging from 5.2 au (Jupiter) to 30 au (Neptune), making all of these planets rather cool. The first detection of an atmosphere around an exoplanet was of a Hot-Jupiter (Charbonneau et al. 2002). Since then, more atmospheres and different chemical species have been found around various types of giant planets (e.g Swain et al. 2008; Macintosh et al. 2015; JWST Transiting Exoplanet Community Early Release Science Team et al. 2023; Tsai et al. 2023; Edwards et al. 2023, just to name a few). Gas giants have been a prime target for atmospheric characterisation due to their extended atmospheres. Of particular interest are close-in giant planets as their high temperature causes the atmosphere to expand or even be lost in a cometary-like tail (see Section 1.3.2). Though in this work we will not focus on this type of atmosphere, we will often return to it since they have been observed and can provide us insights into processes that influence planets and their atmospheres in ways for which we have no examples in our Solar System.

1.2.2 Secondary atmospheres

Secondary atmospheres are a kind of atmosphere made up predominantly of species heavier than hydrogen and helium. The exact composition of a secondary atmosphere can vary greatly. On Earth, for example, we have an atmosphere composed mostly of N_2 and O_2, whereas Venus and Mars have atmospheres rich in CO_2. A very different kind of secondary atmosphere composed of N_2 and CH_4 can be found around Titan, Saturn's largest moon. But let us take a step back and first look at how these atmospheres come about.

The main pathway for a secondary atmosphere to form is through outgassing. When a planet accretes its solid materials, gaseous elements can get trapped in rocks or dissolve into magma. During the early stages of a planet's life, the interior and surface of the planet tend to be very hot, leading to magma oceans and liquid mantles. Gases dissolved into these liquid parts can escape the melt through evaporation. Throughout the solidification of the magma ocean, a layer of volatiles of tens to thousands of bars can build up (Elkins-Tanton 2008).

The precise composition and thickness of such an atmosphere depend on the composition of the planet and the depth of the magma ocean (as summarised in Lammer et al. 2018). These in turn depend on several other factors such as the amount of radiogenic species or the number of impactors (Lebrun et al. 2013). This can result in the buildup of several tens to hundreds of bars. On Earth, for example, the solidification of the magma ocean is estimated to have resulted in 70 bar of CO_2 (Gebauer et al. 2020), an atmosphere much more comparable to current Venus.

After the solidification of the magma ocean, planets can continue to outgas over longer periods of time through volcanism, which requires the mantle of the planet to remain above the melting point. The heat needed to drive volcanism can continue to come from radiogenic species or tidal heating. On Earth, measurements of volcanism show that the material outgassed from magma is usually composed of H_2O, CO_2, CO, and in much smaller amounts N_2 and CH_4. On Earth, the current outgassing rates from volcanism provide 1.0×10^4 kg/s (7.5 Tmol/yr) of CO_2 and 5.4×10^4 kg/s (95 Tmol/yr) of H_2O (Catling &

Kasting 2017, p. 203). When discussing volcanism, Jupiter's moon Io must also be mentioned. In this moon we can observe volcanism driven by tidal heating (e.g. Tyler et al. 2015), which is also thought to be an important source of heating in close-in rocky planets (Jackson et al. 2008). Io is particularly interesting as, even though the radius of the moon is about a quarter of Earth's, its volcanoes outgas SO_2 at approximately 10^4 kg/s (Lopes & Spencer 2007), a rate comparable to that of Earth.

It is important to note that not every atmospheric composition is likely or even possible to form. Species associated with outgassing are, of course, some of the most likely species to be present in secondary atmospheres, but we can try to limit the possible atmospheric compositions even more. When the surface of a rocky planet heats up, particles will escape into the gas phase, slowly forming an atmosphere. To calculate the number of particles that will end up in the gas phase, we can make use of partial pressure or fugacity if we go beyond the assumption of an ideal gas. Using the planet's temperature and the composition of rocks, the possible atmospheric compositions can be estimated (e.g. Miguel 2019; Herbort et al. 2020). These works show how atmospheres can be very different from solar system atmospheres, in particular, those of lava worlds, which are theorised to have mineral atmospheres. The partial pressures can also inform us as to which clouds can form on exoplanets (e.g. Herbort et al. 2022). Just as we define the humidity on Earth, we can determine when and at what altitude other species reach supersaturation and form condensates. This is particularly important in transmission spectroscopy as we will see in Sections 1.5 and 2.2.

There are other hypotheses that discuss the origin of the volatile content of Earth, and in particular the presence of water, that can skew the composition and amount of volatiles. Studies such as Li (2022, and references therein) show the complicated and uncertain nature of these theories. Though these different pathways are very interesting, they are difficult to study for Earth, extremely so for other Solar System planets, and nigh impossible for exoplanets. Within this work, we will group these effects together with the solidification of the magma ocean as an initial condition.

1.3 Habitability

Now that we have looked at different types of planets and atmospheres, we can have a closer look at what we can "do" with these planets. A very interesting reason to look at planets and their atmospheres (in my personal and very biased view) is habitability. In its broadest sense, habitability is defined as being "able to support life". This definition immediately raises the follow-up question: How do you define life? Do we mean humans, more broadly animals, or perhaps plants or even bacteria, or perhaps something completely different and truly alien? This philosophical question has been tried to be answered on many occasions (e.g. Cleland & Chyba 2002; Ruiz-Mirazo et al. 2004; Benner 2010b), but here we will focus on some of the building blocks required for life. Several arguments can be made to narrow down the wide array of possible building blocks required for life and where to look for them. These arguments can be ordered according to how stringent the requirement is for life. Benner et al. (2004) summarise these requirements concisely from thermodynamic disequilibrium to the solvent. The solvent is of particular interest in this work, so let us have a closer look at this point.

First of all, having a solvent is important for life as it facilitates chemistry, allowing the formation of the needed chemical components such as amino acids. On Earth, the most important solvent for life is liquid water. Water has many interesting properties that have been proposed to be useful for the development of life. For example, water is polar, which allows it to be miscible with many other strongly polar molecules. The hydrophobic effect also facilitates the formation of cell membranes. Perhaps one of the properties of water which makes it stand out above other molecules is the fact that ice expands and floats. This rather peculiar property means that ice floats upwards, forming an insulating layer that prevents deeper layers from freezing over. On present-day Earth, we can see how fish survive in lakes that completely freeze over during winter months. In Earth's older history, we can also see how life survived several periods of global glaciation, the so-called snowball Earth periods, likely due to this property (McKay 2000; Corsetti et al. 2003).

Other solvents which have been proposed as suitable to support life include polar solvents like ammonia and sulfuric acid, or non-polar solvents like hydrocarbons. The latter is of particular interest in the context of Saturn's moon Titan, which has lakes composed primarily of methane (Stofan et al.

2007). Though these solvents would theoretically provide many of the properties we believe water provides for the formation of life, they also have their shortcomings. For example, in solvents with weak hydrophobic properties, like ammonia and hydrocarbons without hydroxyl functional groups, the formation of membranes that divide the life form from its environment is more complicated. This could be circumvented through the addition of a hydroxyl functional group, turning our methane into methanol, for example. However, polarity is not necessarily a positive property. The high reactivity of water actually destroys RNA and DNA (Frick et al. 1987; Benner 2010a). On the other hand, the weak hydrogen bonds of these species result in lower boiling temperatures (e.g. methane at 109 K, ethane at 184 K, ammonia at 240 K). As discussed at length in Chapter 6 of Council (2007), many of these negative attributes might only be perceived as negative due to our geocentric biased view of life.

1.3.1 Habitable zone

Though these discussions of truly alien forms of life beyond Earth-like life are very interesting, let us indulge in this geocentric bias and focus on liquid water. The presence of liquid water on the surface of a planet has led to the definition of the circumstellar habitable zone (Kasting et al. 1993). A lot of factors go into the precise calculation of the habitable zone and require complicated models to accurately model these. Both 1D (Kopparapu et al. 2013) and 3D (Kopparapu et al. 2016) climate models have been used to determine the range of orbital distances over which liquid water could be present, given certain conditions. The inner edge of the habitable zone is usually defined through criteria such as runaway greenhouse, a scenario in which oceans would evaporate entirely (Kasting 1988). On the other hand, the outer edge is defined as the furthest point where CO_2 can keep the surface temperature above 273 K. Both of these calculations are influenced by the incoming radiation from the star, the albedo of the planet, the greenhouse gases present in the atmosphere, or cloud coverage, just to name a few. Within the Solar System, the inner boundary has been determined to be anywhere between 0.38 au (Zsom et al. 2013) and 0.99 au (Kopparapu et al. 2013), while the outer boundary has been determined to be anywhere between 1.004 au (Hart 1979) and 10 au (Pierrehumbert & Gaidos 2011). The inner boundaries strongly depend on the received radiation and the species in the atmosphere that absorb this radiation. The species most often taken into consideration are H_2O and CO_2. Of course, the choice of absorption bands and efficiency can strongly influence where the exact boundary falls (Kopparapu et al. 2013). The outer boundary also relies strongly on the incoming radiation, but in this case, we want to hold onto as much heat as possible to keep the surface water from freezing. Because of this, greenhouse gases and cloud coverage play an important role in the determination of the outer boundary.

Beyond looking at the Solar System, there are many other factors that could influence whether or not a planet can sustain liquid surface water. Since the boundaries of the habitable zone depend strongly on the radiation the planet receives, also called insolation in the Solar System or instellation more generally, we can easily see how the details of the host star are also very important. The first parameter we could look at is the spectral type, effective temperature, or stellar mass. For main sequence stars, these parameters are closely related. We will use these classifiers throughout this work somewhat interchangeably, as is common in the field of exoplanet research, even though they are strictly not interchangeable. Wherever this is not the case, we will highlight why it might not be the case. It has long been theorised that high-mass stars would not provide a favourable environment for life due to both the relatively short time they spend on the main sequence compared to the time-scales required for the formation of life and their brightness at shorter wavelengths (e.g. Huang 1959). Sun-like stars have naturally been favoured in discussions on habitability since all (i.e. one) examples of life we know of occur around these types of stars. On the low end of the mass spectrum, we find late K and M-type stars. These stars have gained a lot of attention in exoplanet research due to observational biases towards smaller stars (see also Section 1.5). The habitable zone of these low-mass stars is much closer to the host star, which can cause these planets to become tidally locked, which can also strongly influence the surface temperatures, extending the habitable zone (Yang et al. 2013). The lowest mass stars have also been of great interest in the search for habitable worlds, as these stars can spend a lot of time in the pre-mainsequence phase (Ramirez & Kaltenegger 2014) and on the order of the age of the universe on the main sequence, giving life, and possibly intelligent life, plenty of time to develop. In Chapter 3 we will focus in particular on stars ranging from Sun-like masses, to the low end of the mass spectrum and discuss whether or not these stars are suitable for habitable worlds.

Outside of the star, the properties of the planet can also influence the habitable zone. One such example is the size of the planet (Kopparapu et al. 2014). Generally speaking, larger planets result in stronger surface gravity, which in turn causes smaller column depths of H_2O and smaller greenhouse effects (Kopparapu et al. 2014). This results in the inner boundary of larger planets being closer to their host star. However, the stronger gravity of larger planets could also prevent the atmosphere from building up (Noack et al. 2017). As already mentioned before, the rotation of the planet, and particularly whether the planet is tidally locked or not, can further move the boundaries of the inner edge of the habitable zone both in- and outwards (Yang et al. 2013; Kopparapu et al. 2016). These are just a few factors that we could, or rather should, take into account when modelling the circumstellar habitable zone.

Though the term habitable zone was first coined by Huang (1959), the specification of a circumstellar habitable zone emphasises the importance of the temperature of the planet and is the most commonly used definition of the term. Other similar definitions have been suggested to expand habitability beyond just the temperature of the planet. One such expansion is the galactic habitable zone, which defines the area around the galactic centre where the metallicity is high enough for terrestrial planets to form and contain enough radioactive elements to sustain planet tectonics, whilst also avoiding regions with large numbers of catastrophic events like supernovae (Gonzalez et al. 2001). A different approach that has been put forward looks at ultraviolet (UV) light from the star to define a UV-habitable zone (Buccino et al. 2006). UV radiation is detrimental to life as it destroys DNA, but it has been theorised that a certain amount of high-energy radiation is required in the formation of biochemical components (Toupance et al. 1977).

This shows that there are many different ways of looking at habitability. However, if we return to focus on liquid water, most research has focused on the thermal aspect of the phase of water. A second parameter that determines whether water can exist in a liquid phase or not is the pressure. The calculations of the habitable zone often assume an atmosphere to be present to provide the required pressure, but when is this assumption actually valid?

1.3.2 To atmosphere or not to atmosphere

Looking at the Solar System, we see that atmospheres are not present in all celestial bodies. By combining this Solar System knowledge with stellar insolation and escape velocity calculations, Zahnle & Catling (2017) defined an empirical law that separates planets with and without atmospheres. This boundary was dubbed the cosmic shoreline and is defined by the power law $I \propto v_{\mathrm{esc}}^4$. This power law neatly separates the Solar System's celestial bodies with an atmosphere from those that are bare rocks. The calculation of this power-law is based on the assumption that atmospheres exist where the gravitational binding energy is high and total stellar insolation is low. Observational evidence of this shoreline for rocky exoplanets has not yet been feasible, but JWST is expected to provide much-needed insights (Kempton & Knutson 2024). However, due to the difficulties in interpreting JWST data of rocky exoplanets, as discussed above, detailed simulations of secondary exoplanet atmospheric escape become an integral piece in solving this puzzle.

In the previous subsection, we already hinted at other factors that influence whether a planet might be habitable or not, such as the chemical composition of the atmosphere. If such factors can influence the temperature on the surface, it is reasonable to assume that there are more factors influencing the presence of an atmosphere than just the escape velocity and the installation. For example, in the upper atmosphere, CO_2 can help radiate away incoming heat, as we will see in Section 2.5. As we have already pointed out in the discussion on habitable zones, tidal locking or, more generally, planetary rotation can also significantly influence the distribution of both heat and clouds. These factors can be both beneficial and detrimental to atmosphere retention. So, in the next section, let us take a closer look at the different mechanisms that can lead to the loss of an atmosphere.

1.4 Atmospheric losses

Atmospheric escape can be divided into three broad categories: thermal escape, non-thermal escape, and impact erosion. The last of these categories is, as the name implies, losses caused by the impact of meteoroids. Due to its inherently unpredictable nature, we will not go into the details of this loss to focus on the other two categories.

1.4.1 Thermal losses

Thermal losses are a type of atmospheric loss characterised by particles which are lost to space due to the thermal energy of the atmosphere. This can happen through either Jeans escape or hydrodynamic losses. On Earth, Jeans escape is estimated to make up 10 to 40% of the total mass loss (Catling & Kasting 2017).

Jeans escape occurs when a particle at the top of the atmosphere has a velocity greater than the escape velocity due to thermal energy. The top of the atmosphere, which we will call exobase in this work, is defined as the region where particles enter a collisionless regime. This can be calculated by determining on the one hand the pressure scale height of a particle, which is the distance over which the pressure in the atmosphere drops by e. On the other hand, we can look at the average distance a particle would travel before colliding with another particle, i.e. the mean free path. The ratio of these two values is the so-called Knudson number:

$$Kn = \lambda_{mfp}/H = \frac{1}{\sigma n} \bigg/ \left(\frac{k_{\mathcal{B}}T}{\mu g}\right) \tag{1.1}$$

In this equation, the mean free path depends on the number density of the particles n, and the cross-section of the particles σ. The pressure scale height term is calculated using the Boltzmann constant $k_{\mathcal{B}}$, the temperature of the gas T, the mass of the particles in the gas μ, and the gravitational acceleration g. Once the mean free path exceeds the scale height, this value will become greater than 1 and the probability of a particle colliding is greatly reduced. This is where we define the exobase.

To determine the number of particles that escape at this altitude, we first need to determine the thermal velocity of the particles (section II.3 of Bauer & Lammer 2004). The velocities of the particles are assumed to follow a Maxwellian distribution, which allows us to calculate the most likely velocity easily:

$$v_{therm} = \left(\frac{2k_{\mathcal{B}}T_{exo}}{\mu}\right)^{1/2}. \tag{1.2}$$

In this equation, T_{exo} is the temperature at the exobase, and $k_{\mathcal{B}}$ is the Boltzmann constant. Note that the equation also depends on μ, the particle's mass. This needs to be calculated for each species present at the exobase to calculate the Jeans escape for a secondary atmosphere accurately. Whether a particle escapes or not also depends on the gravity of the planet. This is represented in the equation of the Jeans parameter, which looks at the ratios of gravitational energy over thermal energy:

$$\lambda_{\mathcal{J}} = \frac{E_{grav}}{E_{therm}} = \frac{GM_p\mu}{R_{exo}k_{\mathcal{B}}T_{exo}}. \tag{1.3}$$

The escape velocity is calculated using the gravitational constant G, the mass of the planet M_p, and the distance of the exobase to the centre of the planet R_{exo}. This parameter has been used as an indicator for catastrophic atmospheric escape. When an atmosphere reaches a Jeans parameter of 1.5, it reaches the so-called blow-off condition identified by Öpik (1963) where the loss can be arbitrarily large regardless of the species' mass.

To calculate the exact Jeans escape flux for a less extreme case, we can use the average velocity of the escaping particles, which scales with the Jeans parameter, and multiply it by the number density of the particles at the exobase n :

$$F_{\mathcal{J}} = v_{therm}\frac{(1+\lambda_{\mathcal{J}})e^{-\lambda_{\mathcal{J}}}}{2\sqrt{\pi}}n. \tag{1.4}$$

Due to the dependence of the Jeans escape on the mass of the particle, lighter particles like hydrogen escape more easily. A consequence of this particle mass dependence is that certain species are lost preferentially. This could be one of the pathways in which a smaller rocky planet loses its primary atmosphere whilst holding onto its heavier outgassed species, as mentioned in Section 1.2.2. Even in less extreme cases, such as present-day Earth, we can see that only hydrogen is lost through Jeans escape (Gronoff et al. 2020). This preferential loss of hydrogen, combined with the dissociation of water (see also Section 2.4.2), results in a dry upper atmosphere. Gronoff et al. (2020) summarise that Earth and Mars lose approximately 1 kg of hydrogen per second through Jeans escape, whilst Venus loses about 10^{-8} kg per second. The reasons for the large difference between these loss rates will be discussed in further depth in Section 2.5.

One might have noticed that the calculation of the Jeans escape assumes that there are no large-scale motions in the atmosphere. If an atmosphere heats up enough, large bulk outflow can occur, which can drag along more massive particles that might not have been lost otherwise. Losses through this method are called hydrodynamic losses. Studies such as Tian et al. (2008) show that an Earth-like atmosphere would become hydrodynamic if it were exposed to an irradiation above five times the Earth's current irradiation. Studies of hydrogen-dominated atmospheres (e.g. Erkaev et al. 2013; Kubyshkina et al. 2018) have shown that even for more massive planets, hydrodynamic mass loss can reach the so-called blow-off state, where entire atmospheres can be lost in less than a million years. In these extreme loss scenarios, planets have been observed to have a comet-like tail in egress of a transit (e.g. Vidal-Madjar et al. 2003; Lavie et al. 2017).

At the start of this section, we have already noted that, even in a quiet scenario such as modern-day Earth, thermal losses only make up a small part of the overall losses, so let us take a closer look at non-thermal losses.

1.4.2 Non-thermal losses

A second type of atmospheric loss is non-thermal loss. This category includes many different processes such as photochemical escape, stellar wind charge exchange, ion pickup and polar outflow. These processes tend to be much more complicated to model due to the interplay of planetary properties and stellar wind properties (see for example summaries such as Gronoff et al. 2020). The dependence on the stellar wind parameters also means non-thermal losses become increasingly important for planets with small orbital distances.

Let us briefly summarise here the different types of non-thermal loss (in no particular order). The first type of loss we will look at is photochemical escape. This loss is characterised by interactions with high-energy photons that cause a photochemical reaction in the upper atmosphere, creating energetic neutral species, ions, and photoelectrons. If the products of the reaction gain enough energy, they can be lost immediately. Alternatively, the ions or photoelectrons created through the reaction can recombine, giving particles enough energy to escape. Modelling this type of escape (e.g. Shematovich et al. 1994) requires the photochemical cross sections to determine the photoionisation, the calculation of the transportation and the reactions involving the products, the reaction rates of the recombinations, etc.

The second non-thermal loss mechanism is sputtering, which occurs when particles from the Sun collide with particles in the atmosphere that then get ejected from the atmosphere. This loss mechanism is particularly important for planets without a global magnetic field (Wang et al. 2014). As shown by, for example, Johnson et al. (2000), the efficiency of the sputtering depends on many factors such as the masses of the incident and target species, their cross sections, and the incident angle, just to name a few. These calculations are usually done using Monte Carlo models.

The next mechanism is charge exchange. This loss mechanism occurs when a charged particle from the solar, or more generally stellar, wind captures an electron from a neutral particle in the atmosphere. The atmospheric particle then becomes charged, trapping it in the magnetic field of the planet if there is one, whilst the now neutral particle from the wind continues along its path, retaining most of its kinetic energy (e.g. Simon et al. 2007; Shematovich & Marov 2018). These particles can either escape with their newly acquired electron or collide with a different particle in the atmosphere, causing sputtering.

The last loss mechanism we will mention is polar outflow. This process, also known as ionospheric outflow, occurs when charged particles in the atmosphere escape along the field lines of a planet's magnetosphere (e.g. Gunell et al. 2018; Kislyakova et al. 2020). These particles can receive energy through suprathermal electrons or heating from wave-particle interaction. As this process depends on the path of particles in regions of the atmosphere where collisions are rare, it is often modelled through Direct Simulation Monte Carlo. These simulations, of course, need information about the number of charged particles in the atmosphere as well as the shape and orientation of the magnetic field compared to the stellar wind (e.g. Presa et al. 2024).

On Earth, charge exchange accounts for 60-90% of all atmospheric loss whilst polar outflow contributes approximately 10% (Catling & Kasting 2017). The wide range in the contribution of these losses can be explained through the strong dependence on the activity of the Sun (Boro Saikia et al. 2020). The geological record of Mars indicates that the red planet experienced stretches of time with significant amounts of surface water, which would require an atmosphere denser than the planet currently retains. Observations from the MAVEN satellite or argon isotope ratios indicate that sputtering removed a significant portion of the atmosphere (Jakosky et al. 2018). Other species, such as oxygen, are lost from the Martian atmosphere primarily through photochemical escape (Lillis et al. 2017). Similarly, Venus Express data shows that the solar wind causes atmospheric loss along the magnetotail (Barabash et al. 2007). The lack of magnetic fields in both Venus' and Mars' cases allows the solar wind to reach much lower altitudes, possibly affecting a larger part of the atmosphere.

In general, magnetic fields of planets were considered to protect atmospheres against these losses (Khodachenko et al. 2012). However, as we see on Earth, the magnetic field adds a path of escape through polar outflow and cusp escape. Works such as Gunell et al. (2018) showed that these additional loss mechanisms can cause planets with magnetic fields to reach similar or even larger losses. Grasser et al. (2023) demonstrated that, also in the case of the Archean Earth, which is also a highly irradiated planet, these losses can strongly affect an atmosphere.

All of these parameters, both on the stellar and planetary side, make it difficult to estimate non-thermal losses. Additionally, determining these parameters is complicated in and of itself. Works such as Turner et al. (2021) and Kislyakova et al. (2014) demonstrate how the planetary magnetic field can be determined. Several studies showed that an upper limit for the stellar wind can be calculated from observations (e.g. Wood et al. 2014; Fichtinger et al. 2017; Kislyakova et al. 2024). These works illustrate the complexity of these measurements and consequently the large uncertainties on non-thermal losses. For this reason, we will focus primarily on thermal losses throughout the rest of this work.

1.5 Observations

Both the US Astro2020 Decadal survey and the ESA Cosmic Vision 2050 have identified the discovery of a secondary atmosphere around a planet as a key priority. With an eye on answering the question of whether we are alone in the universe, rocky bodies in the habitable zone are of particular interest. So let us finish this introduction by looking at the state of observations before diving into the theoretical modelling discussed in Chapter 2.

As already mentioned in Section 1.1.2, some of the earliest observations of exoplanets were of systems with planets either close-in, massive, or both. This is due to observational biases of different detection methods. Planets discovered through radial velocity measurements tend to have large masses, as the planet's gravity needs to have a measurable impact on the star. Additionally, the closer the planet is, the larger the effect will be. For example, Jupiter causes a Doppler shift in the solar spectrum with a radial velocity of 12.4 m/s, whereas Earth results in a radial velocity of the order 0.1 m/s (Mayor et al. 2014). These precisions are difficult to measure, particularly for small planets, where the stellar noise becomes important. The long periods of Jupiter (about 12 years) and the Earth (1 year) would also require long-term observations. Small planets such as Proxima Centauri d, a 0.26 $M_\oplus$ planet, result in a measurable radial velocity of 0.38 m/s due to their very short period around a smaller star, here around only 5 days.

The transit method has similar biases. In this method, the main determining factor whether a planet is observable or not is the ratio between the size of the planet and the star. A transit of Jupiter as seen outside of the solar system would result in a transit depth of about 1%, whereas Earth would result in a transit depth of 0.01%. Just as with the radial velocity method, these transits would only occur once in 12 years and 1 year, respectively, meaning we would need long-term observations to detect a system similar to ours. The transit depth and period result in a bias towards large planets or planets around small stars, preferably on short orbits. This has made M-type stars the prime candidates for the search for rocky exoplanets within the habitable zone.

Observations of rocky exoplanets have primarily been carried out using instruments such as Spitzer and Wide Field Camera 3 on the Hubble Space Telescope. These observations have primarily focused on the close-in planets around low-mass stars, which, as mentioned before, are the easiest to observe and result in the highest possible signal-to-noise ratio. Despite this advantage, however, rocky exoplanet observations using these instruments have so far led to non-detections or inconclusive results (de Wit et al. 2016; Diamond-Lowe et al. 2018; Edwards et al. 2021; Mugnai et al. 2021). Several reasons might lead to an observation being inconclusive, including instrumental limitations, masking of atmospheric signals due to clouds or contamination from the star, or because there is simply no atmosphere.

At the time of writing this thesis, the most suited instrument for the study of exoplanet atmospheres is the James Webb Space Telescope (JWST, Gardner et al. 2006, 2023). Its high sensitivity and near-to-mid infrared wavelength coverage allow JWST to determine the presence or absence of atmospheres. Koll et al. (2019), for example, determined that JWST will be able to detect or rule out secondary atmospheres for $\sim$100 targets. In transmission spectroscopy, JWST's near-infrared instruments NIRISS and NIRSpec and mid-infrared instrument MIRI cover several important species for secondary atmospheres such as CO_2 and H_2O (Barstow & Irwin 2016; Morley et al. 2017; Krissansen-Totton et al. 2018; Lustig-Yaeger et al. 2019). On the other hand, the thermal emission from a planet can be used to differentiate between planets with thick cloud coverage and atmosphereless worlds, as an atmosphere would redistribute the heat and lead to a lower thermal emission.

However, thermal emission measurements of TRAPPIST-1 b and c by JWST/MIRI rule out the presence of a thick CO_2 atmosphere, suggesting these are bare rocks (Greene et al. 2023; Zieba et al. 2023). Observations of transmission spectra of LHS 1140 b, a rocky habitable zone planet, using NIRISS and NIRSpec are similarly inconclusive but consistent with bare rock (Cadieux et al. 2024; Damiano et al. 2024). Many of these observations remain uncertain due to the fact that thin atmospheres (i.e. less than 10 bar) often have signatures similar to airless planets within the error bars of current observations.

Perhaps one of the most interesting rocky planets observed with JWST is 55 Cancri e (Hu et al. 2024). This 8.8 $M_\oplus$ planet with an orbital period shorter than 18h has been a curious target since its Spitzer observations. These observations have shown variable eclipse depths (Demory et al. 2016). Further observations with JWST have shown that these variations occur within one week (Patel et al. 2024). It has been proposed that this variation might be the consequence of a magma-cloud feedback loop (Loftus et al. 2024). The authors suggest that due to the planet's small orbital distance, its surface can reach temperatures up to 2800 K, causing the surface to melt causing it to outgas. This, in turn, causes clouds to form, which block the stellar radiation from reaching the surface, cooling the surface back down to about 1000 K. Once the clouds rain down to the surface again, the radiation can heat up the surface once more, starting the loop over. Though this explanation fits observational data, many different models still seem to fit within the observational uncertainties.

A method to remove some uncertainty is to observe a phase curve of the planet to determine the heat distribution between the day and nightside. In the case that the planet has an atmosphere, heat is expected to be redistributed towards the colder nightside. On the other hand, if a planet does not have an atmosphere, the surface on the dayside would heat up, whereas the nightside would cool down without much redistribution. Phase curves from several studies (Kreidberg et al. 2019; Zhang et al. 2024; Luque et al. 2024) demonstrate that thick cloud-free atmospheres can be ruled out through featureless transmission spectra. A large difference between the day and night-side temperatures helps exclude the thick, cloudy atmospheres. However, even with measurements at various points in the planet's orbit, it can be difficult to determine conclusively whether a planet has an atmosphere, as different rock compositions and thin atmospheres still have similar signatures with the observed error bars.

One solution to this problem is to observe the planet more often and stack the observations to minimise the error bars. The main problem with this approach is that measurements of a thin atmosphere are estimated to require several tens of transits or eclipses (e.g. Lustig-Yaeger et al. 2019).

Unfortunately, telescope time is limited, and it is hard to justify spending the time suggested in those works on a single target. A second solution would be to combine observations at different wavelengths, in particular those in and out of the expected features of the atmosphere. A difficulty of this approach is that it can be tricky to properly calibrate different instruments (e.g. Madhusudhan et al. 2023; Luque et al. 2024). Another option would be to inform the retrieval as much as possible, by constraining possible combinations of parameters from a theoretical point of view. The modelling of atmospheres is what we will tackle in the next chapter.

Chapter 2

Atmospheric modelling

"And thus were created the conditions for a staggering new form of specialist industry: custom-made luxury planet building."

- **Douglas Adams**, "The Hitchhiker's Guide to the Galaxy"

Introduction

In the previous chapter, we got an overview of the many components that affect atmospheres and some results from observations. In this chapter, we will take a closer look at the different ways to make sense of observations. To do this, we will take a more theoretical approach and discuss some methods that are currently in use.

Broadly speaking, we can divide current exoplanet atmosphere research into two categories: forward models and retrievals. In forward modelling, the state of an atmosphere is modelled based on boundary conditions or initial conditions. From this initial point, the models go through several different physical processes until a steady state is reached. On the other hand, retrievals approach the question from the other direction. The output of different forward models is matched against an observation until one is found to match. We will look at retrievals in more detail in Section 2.2 as this is a very commonly used tool in exoplanet research, in particular since the launch of the JWST. In Section 2.4, we will look in detail at the forward model used in the rest of this work. This forward model is currently not compatible with retrievals, as they require too much time per model. In Chapter 4, we will discuss how to reduce the calculation times of this forward model. But let us first look at forward models in general.

2.1 Forward models

There are many different forward models which focus on various parts of the atmospheres of exoplanets. Models focusing on the origin of the atmosphere look at the interiors of planets (e.g. Baumeister et al. 2023; Dorn et al. 2018; Rogers et al. 2024). These models can range from 1D models that look at the phase equilibrium between the gaseous atmosphere and the rocky surface or magma oceans (e.g. Lebrun et al. 2013; Herbort et al. 2020), to 2D fluid dynamics which look at the solidification of the interior and the depletion of the volatile content (e.g. Noack et al. 2017; Baumeister et al. 2023). These models can provide insights into, amongst others, the composition of the atmospheres, the amount of atmosphere outgassed, and the time at which the atmosphere is formed.

Moving a step upwards, we reach the troposphere. For Earth, the field of meteorology is dedicated to understanding and modelling all that happens in the layer closest to the surface. The models used to predict the weather can be focused on small areas or specific parameters, such as air quality, but often rely on measurements of the current conditions to make predictions, which might not be as useful in the exoplanet context. The climate of Earth is modelled using so-called Global Circulation Models (GCM), which model the circulation of the atmosphere and ocean. These models have also found applications in the field of exoplanets (e.g. Kopparapu et al. 2016; Turbet et al. 2022). This type of model can provide valuable insights into the redistribution of heat around a planet through zonal winds, or even into asymmetries between the morning and evening terminator. A possible downside of applying these models is that they require some assumptions about the surface of the planet. On Earth, we know how landmasses, mountain ranges, and ocean currents can strongly influence the climate and the circulation of air. For exoplanets, we unfortunately do not have such detailed information, and models often assume either an Earth-like topology or a global ocean.

Another subset of models focuses on clouds. On Earth, most clouds are predominantly made up of water vapour. We do not have to look beyond the Solar System to already see clouds made up of other species, such as sulfuric acid on Venus (Rimmer et al. 2021) or methane on Titan (Nixon et al. 2018). Clouds of exoplanets can have a wide range of compositions from water vapour to silicate clouds (Herbort et al. 2022), or altitudes and circulation patterns (e.g. Mak et al. 2024). All of these clouds can have significant effects on the surface, either heating it through greenhouse gases (Kopparapu et al. 2016) or cooling it down due to reflection or optical thickness (Loftus et al. 2024). The modelling of clouds brings its own set of complications, either due to the computational intensity of microphysics or the parameterisation of these micro-processes (Morrison et al. 2020).

If we continue upwards in the atmosphere, we reach the upper atmosphere. In this work, we loosely define the upper atmosphere roughly as the layers above significant cloud formation but below the exobase, which corresponds to the thermosphere and mesosphere on Earth. This is the region where the radiation from the star first reaches the planet and has the strongest effect. As already mentioned in Section 1.4.1, the exobase is defined as the point where particles in the atmosphere have a longer mean free path than the scale height. This means that it is the location where atmospheric escape becomes important. Several models exist focusing on different parts of the upper atmosphere, such as the chemistry (e.g. Venot et al. 2015; Tsai et al. 2021), whilst others focus more on the hydrodynamics of the layer (e.g. Yoshida & Kuramoto 2020). One of the main complications of modelling atmospheres and, in particular, upper atmospheres, is the interconnectivity of all modelled assets. For example, the temperature at a given altitude will influence the chemistry occurring at that altitude, which will affect which wavelengths of the starlight are absorbed, which in turn influences the temperature. Ideally, all of these factors are taken into account within the same model. Several such models have been made (e.g. Johnstone et al. 2018; Nakayama et al. 2022) and often require iteratively going through each included factor to reach a steady state. This makes these types of models usually very slow or unstable. In Section 2.4 we will look at such a model in detail.

A last group of models of interest to planet atmospheres are those looking at the exobase. These models focus on the movement of individual particles beyond the collisional regime. The main focus for this type of simulation is usually the interaction of the atmosphere with the solar/stellar wind, and the magnetic field of the planet (e.g. Kislyakova et al. 2020; Gronoff et al. 2020, and references therein). As mentioned in Section 1.4.1, non-thermal losses make up the majority of atmospheric losses on Earth. Also for exoplanets, this type of loss is important, in particular those close to their host star or around active host stars (e.g. Presa et al. 2024). These losses can also provide insights into effects that are not directly measurable, like coronal mass ejections (Hazra et al. 2022). This type of model either solves the magneto-hydrodynamic equations for the stellar wind (Tóth et al. 2005) or looks at the individual particles through direct simulation Monte Carlo kinetic models (Kislyakova et al. 2020).

2.2 Retrievals

One of the most commonly used tools in exoplanet observations at the moment is retrievals. In essence, when a retrieval is applied to an observation, a set of parameters in a radiative transfer model is varied and repeatedly compared to the observation to determine the best-fitting model. By comparing all of the different input parameters and their resulting spectra, the retrieval returns the best fitting model and depending on the search algorithm, also the posterior probability distribution and correlations of the parameters (see for example review by Barstow & Heng 2020).

The first part of a retrieval is the model, which is usually referred to as the forward model. The main requirement for this model is that it runs fast, since a retrieval often involves hundreds of thousands to a million models to adequately sample the parameter space. Because of this requirement, the models need to be simple or parameterised 1D models, to run within a feasible amount of time. Some common approximations include chemical equilibrium, constant thermal profiles such as isothermal profiles or Guillot profiles (Guillot 2010), hydrostatic atmospheres, and parameterised clouds. The second required part is the parameter estimation algorithm. This can be as simple as a grid of models to as complicated as nested sampling. These parameter estimations must balance covering the parameter space and efficiently sampling it. One of the more popular of these algorithms (at the time of writing) is MultiNest (Feroz & Hobson 2008) due to its non-Gaussian priors and posteriors.

As this thesis focuses on atmospheric modelling, we will take a closer look at the model part of the retrieval. As mentioned before, these models need to be simple enough to be repeated often, which is not necessarily a disadvantage. In the era of the Hubble Space Telescope and Spitzer, information content from spectra of exoplanet transits was rather limited, making it impossible to differentiate between complex models. The higher spectral resolution and wavelength coverage of JWST spectra allow more complicated models to be used in retrievals. A first example of how a model can become more complicated is the temperature profile. The simplest approach to the temperature structure of the atmosphere is an isothermal profile. As shown by Schleich et al. (2024), an isothermal structure is not sufficient to retrieve the parameters of synthetic spectra and often results in an overestimation of the retrieved parameters. Additional points in the thermal structure of an atmosphere allow for effects such as temperature inversions to be taken into account. These inversions can influence the chemical compositions of an atmosphere and thus skew the transmission spectra. On the other end of the complexity scale, models as expanded as a GCM could be used. Planets are inherently 3D objects, so one could argue that such a model is needed to realistically model an exoplanet. However, as we saw in Section 1.1.2, there are many types of planets for which we do not have examples in the Solar System. For example, tidally locked planets have been theorised to support liquid water on the substellar side of the planet whilst freezing over on the opposite side of the planet (e.g. Yang et al. 2020). Additionally, the lack of information about surface features, water coverage, or possible ocean currents leaves great uncertainty in these models.

A second important point within retrievals is how to handle chemistry. There are two approaches commonly used: free retrievals and chemical models (e.g. Kreidberg et al. 2015). In free retrieval, we do not assume any knowledge of chemistry, and we retrieve each species independently. The advantage of this approach is that it is not bound to the limitations of the model used to calculate the chemistry. One could argue that this is particularly useful in the case of the types of exoplanets for which we do not have in situ measurements to validate models. The disadvantage of this approach is that it can result in unphysical atmospheric compositions. The second approach is to include chemical models to restrict possible combinations of species in the atmosphere according to a chemical network. In order to keep the model fast enough, the chemical models are often limited to chemical equilibrium codes. This is important to keep in mind when we try to retrieve parameters from a planet where this assumption does not hold, such as, for example, close-in planets where photochemistry plays an important role (Tsai et al. 2023; Al-Refaie et al. 2022). However, the use of models might skew our retrievals towards solutions the model was tailored for, for example, Earth-like solutions. A possible solution is to include more physics in the model, but this often results in prohibitively long calculation times or parameterisations. Also, which physics are important? We can include more chemistry (Tsai et al. 2023), tidal effects (Jackson et al. 2008), or climate effects (Yang et al. 2020), just to name a few possibilities.

Outside of possible effects to include on the planet side of modelling, there is also the stellar side. Seeing as transit spectra are always observed as part of the stellar spectra, it is important to keep in mind how the star behaves as well. An example of these effects is limb darkening, which is particularly important during the ingress and egress of the transit (Csizmadia et al. 2013). Further examples include faculae and spots, which can influence measurements of planetary parameters such as the density (Rackham et al. 2018) or even mimic atmospheric features (Moran et al. 2023). Another stellar effect that is a worry in exoplanet observations is stellar activity. If a flare happens at around the transit, it can influence the baseline used to determine the transit depth and distort the observation (e.g. Howard et al. 2023). This shows that understanding the host star is a crucial part of understanding the exoplanet observations.

As already mentioned, in this work we will focus on the modelling aspect of exoplanet atmospheres. In the following sections, we will work our way up from a very simple model to a more complex model. In Chapter 4, we will take a look at how these complex models can be accelerated to be able to work within the framework of retrievals.

2.3 A simple model of mass loss

The main goal of the remainder of this chapter and Chapter 3 is to look at atmospheric losses to determine which planets could hold onto their atmospheres. In Section 1.3.2, we already discussed the various possible mass loss mechanisms that might affect a planet. Throughout all of these methods, the gravity acting on a particle is of great importance in determining if the particle remains bound to the planet. This importance is further reinforced by the fact that the escape occurs at the top of the atmosphere, which can significantly change as the atmosphere becomes "puffy". To illustrate this effect, let us look at a toy model. The first step is to calculate the exobase altitude. As described in Section 1.4.1, we will use the Knudson number for this:

$$\frac{\lambda_{mfp}}{H} = \frac{1}{\sigma n} \Big/ \left(\frac{k_{\mathcal{B}} T}{\mu g}\right) \tag{2.1}$$

If we assume our atmosphere is composed of an ideal gas, we can replace the number density n by a function of the pressure P, and temperature T. The cross-section of the particle can be calculated using the kinetic diameter d of the particles.

$$\frac{k_B T}{\sqrt{2}\pi d^2 P} = \frac{k_B T}{\mu g} \tag{2.2}$$

For the purpose of this simplified model, we will assume an isothermal atmosphere. We will not assume a constant gravitational acceleration, as our atmospheres can become very extended. With these assumptions, we will replace the pressure in the equation using the barometric formula:

$$\begin{aligned}
\frac{dP}{P} &= \frac{-\mu g(z) dz}{k_B T} \\
P(z) &= P_0 \exp\left(\int_0^z \frac{-\mu g(z) dz}{k_B T}\right) \\
&= P_0 \exp\left(\int_0^z \frac{-\mu G M dz}{k_B T (z+R)^2}\right) \\
&= P_0 \exp\left(\frac{-\mu G M}{k_B T}\left(\frac{1}{R} - \frac{1}{z+R}\right)\right) \\
&= P_0 \exp\left(\frac{-\mu G M}{k_B T}\frac{z}{R(z+R)}\right)
\end{aligned} \tag{2.3}$$

This equation can then be placed in Eq. 2.2 and simplified as follows

$$\begin{aligned}
\frac{k_B T}{\sqrt{2}\pi d^2 P_0 \exp\left(\frac{-\mu G M}{k_B T}\frac{z}{R(z+R)}\right)} &= \frac{k_B T}{\mu g} \\
\frac{\mu}{\sqrt{2}\pi d^2 P_0} &= \frac{\exp\left(\frac{-\mu G M}{k_B T}\frac{z}{R(z+R)}\right)}{g}
\end{aligned} \tag{2.4}$$

In this equation, we have one more term to replace, namely the gravitational acceleration. In the barometric equation, we have already replaced this term with the altitude-dependent equation.

$$\begin{aligned}
\frac{\mu}{\sqrt{2}\pi d^2 P_0} &= \frac{\exp\left(\frac{-\mu G M}{k_B T}\frac{z}{R(z+R)}\right)(z+R)^2}{GM} \\
\frac{\mu G M}{\sqrt{2}\pi d^2 P_0} &= \exp\left(\frac{-\mu G M}{k_B T}\frac{z}{R(z+R)}\right)(z+R)^2
\end{aligned} \tag{2.5}$$

This gives an equation where all altitude-dependent terms are on the right-hand and all terms we assume to be constant through our atmosphere are on the left-hand side. In this equation, we will assume the different atmospheres to be composed of a single species listed in Table 2.1. Furthermore, we will assume a planet with a mass and a radius equal to that of Earth for this example. We can solve the equation numerically for a given temperature to find the exobase altitude.

Table 2.1: Mass and kinetic diameter of modelled species.

Species name	μ [1.7.10^{-27} kg]	d [1.0^{-12}]
H	1	25
H_2	2	289
C	12	70
CO	28	376
CO_2	44	330

Once the exobase altitude is found, we can calculate the escape velocity at this altitude. Next, we can calculate the most probable thermal velocity of the particles in the atmosphere for the same temperature.

$$\begin{aligned} v_{esc} &= \sqrt{\frac{2GM}{r_{exo}}} \\ v_{therm} &= \sqrt{\frac{2k_{\mathcal{B}}T}{\mu}} \end{aligned} \tag{2.6}$$

When this thermal velocity exceeds the escape velocity, the atmosphere can be lost. Figure 2.1 shows how these two velocities change as a function of our assumed temperatures. The dashed lines on the figure indicate the escape velocity at the exobase for the different compositions in Table 2.1. The full lines show us the thermal velocities of the particles in the atmosphere. If we start with an atmosphere composed of just H, we can see that the escape velocity rapidly drops to zero as the temperature reaches about 250 K. Due to the light mass of H-particles, the atmosphere needs to be very extended to support a surface pressure of 1 bar. Additionally, H atoms reach higher velocities much more easily, also due to their light mass. The escape velocity and thermal velocity cross around this 250 K mark, which would mean that an atmosphere at this temperature would start losing particles with at least the average thermal velocity. For an H_2 atmosphere, this would occur around 410 K, due to the mass of the particles increasing.

In a more realistic case, an Earth-sized planet would have a secondary atmosphere made up of elements like CO_2, shown by the light blue line in Figure 2.1. This atmosphere would be lost at temperatures of about 10 000 K. However, the atmosphere's composition also changes under the conditions that would lead to such high temperatures. Through either chemistry, photochemistry, or high temperature, the CO_2 molecules of our simple atmosphere will break down into CO, C, and O (and of course ions, but that is beyond this example). These species are lighter and require a much lower temperature to escape to space. In Figure 2.1, we see that an atmosphere of pure C would only require a temperature of 3000 K to escape.

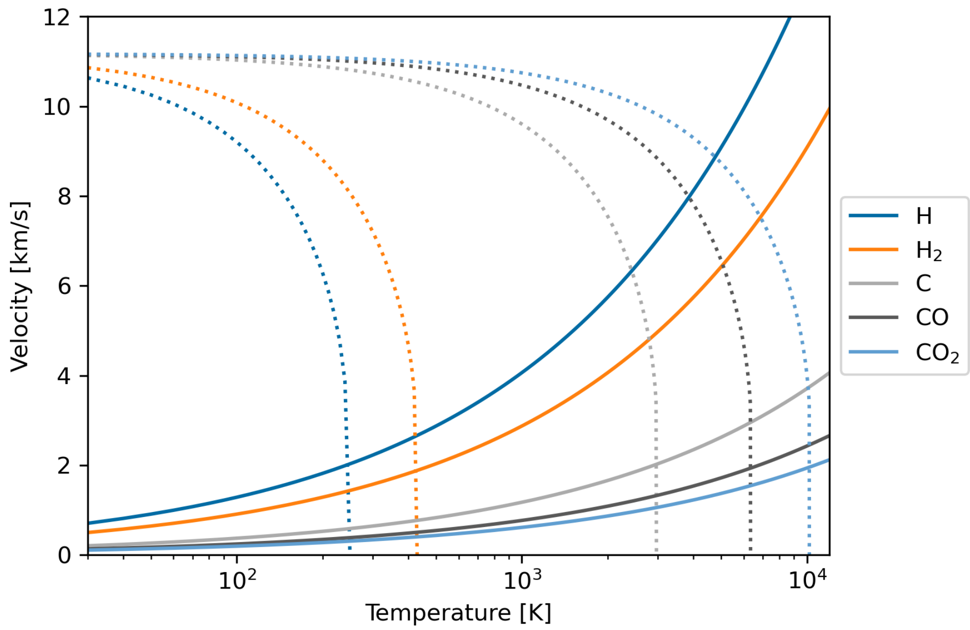

Figure 2.1: A toy model of atmospheric escape for an Earth-like planet. The full lines indicate the thermal velocity of the particles in the atmosphere, whilst the dashed lines indicate the escape velocity at the exobase of the atmosphere.

This simple model illustrates how many non-linear effects contribute to the structure of the atmosphere. A highly irradiated planet will heat up, which causes chemistry and photochemistry to change its composition. This, in turn, makes the atmosphere expand. All of these changes also contribute to the mass loss rate of the atmosphere. To better understand all of these effects, we will have a look at a more in-depth model in the next section.

2.4 The Kompot code

In this work, we focus on a particular code called the Kompot code. This code was developed at the University of Vienna and first described in Johnstone et al. (2018). The Kompot code is a self-consistent, one-dimensional thermo-chemical code which models cloud-free upper atmospheres based on first principles. This code was originally developed to model Earth (Johnstone et al. 2018; Kislyakova et al. 2020) but has also been applied to early Earth (Johnstone et al. 2021b; Grasser et al. 2023), the Martian atmosphere (Amerstorfer et al. 2017), water-dominated planets (Johnstone 2020), and exoplanets (Van Looveren et al. 2024). Let us have a closer look at how the Kompot code works before we discuss applications.

2.4.1 Overview

The Kompot code includes many aspects, such as the transfer of stellar irradiation in the X-ray, UV, and IR regimes and the resulting heating and photochemistry; chemical reactions; molecular and eddy diffusion; IR cooling; and thermal conduction. Additionally, the modelled atmosphere expands and contracts in reaction to the changes in the temperature profile.

It does this in a self-consistent manner, meaning that not only does it take into account each of these aspects, but also how they interact. To solve all the different parts of the included physics, the code uses an operator-splitting approach. In this approach, the differential equations that describe the model are decomposed into a sum of partial problems. For example, the change of temperature in a part of the atmosphere is influenced by incoming radiation, chemical reactions, and thermal conduction, just to name a few points. Rather than solving all of these terms in the equation at once, each is solved sequentially to form a full timestep. This process is then repeated iteratively until a steady state is reached. Depending on the number of chemical equations included, the wavelength range taken into account, and how far the initial estimate is from the final solution, this can require millions of iterations.

Another strength of the Kompot code is that it is based on first-principles physics, which means that it avoids using parameterised scaling laws and free parameters as much as possible. Instead, the code uses physical laws and exact relations where possible. The advantage of this design choice is that poorly constrained parameters, such as heating efficiency or escape efficiency, are avoided, yielding calculations that are more precise. The downside of this approach is that many more calculations are needed, which inevitably leads to longer computation times. In Chapter 4, we will discuss ways to both have and eat the proverbial cake.

In the upcoming sections, we will first take a closer look at some of these aspects that are relevant to this thesis. For an in-depth discussion of the model, readers can turn to Johnstone et al. (2018).

2.4.2 Chemistry and photochemistry

The first version of the Kompot code, as described in Johnstone et al. (2018), contained 63 species, of which 30 were ion species. These species cover some of the most common species found in Earth's atmosphere, containing the atoms: H, He, C, N, O, Ar, and Cl. All of these species were combined into a chemical network of 447 chemical reactions and 56 photoreactions.

A first addition to the chemistry was presented in Johnstone (2020). In that work, deuterium and species containing deuterium were added to the network, resulting in an additional 9 species and 37 reactions. Considering deuterium as a separate species allows the code to model the fractionation of hydrogen and deuterium. This has been used to determine both the origin of volatiles and atmospheric escape rates, as the lighter protium is lost more easily.

A second addition to the chemistry was the addition of sulphur and sulphur-bearing species as presented in Grundnig & Van Looveren (in prep.). Though we only see trace amounts of sulphur-bearing species in Earth's atmosphere, SO_2 is the third most abundant species in the atmosphere of Venus. These species are important greenhouse gases near the surface of Venus and are part of the thick cloud deck. Unfortunately, neither of these regions is modelled by the Kompot code as condensation is not included at the time of writing this thesis. Sulphur species are also of particular interest in hydrogen-dominated atmospheres. From equilibrium chemistry, sulphur is expected to be predominantly locked up in HS. However, SO_2 had been theorised to be an indicator of photochemistry in highly irradiated planets. The first detection of the presence of SO_2 was reported in WASP-39 b (Tsai et al. 2023), a Saturn-mass planet with a Jupiter-like radius on a four-day orbit around its host star. Though photochemistry was to be expected in such a close-in planet, the fact that it has measurable effects on the planetary spectrum demonstrates that it is important to include both photochemistry and sulphur-bearing species in models. For similar reasons, hydrocarbon chemistry is also being added to the chemical network at the time of writing.

The chemical reactions form a set of ordinary differential equations. By default, Kompot solves these equations using an implicit multi-step Rosenbrock method as described in Appendix H of Johnstone et al. (2018) and adapted from Sandu et al. (1997), though other solvers are included. At its core, this method solves matrix equations of the form $Ak_i = B$. In this equation, k_i is the increment vector, which describes the reaction rate over a part of a time step and the variable we will solve for. Here, B is a vector of length N and A is a matrix of size $N \times N$, where N is the number of chemical species included, containing the reaction rates of the chemical network. This set of equations is solved through Gaussian elimination, a method with a complexity of the order of N^3. It is easy to see that as the number of species is increased, the computational time rapidly increases. However, observations of atmospheres show that complex chemistry does occur and needs to be included in model atmospheres. This means that in order to model large numbers of different atmospheres within a short amount of time, as when we perform retrievals, we either need to reduce the included chemistry or otherwise reduce computation time. As we already discussed in Section 2.2, the reduction of included chemistry, like with free chemistry retrieval, can lead to unphysical or degenerate solutions.

2.4.3 Heating and Cooling

Heating and cooling are crucial factors in the modelling of atmospheres. First of all, the chemistry of an atmosphere is strongly dependent on the temperature of the atmosphere at each particular altitude. Beyond the change in species, the temperature also determines the phase in which species exist in the atmosphere. On Earth, this is demonstrated clearly through the cold-trap, which prevents the relatively light water molecules from rising to altitudes where they can dissociate into even lighter hydrogen and oxygen. In Section 1.4.1, we saw that an increase in temperature can lead to catastrophic losses. Likewise, having the correct cooling pathways available in an atmosphere can prevent these losses. So let us have a look at the different mechanisms that are included in the Kompot code.

2.4.3.1 Heating

In the previous section, we already saw that the Kompot code includes a large network of chemistry. A large section of these reactions is exothermic and adds heat to the atmosphere. This is the dominant type of heating at lower altitudes. This is due to the relatively high density of molecules, allowing for many different chemical reactions. Figure 2.2 demonstrates this effect for an Earth-like atmosphere. In the left panel, we can see that at an altitude of 100 km, the number of molecules decreases as they get dissociated by the incoming radiation. On the right panel, we see that the chemical heating, shown by the full blue line, is greatest below these altitudes as well. At 250 km, the atmosphere has a similar amount of molecules and atoms. This leads to the greatest variety of species, which allows for many different chemical reactions to occur. In turn, this leads to the strong increase in chemical heating we see reflected in the right-hand plot. The heating from chemistry is also influenced by the included species and the mixing ratios of these species. Because of this, the trends we see in Figure 2.2 do not necessarily occur at the same altitudes if we change the chemical composition.

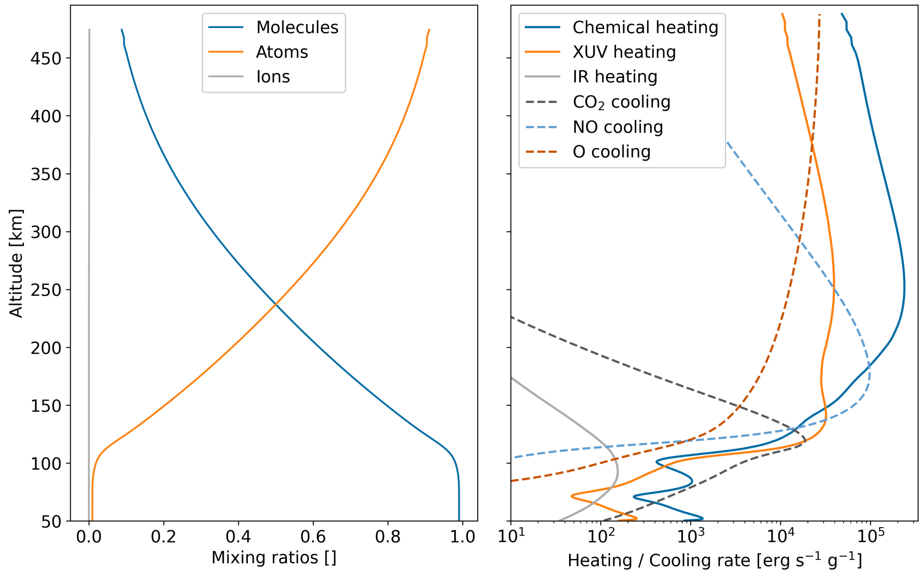

Figure 2.2: The general composition and heating and cooling mechanisms of a model with Earth's composition. The left panel shows the relative abundances of molecules, atoms, and ions for different altitudes. The right panel shows the different heating mechanisms with full lines and cooling mechanisms with dashed lines.

The next major source of heating we will discuss is XUV heating. This is the heating caused by an X-ray or ultraviolet photon from the star being absorbed by a particle in the atmosphere. There are no exact definitions of the wavelength range covered by the XUV, but within this work, we will define it from 1 to 400 nm. Within the atmosphere, there are molecules that can get dissociated and atoms that can get excited to a higher energy level. These are included in the model through photochemical reactions. For each included photoreaction, the species in question has wavelength-dependent cross-sections which were taken from the KIDA database (Wakelam et al. 2012). These cross-sections define the wavelength of the photons that the molecule or atom can absorb. When a photon is absorbed, a part of its energy is used in the reaction to break the bond of the molecule or push the atom to the excited state, the bonding energy or excitation energy, respectively. The resulting particle absorbs the remaining energy in the form of thermal energy. This makes the XUV heating strongly dependent on the stellar radiation and the particles present at a specific altitude. Because of this, the spectrum of the star needs to be calculated at each altitude through radiative transfer. However, each time the chemical composition of the atmosphere changes, the radiative transfer needs to be recalculated. The repeated calculation of the radiative transfer makes this step the second-most computationally intensive step of the model.

In Figure 2.2, the orange line indicates the XUV heating. We can see that this is a major and near-constant source of heating down to an altitude of 100km. Below this altitude, the atmosphere is composed mostly of molecules, as the photons of the correct wavelength to dissociate these molecules have already been absorbed. This can be seen at higher altitudes where the composition changes towards being dominated by atoms. These atoms can, in turn, absorb other photons to reach excited states or even ionise. This is not visible in Figure 2.2 because the modelled scenario is not irradiated enough to reach a significant ionisation rate even at the top of the atmosphere. Planets closer to their host star can become much more ionised. This, in turn, can lead to an increase in non-thermal losses, though this falls outside of the scope of this work.

Beyond XUV radiation, another important heating source is Infrared (IR) radiation. IR radiation is of particular importance in the calculation of the surface temperature, as discussed in Section 1.3. At longer wavelengths, the absorption of photons occurs primarily through molecular bands. The Kompot code was originally developed to model Earth around the Sun and thus has several assumptions that are important to keep in mind. The first assumption is that the IR spectrum follows the Planck curve for a given temperature. Though this works for stars like the Sun or hotter, this assumption becomes less correct for cooler stars as their spectra contain many of the same molecular bands. The second assumption is that only the absorption through H_2O and CO_2 is taken into consideration. In Earth's atmosphere, these are the main absorbing species, in large part due to their mixing ratios. Other species also contribute to absorption bands on Earth, notably ozone, methane and nitrous oxide, though to a much lesser degree. We can easily see then how this second assumption might break down for an atmosphere with a different composition. Returning to Figure 2.2, we can see the heating due to IR heating noted through the full grey line. This heating occurs mostly near the bottom of the simulated domain. This can be explained by the presence of the absorbing molecules at lower altitudes. On Earth, we see that IR heating becomes even more important in the troposphere, where there is a higher concentration of water vapour.

The last type of heating included in the Kompot code is Joule heating. This type of heating, also called Ohmic heating, is the result of charged particles moving through the magnetic field of the planet. Due to Earth's comparatively weak magnetic field, this type of heating is not very effective. In Figure 2.2, Joule heating was not added because it falls below the lower limit of the plot. Similarly, this heating is not very effective in any of the other rocky planets of the Solar System. We do, however, observe this effect strongly in some of the gas giant atmospheres and some of their moons, in particular Jupiter and Io. The moon Io gets heated through tidal heating, causing it to be extremely volcanically active. As the moon orbits within the magnetic field of Jupiter, the particles ejected by the volcanoes are guided along magnetic field lines into Jupiter's atmosphere. These particles can cause significant heating in Jupiter's atmosphere. The same effect is expected to affect planets that move within the Alfven radius of their star.

2.4.3.2 Cooling

The Kompot code includes several cooling pathways through the IR emission. This happens when a particle reaches an excited state through collisions with other particles and emits a photon through radiative relaxation. As described in section 2.5.2 of Johnstone et al. (2018), the Kompot code only considers emission lines known to contribute to the cooling of Earth's atmosphere through approximated relations. These included emission lines are:

- CO_2 at 15 μm
- NO at 5.3 μm
- O at 63 μm and 147 μm
- H_2O through rotational bands
- Lyman alpha

Each of these transitions has collision partners associated with it that influence the number of excited atoms or molecules. This means the efficiency of a cooling mechanism depends on the presence of the particle emitting the photon and the number density of the collision partner. In the previous section, we saw that CO_2 and H_2 absorb IR radiation, which leads to heating. Because of this, a term is added to reflect that not all emitted photons escape to space, but can also be reabsorbed. For CO_2 this is done through the calculation of an escape probability that depends on the number density of CO_2 above the altitude where the photon is emitted. For H_2O, the optical depth of a column of the atmosphere is determined to find the amount of escaping photons. This rather extensive calculation was adopted from Kasting & Pollack (1983) equations 32 through 38.

Though within this work we will not go into details of the exact calculation of each of these cooling terms, it is important to understand how they can contribute to the planet's thermal structure. In Figure 2.2, we can see how the CO_2 cooling shown by the dashed grey line is the dominant source of cooling near the bottom of the simulated domain, where molecules are also dominant. CO_2 cooling reaches its maximum around 120 km as there are still many molecules at this altitude, but very few above, allowing more photons to escape. At an altitude of 160 km, we can see that NO cooling becomes the dominant cooling mechanism, shown by the dashed blue line. At this altitude, O_2 molecules start to break down due to the radiation, which allows the free oxygen atoms to recombine with nitrogen into NO. Above 300 km, we see that the cooling through atomic oxygen, the red dashed line, takes over as the dominant cooling pathway. This can easily be understood when we look at the left panel of Figure 2.2 and see that the molecules which provided the cooling at lower altitudes have mostly dissociated into atoms.

In Section 2.5, we will see that for the inner Solar System planets, this approach works reasonably well, though it has some shortcomings. The first problem we can identify is that the particular lines were selected based on Earth observations. Under different circumstances, be it a different composition or a different temperature regime, these lines are not necessarily the most efficient cooling species. This was highlighted by Nakayama et al. (2022), where more atomic line transitions were included. In that paper, the transition of atomic oxygen at 630 nm becomes a dominant cooling mechanism once the atmospheric temperature reaches 3000 K as the O(1D) energy level becomes more populated. Earth's atmosphere does not reach this temperature, and because of it, this energy level is not populated enough to have a significant impact on the temperature profiles. However, in other cases, like the early solar system or close-in exoplanets, this can become more important. As discussed in Chatterjee & Pierrehumbert (2024), this type of model can be sensitive to missing physics. In that work, the authors discuss how the addition of line cooling and radiative recombination does contribute to the cooling of highly irradiated planets, but an incomplete description of escape probability and ion-electron interactions leads to an overestimation of the cooling effect.

2.5 Model Validation

In this section, we will take a closer look at different Kompot models simulating solar system bodies. In Johnstone et al. (2018), the model was validated against Earth and Venus to demonstrate its accuracy. These comparisons allow us to validate the models using in situ measurements of different types of atmospheres. Furthermore, we can use these models to identify possible physics that might be missing or assumptions which may not always be valid. In this section, we will further test models of Earth, Venus, and Mars. The planets represent a small array of possible rocky planet sizes and secondary atmosphere compositions for which we have in situ data. We will not look at Titan since the thermal profile of its atmosphere is strongly influenced by the presence of methane, which is being implemented at the time of writing this work.

The input parameters we will use are listed in Table 2.2. These parameters represent general information on the planet as a whole, such as mass, radius, and orbital distance, as well as the lower boundary of our simulated domain. For the lower boundary, these parameters include the temperature at the boundary, the number density of the gas at the boundary, and the mixing ratios of species. It is important to note that we use the composition of the entire atmosphere rather than the boundary, as we can sometimes select boundary layers that have compositions not representative of the rest of the atmosphere. The Earth is a prime example of this; near the surface, the atmosphere can reach high levels of humidity due to the large amounts of surface water. However, the water content of the atmosphere drops rapidly at the cold trap, a region around 20 km altitude where the temperature is

Table 2.2: Summary of parameters used for the validation models.

Parameter	Earth	Venus	Mars
Planet Radius [$R_\oplus$]	1	0.95	0.53
Planet Mass [$M_\oplus$]	1	0.815	0.151
Semi-major axis [au]	1	0.723	1.523
Temperature base [K]	267.2	206	210
Number density base [cm^{-3}]	2.7×10^{19}	1.37×10^{17}	2.2×10^{17}
Mixing ratios [ ]	N_2 0.78110 O_2 0.20955 Ar 9.3430×10^{-3} CO_2 4.0×10^{-4} He 5.2417×10^{-6} H_2O 6.0×10^{-6}	CO_2 0.965 N_2 0.035 SO_2 1.5×10^{-4} Ar 7.0×10^{-5} H_2O 2.0×10^{-5} CO 1.7×10^{-5} He 1.2×10^{-5}	CO_2 0.9597 Ar 0.0193 N_2 0.0189 O 1.46×10^{-3} CO 5.57×10^{-4} H_2O 2.1×10^{-4}

cold enough to trap the water vapour below it. In these models, we set the lower boundary at the planet's surface for each modelled planet.

2.5.1 Earth Models

The first atmosphere we shall model is the Earth, as it is the most well-studied atmosphere. To validate these models, we will make use of the NRLMSIS model atmosphere (Picone et al. 2002). This is an empirical model of Earth's atmosphere that requires several input parameters, such as the time and location of the modelled column of the atmosphere. The temperature of the upper atmosphere can vary strongly depending on many factors, such as for example the exact distance to the Sun, the solar activity, the zenith angle at the time, date, and latitude used as input. We will use a model at a latitude of 66° and longitude of 0° at noon on the 10th of January and a second model at a latitude of -66° and longitude of 0° at noon on the 11th of May. These two models give us a range of possible conditions over a year that an atmosphere can be exposed to. The locations of these models have been chosen to result in a zenith angle of 66°, which represents the average day-side profile (Johnstone et al. 2018).

Figure 2.3 shows the temperature-altitude profiles of the Earth model with full lines. The shaded area shows a range of NRLMSIS empirical models for different conditions throughout the year, which we will use as a baseline. The grey line shows a model which uses the surface as a lower boundary with the parameters listed in Table 2.2. Just above the surface, in the troposphere, this model reaches much higher temperatures than the baseline. The troposphere is strongly influenced by local conditions of the surface. Some examples of this are the composition of the land, think here, for example, continent vs ocean, the albedo of the surface, or the moisture available for cloud formation. Additionally, the troposphere is also strongly influenced by circulation. In Earth's atmosphere, most clouds and hazes form in the troposphere (i.e. up to 20 km), but also at higher altitudes, mesospheric (up to 25 km) and stratospheric (up to 85 km) clouds can occur that can block radiation from reaching lower altitudes. These are all effects that are not included in the model and can explain part of the difference between the model and the baseline.

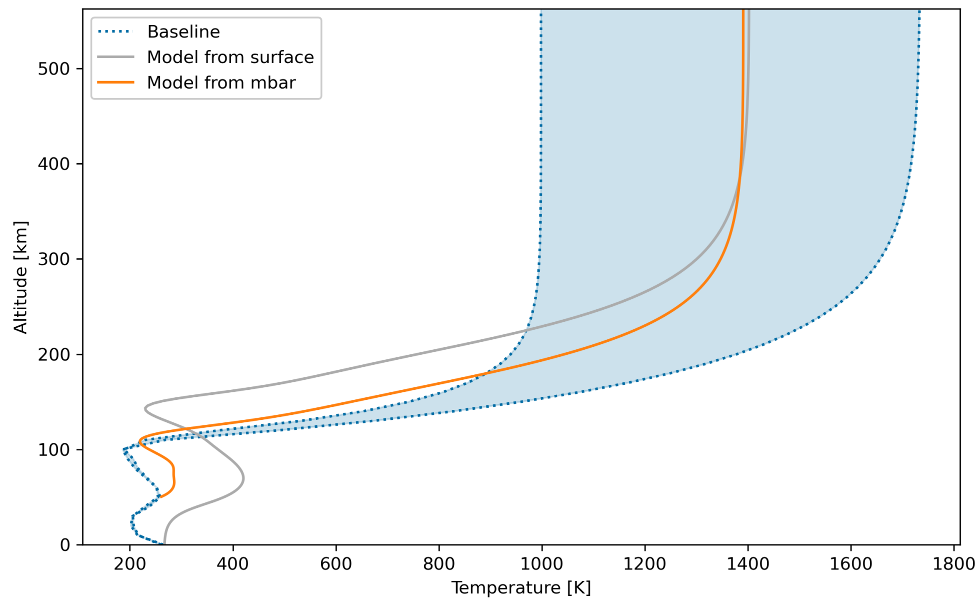

Figure 2.3: Altitude temperature profiles of Earth. The full lines show the Kompot models with different lower boundaries, while the dashed lines and shaded area show a possible range of NRLMSIS empirical models.

To avoid these types of errors, we can define the bottom boundary at a higher altitude where these effects do not occur. By setting the lower boundary at the 1 mbar level, or about 50 km on Earth, the model will be more representative by focusing on the cloud-free part of the atmosphere. This is shown

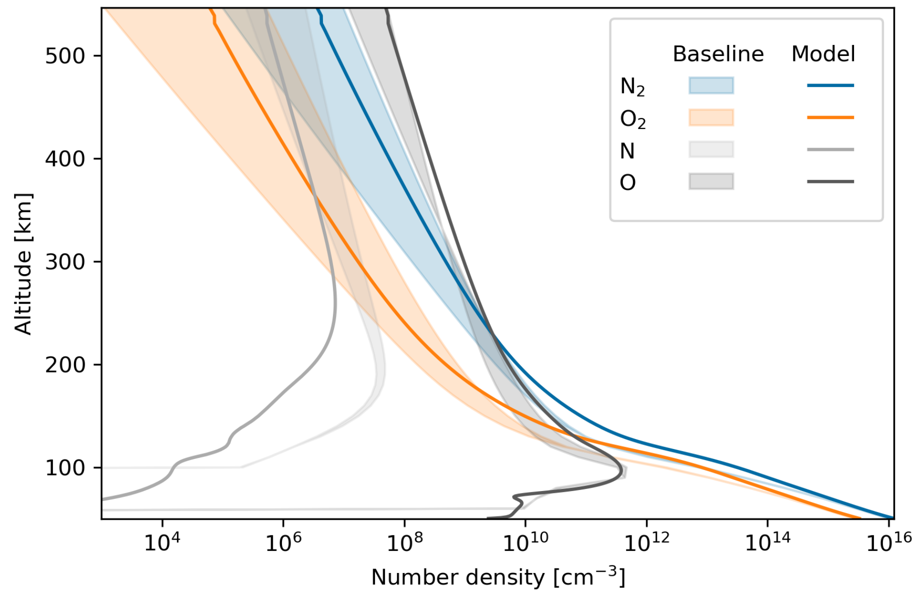

Figure 2.4: Altitude-number-density profiles of Earth. The full lines show the number densities of various species according to the Kompot model, while the shaded area shows a possible range of NRLMSIS empirical models.

in Figure 2.3 with the orange line. We can see that this second model increases in temperature whilst the baseline decreases towards an altitude of 100 km. This initial heating is a numerical artefact from modelling the atmosphere as a boundary condition problem. The bottom boundary of the domain has a fixed temperature, which unintentionally serves as a stronger reservoir of heat than what we can observe on Earth. The fixed chemical composition at the bottom is also a simplification of the actual chemical composition. Once the model calculates the chemistry using the full chemical network, this simplification causes heating in the layers just above the bottom layer. The inclusion of diffusion in the model continues to fuel this chemical heating. We see this numerical effect reflected in both models.

This problem is more difficult to prevent as fixed boundary conditions are required for the stability of the model. For the purposes of this work focused on the very top of the atmosphere, this discrepancy will not be a problem since it only affects the lowest layers in the simulated domain. If we wish to use these models as a basis for retrievals, as described in Section 2.2, this difference can become more important. Several possible solutions include setting the bottom layer to a lower altitude, but this might run into the problem we noted earlier with cloud formation, or using boundary conditions that are closer to equilibrium chemistry conditions rather than the mixing ratios of the total atmosphere. In order to use the latter solution in a self-consistent way, the model should be set up with elemental abundances rather than molecular mixing ratios. Such a solution is being implemented at the time of writing this work by a fellow PhD student, though it requires a more detailed study of possible compositions of the atmosphere as described by, for example Herbort et al. (2022).

The model starting from 1 mbar follows the baseline much closer, in particular above 100 km. Comparatively, the model starting at the surface has a much larger vertical offset. This is likely due to the larger reservoir of heat following the increased amount of chemical heating at higher pressures, combined with the less efficient cooling as the emitted radiation needs to travel through more atmosphere to escape. Near the exobase, both models reach a similar temperature. The temperatures of the model fall in the middle of the temperature range from the baseline and thus also represent the average conditions over the course of a year.

In Figure 2.4, we can see how the chemical composition of the model and baseline atmosphere change with altitude. The full lines show the number densities according to the Kompot models for some of the two most common species, N_2 and O_2, in Earth's atmosphere and the elements of these molecules. The shaded area shows the range in number densities of these species between the earlier-mentioned NRLMSIS models. From Figure 2.4, it is immediately clear that near the bottom of the simulated domain, the atmosphere is dominated by molecules. Though atoms can be formed through chemical reactions, they remain rather rare until an altitude of 100 km. At higher altitudes, the incoming stellar radiation is absorbed by the atmosphere and causes the molecules to photodissociate into atoms. Near the top of the atmosphere, atomic oxygen is the most dominant species, which, as we saw in Section 2.3, is lost more easily than its molecular counterpart. This figure also demonstrates that the chemical composition of the model matches quite well with the baseline, in particular near the top of the atmosphere where the loss occurs.

The remaining differences we see in Figure 2.4 could be due to missing pathways in the chemical network, the limited temperature and pressure range for which absorption cross-sections are available, or even differences in the used solar spectrum compared to the actual spectrum at a given moment. Though it is always important to keep all of these factors in mind, for the purposes of this work, our Earth model fits the baseline well enough. But let us look beyond the Earth to see how well it holds up under different circumstances.

2.5.2 Venus Models

Venus provides us with a very different view of rocky planets. Though Venus only has a mass of 0.815 $M_{\oplus}$, it has a surface pressure of 93 bar, demonstrating that the mass of the atmosphere does not necessarily scale with the size of the planet. The atmosphere is also composed mostly of CO_2, a molecule significantly heavier than the average molecule in Earth's atmosphere, and that is also known for its greenhouse effect. Observations of Earth's sister planet proved notoriously difficult due to the ever-present thick cloud deck limiting the wavelengths and depths that instruments can probe. Additionally, the hostile surface environment composed of high pressure and temperatures high enough to melt lead means that the electronics of landers either need to be very complicated or they do not survive very long. Due to the limited amount of data from lower strata, we will start our model at the millibar level rather than the surface. As we also saw already in the Earth models, the high-pressure environment closer to the surface is poorly captured by the Kompot code, due to the many cloud and circulation-related factors not included in the model.

The boundary conditions of the models were taken from Limaye et al. (2017), who summarised data from many different ground- and space-based instruments. The observations collected in that work already show a very interesting point, namely that due to its slowly rotating atmosphere with a four-day rotation period, the night side of Venus has more time to cool, creating a relatively large temperature difference between the day and night sides. This slow rotation is important to keep in mind when determining atmospheric losses using a 1D code, which models a specific zenith angle. Though we will again use an angle of 66°, this model will be representative of the day side of the atmosphere, but not necessarily of the night side. Despite the slow rotation rate of the atmosphere of Venus, it still rotates about 60 times faster than the surface, leading the atmosphere to be a so-called super-rotating atmosphere (Horinouchi et al. 2020). This can lead to strong zonal winds and consequently influence the cloud coverage of a planet, which again influences its temperature (Yang et al. 2014). Just as with the lower areas of Earth, a 1D model will not be able to fully capture these 3D effects, which is important to keep in mind whilst we look at our results.

Figure 2.5 shows the atmospheric temperature of observations from different instruments at latitudes between 50 and 70° on the Venus dayside (after figure 17 of Limaye et al. 2017) and the Kompot model of Venus. The figure shows that the model and observations are in good agreement within the modelled region. At lower altitudes between 60 and 80 km, we can see in the observations two thermal inversions. These altitudes correspond with the top of the cloud layer on Venus and thus cannot currently be accurately represented by our model. Due to this, we set the lower boundary of the model to the top of this region at an altitude of 80 km. In the upper reaches of the atmosphere, however, we can see that the model manages to recreate the thermal profile accurately. When we compare this modelled profile to Earth's modelled profile presented in Figure 2.3, we can see that the exobase of Venus only reaches a temperature of about 500 K, whilst Earth reaches temperatures close to 1800 K. Despite the fact that Venus is closer to the Sun than Earth and receives about two times the amount of flux, the planet with a hellish surface maintains a much cooler atmosphere. This is due to the large

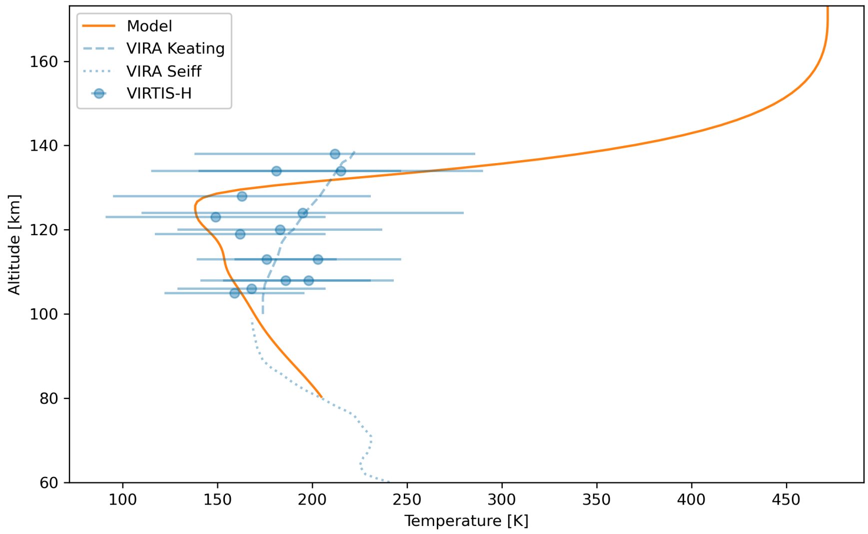

Figure 2.5: Altitude temperature profiles of Venus. The full line shows the Kompot model, while the blue dashed lines and points show observational data from different sources as summarised by Limaye et al. (2017).

amounts of CO_2 in the Phosphorian (one of the many adjectives suitable for Venus, referring to the god Phosphorus or "dawn-bringer") atmosphere, which acts as a coolant through the strong emission line at 15 μm. This, in turn, leads to small thermal atmospheric losses. In Chapter 3, we will see that this cooling mechanism is particularly important during the early evolution of planets.

2.5.3 Mars Models

Lastly, let us take a closer look at our next neighbouring planet, Mars, with a mass of only 0.107 $M_\oplus$. The Martian atmosphere, similarly to Venus, is primarily composed of CO_2 with smaller amounts of Ar, N_2, and O. Contrary to Venus, however, the surface pressure on Mars reaches only 6 mbar, whilst the average surface temperature is only 209 K. This combination of low pressure and temperature results in the fact that liquid water in the form of brines is rare and often limited to the lowest elevations where the pressure is just high enough (Heldmann et al. 2005). The geology of Mars, however, seems to indicate that the now red planet did experience an extended period of significant surface water (see for example a summary by Carr & Head 2010). The build-up and erosion of sediment in alluvial fans indicates that this was not a single period of liquid surface water, but rather an extended time with episodes of surface water (Kite et al. 2017). Kite et al. (2022) have also shown that during river periods on Mars, the atmospheric pressure could have been as high as 150 mbar. We already noted in Section 1.4.2, observations of non-thermal losses show that even today, Mars loses heavier atoms such as Ar and O to non-thermal loss processes. Though we will focus on modelling present-day Mars in this section, the study of the evolution of its atmosphere is interesting as well and will be the topic of our upcoming work.

The observations we will use for a comparison against the Mars model were collected by the Opportunity Rover during its descent (Withers & Smith 2006). This rover landed at -1.948282° N at a local solar time of 13:13, making this close to the substellar point. Near the bottom of the simulated domain, we can see a slight increase in temperature, which we noted before due to the fixed boundary condition. At higher altitudes, up to 80 km, both profiles follow a similar slope, though with an offset. These differences between the model and the observations are less than 40 K over this range. The slightly higher temperatures could be due to circulation or simply because we are closer to the substellar point than we assumed in the model.

At altitudes above 80 km the temperature increases rapidly due to the stellar radiation. Another difference we see between the model and observations is a decrease in temperature at approximately

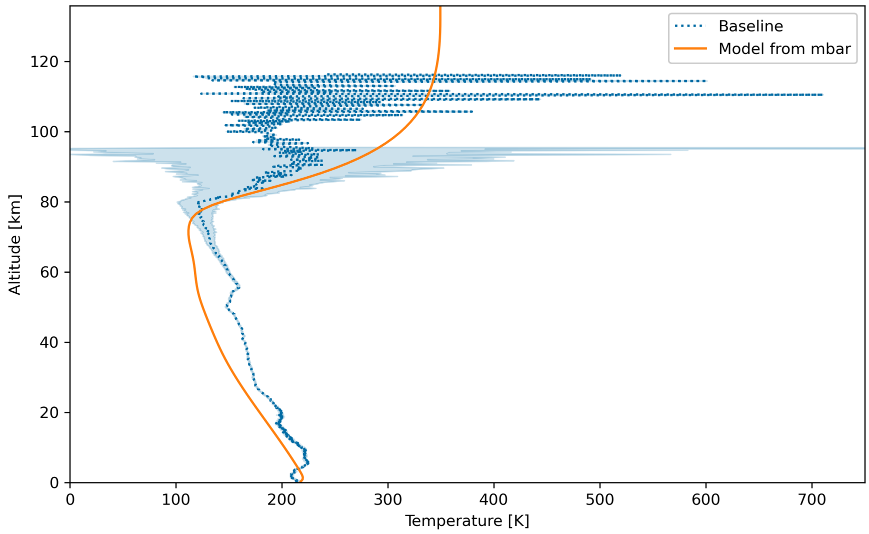

Figure 2.6: Altitude temperature profiles of Mars. The full line shows the Kompot model, while the dashed lines and shaded area show observational data and their error bars from the descent of the Opportunity Rover Withers & Smith (2006).

100 km in the observations. This coincides with the mesopause of the Martian atmosphere. Observations from various instruments have shown that there are CO_2 ice clouds present around this altitude (Montmessin et al. 2006). These clouds are similar to noctilucent clouds on Earth, occurring at low pressures and forming ice more easily. However, this difference is rather minor and does not impact the model at the top of the simulated domain, which matters most in loss calculations.

These three validation models have shown that the Kompot code can quite accurately recreate observations of rocky planets. These models have, however, also highlighted the areas where the model is less representative, which we should keep in mind when modelling planets beyond the Solar System.

Chapter 3

Habitable Zone and Atmospheric Retention Distance

"About that... I have some good news and bad news."

- **Taimi**, "Guild Wars 2, Living World Season 3"

Declaration of published work

This chapter includes text already published in Van Looveren et al. (2024) and Van Looveren et al. (2025). As a result, there may be partial overlap with this publication.

Introduction

In this chapter, we take a closer look at the interplay of different factors that influence atmospheres. Here will present results which have been previously published in Van Looveren et al. (2024) and Van Looveren et al. (2025). First, we will look at the atmospheric loss and several planetary parameters that influence it. These parameters include the planet's mass, radius, and orbital distance. Also of great importance is the composition of the atmosphere, in particular the mixing ratio of CO_2 (as we saw in Section 2.5) After that, we will combine these results with stellar models to apply our new knowledge of mass loss to other planetary systems and what this means for exoplanet observations.

3.1 Model parameters

The first step in determining the mass loss rate of a planet is to calculate its thermal profile. This will require several boundary conditions. Unfortunately, contrary to the Solar System planets, which we discussed in Section 2.5, we do not have any measurements of exoplanets to provide as boundary conditions for our models. Choosing realistic values for these parameters is essential to creating realistic models because a model with rubbish input will produce rubbish output.

3.1.1 Lower boundary conditions

The first parameter to look at is the base density. We saw in Section 2.5 that one of the main causes of deviations between models and observations was the presence of clouds and condensation. In our Earth model, we demonstrated that placing the lower boundary near the millibar level resulted in much more accurate results. Although clouds can form at higher altitudes, as discussed in the Mars model, these tend to be rather rare and thus have a much smaller impact on our models. But how do we determine this millibar level for different planets? On Earth, the atmospheric pressure decreases from 1 bar at the surface to a millibar at an altitude of approximately 50 km. On Venus, the surface pressure is around 93 bar and the millibar level at approximately 85 km (Limaye et al. 2017). We can use the barometric equation (see Equation 2.3) to calculate the altitude at which the pressure would reach a millibar if Earth had a surface pressure of 93 bar, which also results in an altitude of 87 km. This difference results in an upward shift of the simulated domain, which only influences the gravitational acceleration in our model. The exact gravitational acceleration is important when determining the escape velocity. The upward shift of about 35 km would result in a difference in escape velocity of less than 0.3%. Because of this, it is safe to assume that for roughly Earth-sized planets, the exact altitude of the millibar does not greatly influence the mass loss rate. For this reason, we will simply assume the lower boundary to be at 50 km above the surface with a number density of 1.73077×10^{16} cm^{-3}. It is important to note, however, that if a planet has a higher surface pressure, it has more particles in its atmosphere. This means that if a planet experiences great mass loss, there is simply a larger reservoir to draw from. Since the majority of these particles fall outside of the simulated domain, we will treat the lower atmosphere together with any possible outgassing as a reservoir of particles.

The second boundary condition we will inspect is the temperature at the base of the simulated domain. As demonstrated by Venus, which has a temperature of 737 K at the surface but only 206 K at the millibar level, the surface temperature is not representative of the conditions in the upper atmosphere. One might argue to use the equilibrium temperature as a reasonable guess for the lower boundary temperature. However, when we compare Earth to Venus, which is closer to the Sun and thus should have a higher equilibrium temperature, we see that Venus is actually cooler at the millibar level by about 60 K. Figure 3.1 shows the altitude-temperature profiles of several Earth models that use identical input parameters, with the exception of the base temperature. These models use temperatures ranging from 250 K to 550 K. The higher temperature shifts the mesopause, the lowest temperature in the simulated domain, before the XUV heating becomes the dominant heating mechanism, upwards from 100 km to 150 km. This upward shift continues relatively linearly up to 280 km. The thermal profile near the top of the atmosphere is mostly determined by the incoming radiation. Due to this, the exobase temperatures of the different models vary between 1130 K and 1180 K, even though the base temperatures varied by

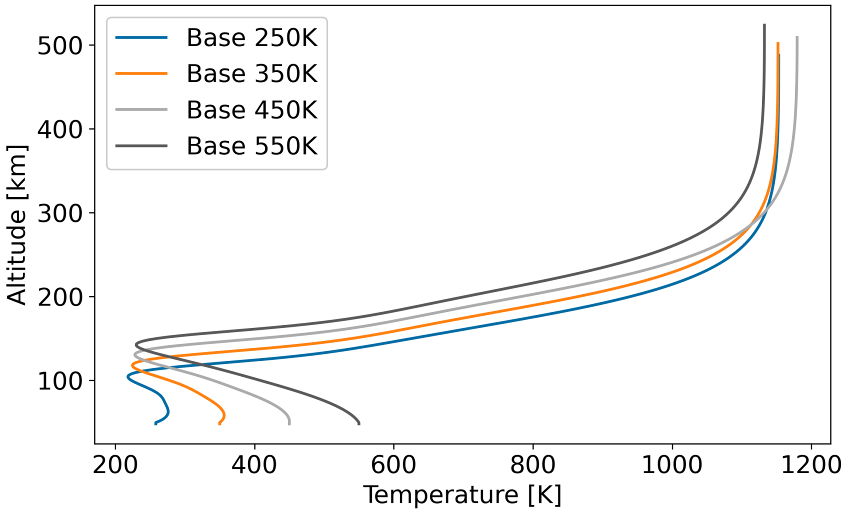

Figure 3.1: Altitude-temperature profiles for an Earth-like model with varying lower boundary temperatures.

300 K. As we will look primarily at higher irradiances, the impact of the star will only become stronger. In the case of transit spectroscopy, the conditions of these impacted regions are more important as they impact the spectrum of the planet. However, for the calculation of the mass loss, the lower boundary is not as impactful and we will assume the Earth value of 267.2 K.

In Section 2.5, we already saw the difference between an N_2-dominated atmosphere (like Earth) and a CO_2-dominated atmosphere (like Venus). Due to its strong cooling effect, we will focus on varying the CO_2 mixing ratio, assuming that the rest of the atmosphere is composed of N_2. In Section 3.2.2 we will look at these variations and their effects in more detail.

3.1.2 Stellar spectrum

The next parameter is the input spectrum. Of course, the total intensity of the spectrum influences the atmosphere, as a more intense spectrum will deposit more energy. However, the exact shape of the spectrum can also strongly influence the atmosphere. Figure 3.2 shows the XUV section of the Sun's spectrum in blue. This spectrum is an empirical spectrum of the current Sun taken from Claire et al. (2012). We can then compare the solar spectrum to the spectrum of a low-mass star, such as for example TRAPPIST-1, a 0.0802 ± 0.0073 $M_\odot$, of spectral type M8 (Gillon et al. 2017). The orange line in Figure 3.2 shows a modelled spectrum of TRAPPIST-1 from the Mega-MUSCLES survey (Wilson et al. 2021). In the figure, the spectrum was scaled to 0.512 au, such that the flux integrated from 10 nm to 121 nm is the same as the irradiance received on Earth. To scale this spectrum, we assumed a distance from Earth to TRAPPIST-1 of 12.43 pc, as was used in Wilson et al. (2021). Comparing these two spectra, we can see how the 'blackbody' section of the spectrum is much fainter for the M-type star, which is why the habitable zones of later-type stars are closer than for solar-type stars. Towards the X-ray end of the spectrum, we can see that low-mass stars can reach spectral irradiances similar to or even higher than the Sun. The X-ray luminosity of the Mega-MUSCLES spectrum calculated from 0.517 - 12.4 nm, is 3.4×10^{26} erg s^{-1}, which corresponds to the low end of the luminosity range determined by Wheatley et al. (2017) using observations from XMM-Newton.

The right axis of Figure 3.2 and the dashed grey line show the collisional cross-section of photo-ionisation and dissociation reactions (Huebner & Mukherjee 2015) of the average particle of the Earth's atmosphere. We can see that the atmosphere is particularly sensitive to the Extreme ultraviolet (EUV) range between 10 nm and 100 nm. Unfortunately, this wavelength range is also strongly absorbed by the interstellar medium, making the reconstruction of the spectra of stars very uncertain. Wilson et al. (2021) describe that this section of the spectrum is reconstructed using the Differential Emission Measure

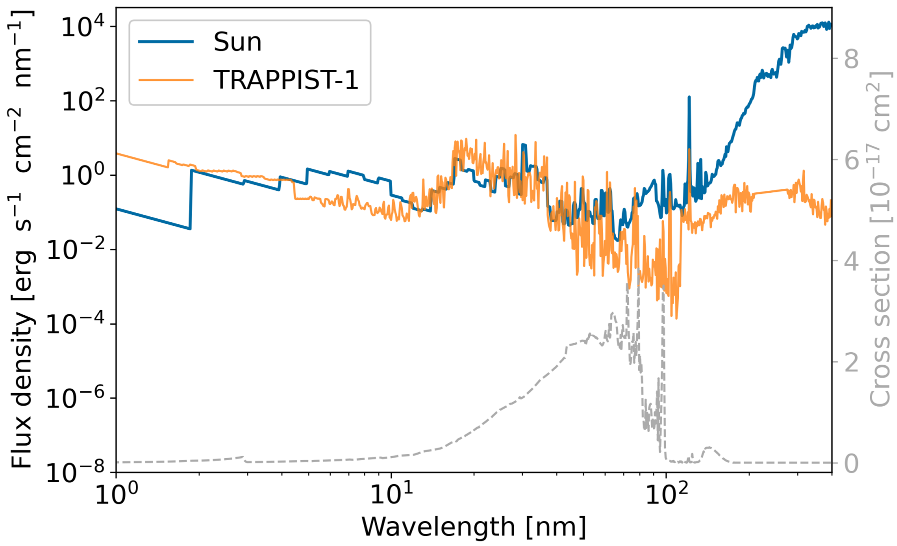

Figure 3.2: Spectrum of the Sun (Claire et al. 2012) in blue and the TRAPPIST-1 (Wilson et al. 2021) in orange. The grey dashed line shows the collisional cross-section of the average particle in Earth's atmosphere.

(DEM), a scaling relation for the emission from the optically thin plasma. This scaling relation uses lines in the observable X-ray and FUV to estimate the EUV range. Though this is a common approach, it requires small optical depths in the corona, which might not be the case for each emission line, particularly looking at M-type stars (Fontenla et al. 2016).

However, it is interesting to take a brief look at the impact of the precise stellar spectrum on the thermal profile of the planet. The thermal profiles in Figure 3.3 show how an Earth-like planet with an atmosphere composed of 1% N_2-99% CO_2 reacts to the solar spectrum and the TRAPPIST-1 spectrum. The left panel shows the profile of a planet receiving the irradiance of Earth between 10 nm to 121 nm, which means 1 au in the Solar System and 0.512 au in the TRAPPIST-1 system. The right panel shows the model of a planet receiving four times the irradiance in this wavelength range, i.e. 0.5 au for the Solar System and 0.256 au for the TRAPPIST-1 system.

These profiles show that the upper atmospheres with the same composition and irradiation can have a different structure. The model using the solar spectrum is colder at most altitudes compared to the synthetic TRAPPIST-1 spectrum. This is even though, as we can see in Figure 3.2, the atmosphere in the model using the solar spectrum receives more total energy due to the stronger photospheric radiation. Running models excluding sections of the UV spectrum with $\lambda > 121$ nm and X-ray ($\lambda <$ 10 nm) resulted in similar thermal profiles. This seems to indicate that the EUV section of the spectrum, i.e. wavelengths between 10 nm and 121 nm, has a particularly strong influence on the shape of the thermal profile. It is important to note that the Mega-MUSCLES survey spectrum was scaled such that the irradiance of this wavelength range is equal to that of the solar spectrum, even though the strength of individual emission lines varies. A peak in the cross-section of the dissociation reaction of CO_2 into CO and O around 109 nm seems to be the main cause of the difference in the thermal profile. In the TRAPPIST-1 spectrum, the spectral irradiance at this wavelength is almost two orders of magnitude below the observed solar spectrum. This region of the Mega-MUSCLES spectrum coincides with a transition from the Phoenix model to the DEM. Figure 3.2 shows that cross-sections of photoreactions of an N_2 dominated atmosphere also have several peaks in this wavelength range.

To minimise the number of additional models and assumptions we make, we will use the solar spectrum throughout the rest of this work. The models in the remainder of this chapter will be exposed to different irradiances by scaling the entire spectrum between 1 nm and 430 nm. Within the Solar System, this scaling can be translated to the distance to the Sun, but outside of the Solar System, we will need an additional scaling to account for the luminosity of the star. Since we already saw that

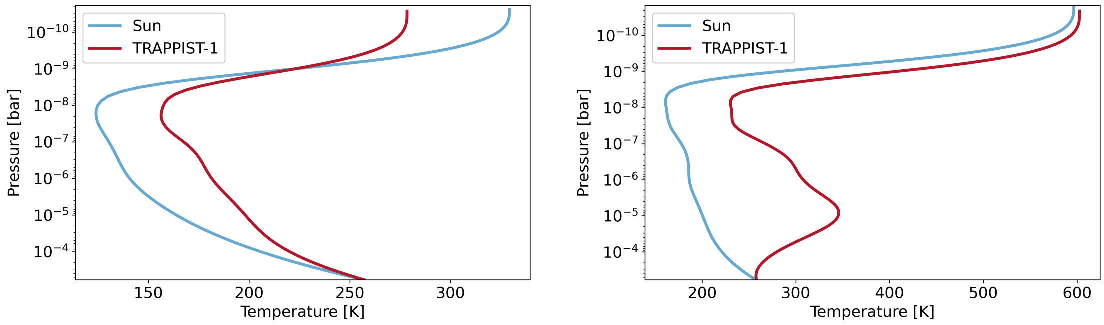

Figure 3.3: Pressure-temperature profiles of a 1% N_2-99% CO_2 atmosphere exposed to the solar spectrum (in blue) and the TRAPPIST-1 spectrum (in red). Left: Spectrum with an irradiance of Earth between 10 nm and 121 nm. Right: Spectrum with an irradiance of four times Earth, between 10 nm and 121 nm.

common compositions of secondary atmospheres are particularly sensitive to the EUV spectrum of a star, we will use the wavelength range between 10 and 92 nm and define the EUV flux density at 1 au as $F_{EUV,\oplus} = 1.1 \times 10^{28}$ erg/cm^2. This irradiance will allow us to calculate the distance at which a planet around a different star experiences conditions similar to Earth.

In order to keep our approach as general as possible for a wide array of stars, we use the stellar parameters presented in Johnstone et al. (2021a). In this work, the evolution of the luminosity of stars with masses between 1.2 and 0.1 $M_\odot$ is modelled for many different initial rotation rates, as this parameter strongly influences the XUV evolution of a star. The authors define a star as a slow rotator if its initial rotation rate corresponds to the 5th percentile of the distribution of possible initial rotation rates. Similarly, a medium rotator is defined as the 50th percentile and a fast rotator is defined as the 95th percentile. In Section 3.4, we will look at the impact of stellar mass and initial rotation rate on the atmospheric retention distances.

3.2 Mass loss models

3.2.1 Atmosphere structure

To calculate the Jeans escape of a model atmosphere, we will need the temperature and altitude of the exobase. First, let us take a closer look at the atmospheric structure of the model atmospheres and the impact of the chemical composition and stellar irradiance. Figure 3.4 shows an example of pressure-temperature profiles for different atmospheric compositions. These are models of a planet of 1 $M_\oplus$ exposed to 1 $F_{EUV,\oplus}$. This figure clearly demonstrates how an increased CO_2 mixing ratio results in a lower temperature in the upper regions of the atmosphere. In Section 2.5, we saw this effect also when comparing the Earth model to the Venus model. The lower temperature in the upper atmosphere, particularly at the exobase, would lead to a lower atmospheric loss.

The structure of the atmosphere and, consequently, the cooling are also affected by the stellar irradiance. Figure 3.5 shows how a 1 $M_\oplus$ with an atmospheric composition of 1% N_2 and 99% CO_2 reacts to different irradiances. The top row of the figure shows the mixing ratios of abundant species and their associated ions throughout the atmosphere. The second row of Figure 3.5 shows the vertical distribution of CO_2 and O cooling. In the first column, we can see the planet exposed to 1 $F_{EUV,\oplus}$. In this model, we see that the entire atmosphere is dominated by CO_2, which also leads to CO_2 cooling being the dominant cooling mechanism. A model with six times Earth's irradiance shows a similar structure below an altitude of 100 km. Above this altitude, we can see that the CO_2 is photodissociated into atomic oxygen and ions. In the second row of this case, we can see that even though O becomes the dominant species, the CO_2 cooling remains the dominant cooling mechanism up to approximately 180 km. This further demonstrates how strong the CO_2 cooling is. In the high-irradiance scenario, the upper layers of the atmosphere become increasingly more ionised. Though not part of our loss calculations, ions are

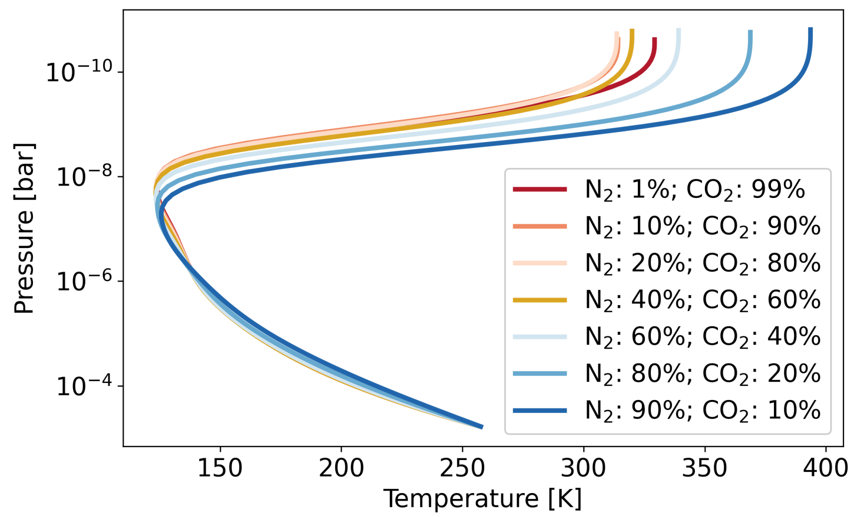

Figure 3.4: Pressure-temperature profiles for a 1 $M_\oplus$ planet receiving 1 $F_{\mathrm{EUV},\oplus}$. The colours indicate the different bulk compositions.

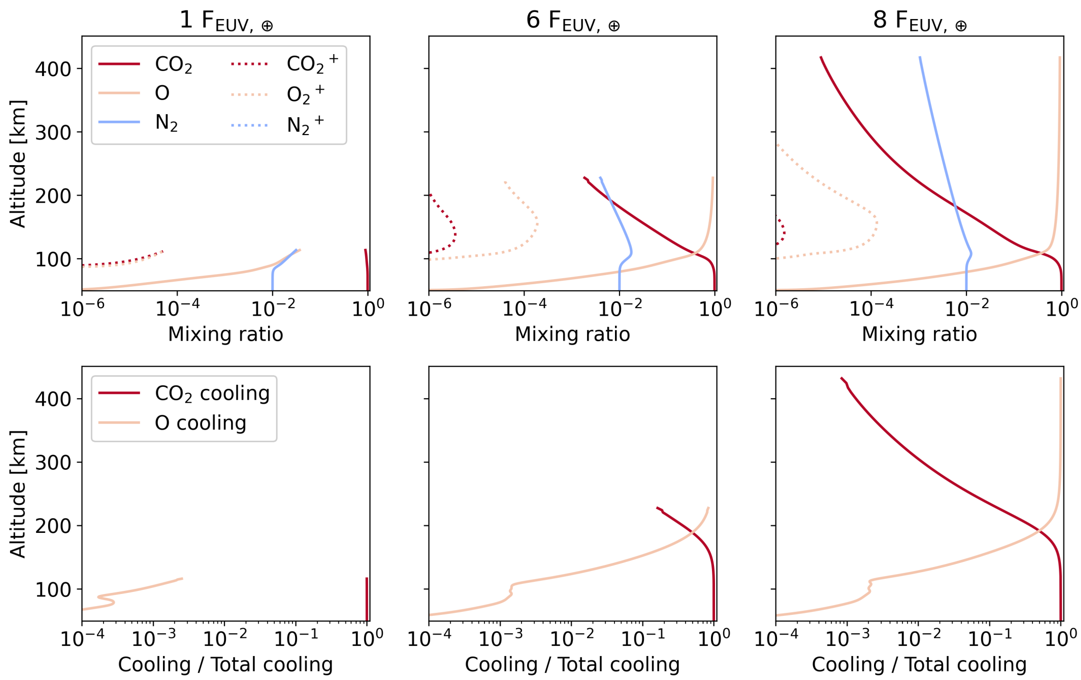

Figure 3.5: Mixing ratios and cooling contributions of Kompot models. Top row: Mixing ratios of several neutral species (indicated by solid lines) and ionised species (indicated by dotted lines) in the simulated domain. Bottom row: Contributions of different cooling mechanisms at different altitudes. Each column corresponds to different levels of irradiation, namely 1, 6, and 8 $F_{\mathrm{EUV},\oplus}$. All models presented in this figure are of a 1 $M_\oplus$ planet with an atmosphere composed of 1% N_2-99% CO_2.

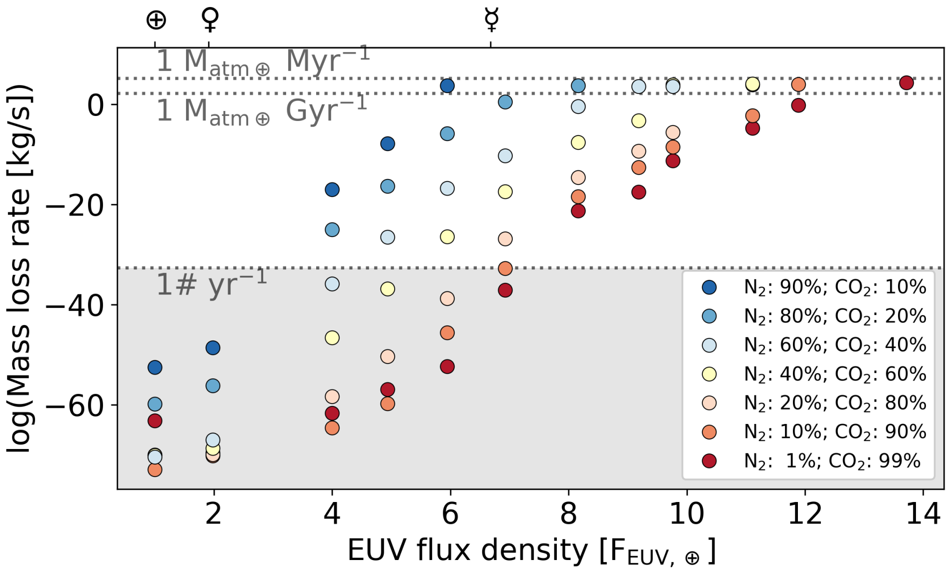

Figure 3.6: Abundance-weighted average Jeans escape for a 1 $M_\oplus$ planet. Colours indicate different chemical compositions. The ticks on the top x-axis indicate the EUV flux received by the Solar System planets (given by their astronomical symbol). The horizontal lines indicate mass-loss rates in different units. The grey area indicates negligible loss rates.

more susceptible to non-thermal losses, which would increase our estimates as demonstrated for early Earth by Grasser et al. (2023). In Section 1.4.1, we discussed how the Jeans escape is calculated. This mass loss rate depends on the masses and abundances of the escaping particles. The dissociation of molecules into atoms at the top of the atmosphere results in lighter particles escaping more easily.

In the high-irradiance case, the CO_2 cooling is still the dominant process in the lower section of the atmosphere. The photons emitted by CO_2 molecules need to pass through a larger atmosphere to escape and cool the atmosphere. This process remains efficient because the calculation of the escape probability depends on the number density of CO_2 at higher altitudes. This species dissociates and leaves the upper reaches of the atmosphere transparent for the CO_2 cooling. The dissociated oxygen particles result in their own cooling, though in our model, O cooling is not as efficient as CO_2 cooling, resulting in a rapid expansion of the atmosphere between the 6 and 8 $F_{\mathrm{EUV},\oplus}$ case. Nakayama et al. (2022) claim that a more complex treatment of atomic line cooling by adding more emission lines could result in a cooler atmosphere and lower mass loss rate. When more emission lines are included, the escape probability becomes increasingly important as other species can reabsorb the photons before reaching the top of the atmosphere. Underestimating how many photons get reabsorbed can result in an overestimation of the cooling. Though a thorough analysis of these additional cooling mechanisms will be the subject of future work, it is important to keep the possible limitations of the models in mind.

3.2.2 Composition variation

In this section, we will take a look at the dependence of the atmospheric loss on the chemical composition of the atmosphere. To study this, we modelled atmospheres with chemical compositions varying from 10% CO_2 and 90% N_2 to 99% CO_2 and 1% N_2. These compositions represent common atmospheric compositions of rocky planets, with a focus on CO_2, which has a strong cooling effect and N_2, which tends to be much more inert (compared to, for example, CO_2, H_2O, or O_2) in the atmosphere.

Figure 3.6 shows how these atmospheric compositions influence the mass loss rate for an Earth-mass planet at different irradiances. The x-axis of the figure shows the irradiance of the various models, where, for reference, the top x-axis shows where the Solar System planets would fall on this scale. The

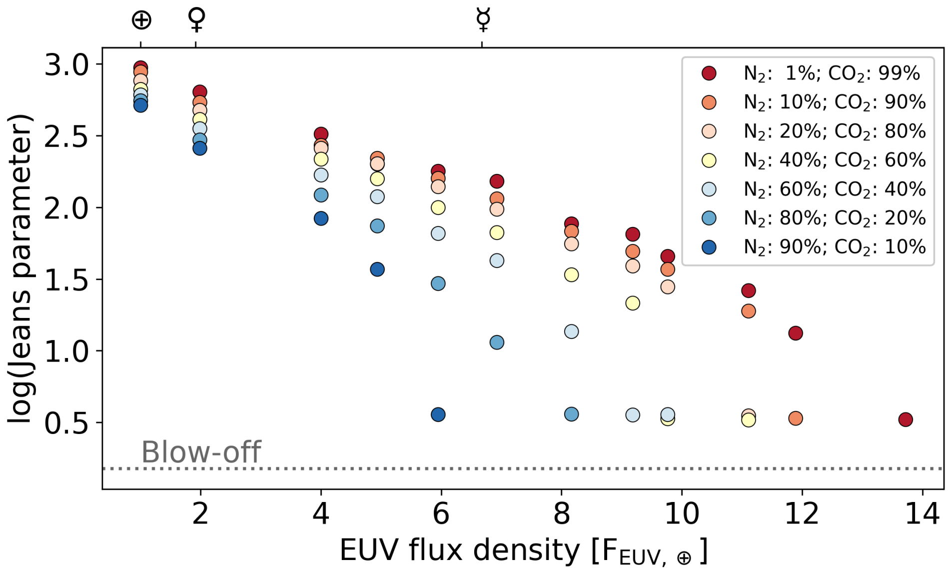

Figure 3.7: Jeans parameter for a 1 $M_{\oplus}$ planet. Colours indicate different chemical compositions. The ticks on the top x-axis indicate the EUV flux received by the Solar System planets (given by their astronomical symbol). The horizontal line indicates the blow-off limit.

mass loss rate shown on the y-axis represents the average mass loss rate of the model, weighted by the abundance of each species at the exobase. This weighting of the average prevents the value from being skewed by lighter species, which are not abundant in the atmosphere. For example, C weighs 12 amu whilst O weighs 16 amu, meaning C is lost more easily, though in a CO_2 dominated atmosphere, there is only one C atom for every two O atoms. As the models are in a steady state, they will not reflect the more limited reservoir of a particular element and could thus overestimate the mass loss rate. It is also important to note that the y-axis covers over 70 orders of magnitude, and some of these results are numerical without any physical meaning. The grey shaded area indicates mass loss rates of less than a single particle per year and should be considered as negligible. For example, at 1 $F_{\mathrm{EUV},\oplus}$ the 99% CO_2 model seems to have a much higher mass loss rate than the same model at 2 $F_{\mathrm{EUV},\oplus}$. These losses, however, are orders of magnitude lower than the loss of a single electron over the age of the Universe. Such small values can easily change by orders of magnitude due to a discretisation of the atmosphere when a different cell is considered to be the exobase, or by small fluctuations of the exobase temperature. Because of this, the mass loss rates within the grey shaded area should be considered as zero. On the other hand, the upper two dashed lines indicate significant mass loss rates. The lower of these lines shows the loss of the Earth's atmosphere (5.14×10^{18} kg, Trenberth & Smith 2005) in one billion years, whilst the upper line indicates the loss of the Earth's atmosphere in one million years, assuming a constant loss rate.

In Figure 3.6, we can see that all compositions for an Earth or Venus flux density lead to negligible mass loss rates. As the irradiance increases, the mass loss rate increases. The shaded area shows that up to 5 $F_{\mathrm{XUV},\oplus}$ Jeans escape is negligible for most chemical compositions. By approximately 6 to 7 $F_{\mathrm{XUV},\oplus}$, which resembles the conditions at Mercury's orbital distance, the N_2 dominated atmosphere reaches catastrophic loss rates. At higher flux densities, the model reaches temperatures at which some of the analytic expressions for heat exchange used in the code are no longer valid. At 8 $F_{\mathrm{EUV},\oplus}$ the atmosphere with 80% N_2 reaches the same mass-loss rate. At increasingly high irradiances, more compositions reach these extreme mass loss rates, until the 99% CO_2 model reaches this loss rate at 14 $F_{\mathrm{EUV},\oplus}$.

Another point to keep in mind is the second type of thermal losses: hydrodynamic losses. Öpik (1963) defined a blow-off condition, the point when the thermal energy of the atmosphere exceeds the gravitational energy. This would lead the atmosphere to blow away. This condition is reached when the Jeans parameter (see Equation 1.3) is lower than 1.5. Figure 3.7 shows the Jeans parameter of the models shown in 3.6. The dashed horizontal line shows the Jeans parameter of 1.5, or 0.4 on the logarithmic y-axis. The figure shows that none of the models reach this blow-off condition, even though these models reach very high mass loss rates as shown in Figure 3.6. Even though the blow-off condition was traditionally considered the transition point between Jeans escape and hydrodynamic escape, research by Tian et al. (2008) shows that an atmosphere reaches the hydrodynamic flow regime before it reaches this blow-off condition. In this regime, other effects become important, such as hydrodynamic flows and adiabatic cooling. Mass loss in the hydrodynamic regime is estimated to be orders of magnitude higher than Jeans escape (Johnstone et al. 2019). Tian et al. (2008) determine that an Earth-like atmosphere would reach the hydrodynamic regime between 7000 and 8000 K, or about 5 times Earth's current EUV flux.

The change to the hydrodynamic regime and non-thermal losses further emphasise that the mass loss rates of these models are likely an underestimation of the actual losses a planet under those conditions would experience. With this, we have already assessed two possible factors, namely composition and irradiance, though there is one more very impactful factor to look at before we get into some results.

3.2.3 Mass variation

When we look at the planets in the Solar System, we can see that even though Mars is farther from the Sun, it has a much more tenuous atmosphere. When we compare Earth and Mars, a parameter which stands out is the difference in planetary mass, namely 1 $M_\oplus$ compared to 0.151 $M_\oplus$. A lower mass results in a lower escape velocity, which means that a particle needs less energy to escape from the planet. However, looking further out in the Solar System, we find Saturn's moon Titan. The 0.0225 $M_\oplus$ moon holds onto an atmosphere with a surface pressure of approximately 1.5 bar. This indicates that smaller objects can retain their atmosphere, though likely only at much larger orbital distances.

To study this, we repeat the models discussed in the previous section with a lower planetary mass. These models assume a surface radius 0.93 $R_\oplus$ so that the density of the planet remains 5.5 g/cm^3. The upper panel of Figure 3.8 shows the averaged mass loss rates for different atmospheric compositions and irradiances for the smaller planet. We can see that the models follow a similar pattern of increasing loss with increasing irradiance and decreasing CO_2 content. As expected, the models reach the catastrophic mass loss rate at a smaller irradiance, as less energy is required to reach the lower escape velocity. We can see how none of these models reaches the 14 $F_{\mathrm{EUV},\oplus}$ irradiance, which the 1 $M_\oplus$ did reach in Figure 3.7. Similarly, at an irradiance comparable to Mercury, an atmosphere composed of 80% N_2 and 20% CO_2 could be retained around a 1 $M_\oplus$ planet but not a 0.8 $M_\oplus$ planet. An unfortunate point to note is the seeming break in the upwards trend at 11 $F_{\mathrm{EUV},\oplus}$ between the 90% CO_2 and 99% CO_2 model. This higher mass loss rate in the 99% CO_2 model is likely due to the energy exchange mechanism between electrons and neutrals through the CO-vibrational excitation. This energy exchange mechanism was excluded in the 99% CO_2 model due to the approximation breaking down when the number density of CO molecules is too high. This removes a pathway for energy to be transferred between the neutrals and electrons, leading to more energy being stored in the neutrals and consequently making the mass loss rate higher. Solving this problem would require a different analytical approximation, but this falls outside the scope of this work.

The lower panel of Figure 3.8 shows the mass loss rates for a planet of a 1.2 $M_\oplus$. This planet's radius was scaled to 1.06 $R_\oplus$ to also retain a 5.5 g/cm^3 density. Particles in the models have to overcome a higher escape velocity to escape from the planet. This results in models having lower mass loss rates compared to the other planetary masses. For example, the N_2-dominated model only reaches the catastrophic loss at Mercury-like irradiances. This shows that higher masses can hold onto atmospheres under a wider array of models.

A problem that planets with higher masses run into is that they may not be able to outgas an atmosphere. Models of stagnant-lid planets have shown that a planet with masses above 5 $M_\oplus$ might not be efficient at outgassing material from the mantle (Noack et al. 2017; Dorn et al. 2018). This occurs due to the pressure-dependent viscosity lowering the convection in the lower mantle. This causes less material with volatiles to reach the top of the mantle, where it could outgas to build up the atmosphere. Though planets reaching such masses will be the topic of an upcoming study, we can already see from Figure 3.8 that there will be careful balancing required between finding planets that are large enough to retain their atmosphere effectively and those that are small enough to outgas their mantles. This leads us to the next section on how atmospheres can be replenished.

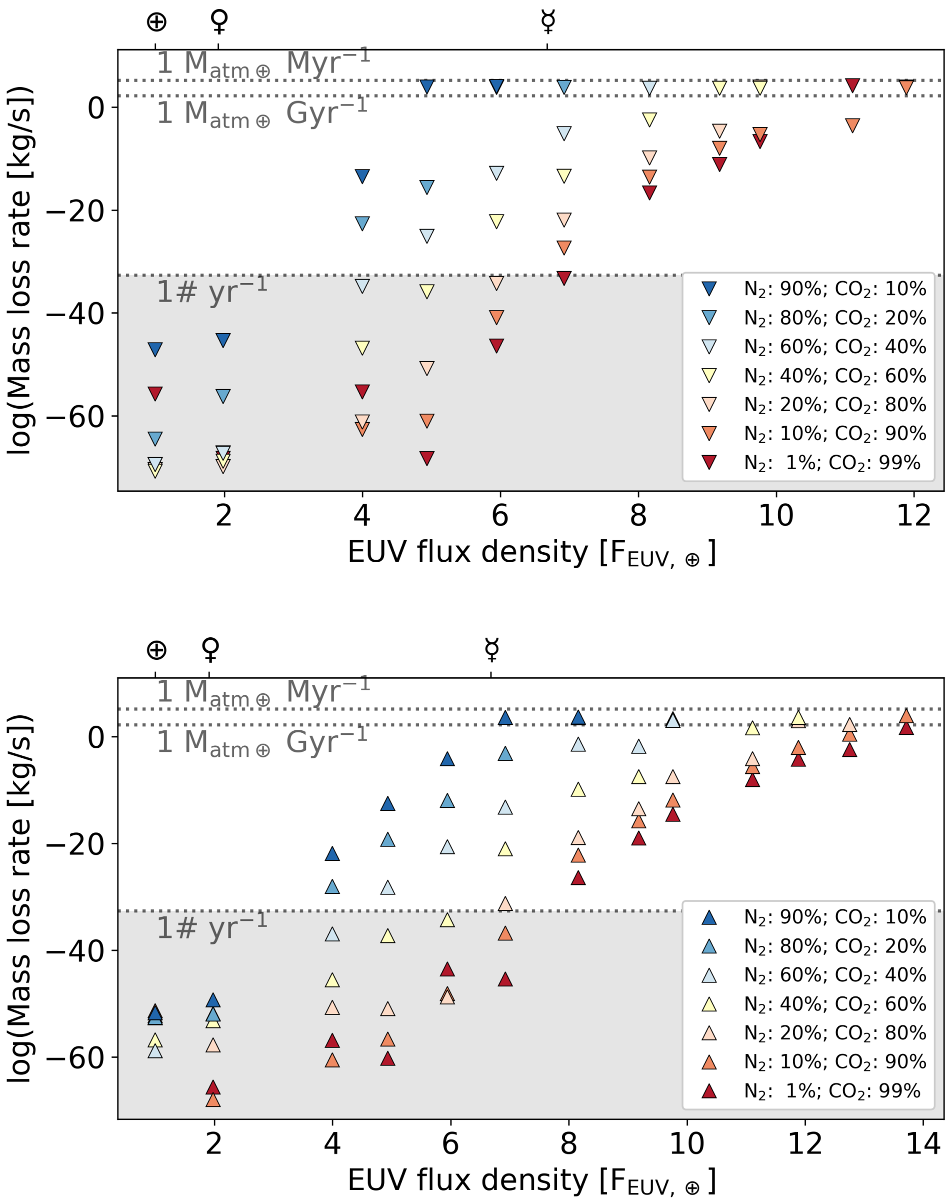

Figure 3.8: Abundance-weighted average Jeans escape for a 0.8 $M_\oplus$ (upper) and a 1.2 $M_\oplus$ (lower) planet. Colours indicate different chemical compositions. The ticks on the top x-axis indicate the EUV flux received by the Solar System planets (given by their astronomical symbol). The horizontal lines indicate mass-loss rates in different units. The grey area indicates negligible loss rates.

3.2.4 Mass replenishment

If we want to determine if an atmosphere is lost, it is important to take into account the amount of atmosphere that is replenished. The entire volatile content of a planet will not be in the atmosphere entirely throughout its lifetime, but rather some amount will be retained in the mantle, which can be outgassed over time (summarised in Fig. 1 of Lichtenberg et al. 2023). During the early stages of a planet, global magma oceans and their solidification lead to the first buildup of a secondary atmosphere, which can be on the order of tens to thousands of bars (Elkins-Tanton 2008). The depth of the magma ocean, size of the planet, and the composition of the planet not only determine the thickness of the atmosphere but also its composition (as summarised in Lammer et al. 2018).

However, the entire atmosphere does not have to be outgassed during this early stage. For example, Earth continues to replenish its atmosphere through volcanism, which provides 1.0×10^4 kg/s (7.5 Tmol/yr) of CO_2 and 5.4×10^4 kg/s (95 Tmol/yr) of H_2O (Catling & Kasting 2017, p. 203). Additionally, as summarised in Lammer et al. (2018, Section 5), the delivery of nitrogen to the atmosphere can also occur through volcanism in small amounts (less than 1% of all outgassed material), though for present-day Earth, the nitrogen cycle is inextricably tied to the biosphere, making it more complicated to determine for exoplanets. Additionally, models by Guimond et al. (2021) show that for stagnant lid planets similar to the early Earth, the outgassing rates can reach about 1.4×10^4 kg/s (10 Tmol/yr). In another study, Baumeister et al. (2023) investigated the planetary interior and outgassing evolution of a large range of planets with different mantle redox states, volatile contents, masses, and sizes. That study showed that volcanic outgassing rates can stay at about 10^2 kg/s (7×10^{-2} Tmol/yr) of CO_2 for multiple gigayears. The timescale over which the rocky planets stay volcanically active is usually defined by the presence of melt in the mantle. Generally, this is estimated through the thermal budget of the planet at formation. However, other effects such as tidal and possibly induction heating can continue to influence the amount of melt (Kislyakova et al. 2017).

In order to compare the outgassing rates, typically given in units of Tmol/yr, to the mass-loss rates, which are often expressed in Earth oceans, we need to briefly address units. In this study, we define the catastrophic mass loss rate as the entirety of Earth's atmosphere being lost within 10 Myr, or approximately 1.6×10^4 kg/s, with Earth's atmosphere weighing 5.14×10^{18} kg (Trenberth & Smith 2005). Such a mass loss rate falls just above the lower of the dashed lines in Figures 3.7 and 3.8. This loss rate would be equivalent to a loss of 0.004 Earth's oceans in 10 Myr, assuming the mass of the Earth's ocean to be 1.4×10^{21} kg (Wolf & Toon 2015). On the other hand, a pure CO_2 outgassing rate of 1.7×10^4 kg/s translates to about 12 Tmol/yr. This outgassing rate is on the higher end of both measurements and models, though higher rates are achievable, in particular during the early stages of planet formation.

Using our modelled atmospheres, we can find the EUV irradiance at which this extreme mass loss rate is reached. We will then use the irradiance to define the minimal orbital distance around different types of stars where a planet can retain its atmosphere, which we defined as the Atmospheric Retention Distance (ARD) in Van Looveren et al. (2025). To get a better idea of the meaning and implications of the ARD, we will apply it to the Solar System in the next section.

3.3 Solar System

The Sun (by definition) is a 1 $M_\odot$ star and likely started out as a slow rotator (Johnstone et al. 2021b). Using the corresponding model from Johnstone et al. (2021a), we can calculate the ARD for the Solar System. Figure 3.9 shows the ARD for the different models using different coloured lines and their evolution over time. At smaller distances (i.e. below the coloured lines), the escape rate is greater, making the presence of an atmosphere even less likely. On the other hand, at distances greater than the retention distance, an atmosphere can be maintained over long timescales or even increased if the outgassing rate is high enough. The green shaded area in the figure indicates the HZ, which is calculated based on the bolometric luminosity of the stellar model.

Here we can see how the bolometric luminosity of a Sun-like star, which defines the HZ, does not evolve the same way as the EUV luminosity, which we use to determine the ARDs. While the bolometric luminosity stays almost constant over much of the star's main-sequence life and gradually increases

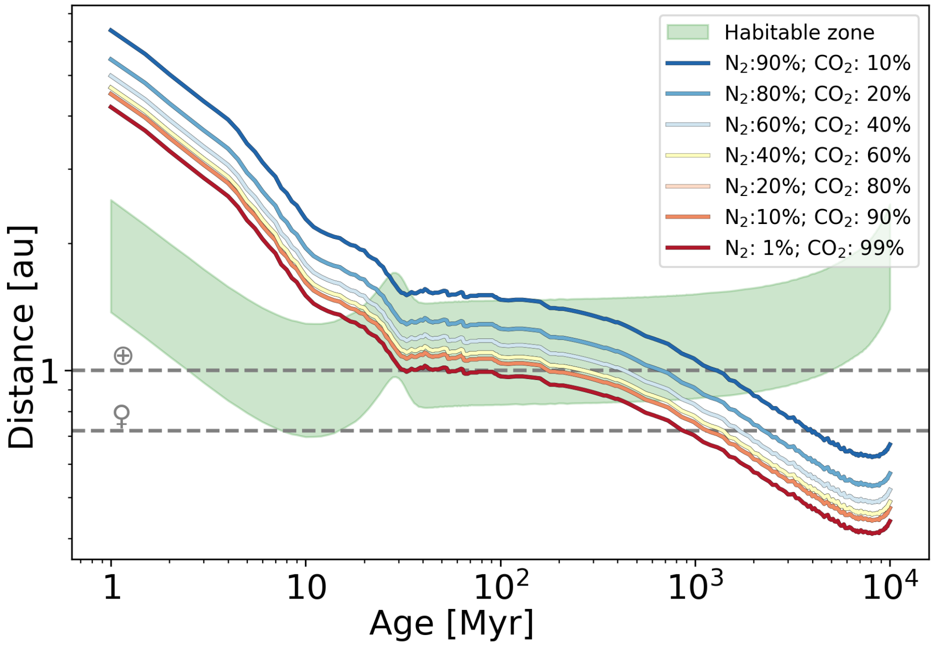

Figure 3.9: Atmosphere retention distance for different atmospheric compositions, indicated by different colours, over time for a 1 $M_\odot$ slow rotating star. Above these lines, atmospheres can be retained. The green shaded area indicates the habitable zone. The dashed lines indicate Earth's and Venus' semi-major axes, denoted by their corresponding symbols.

towards the end of it, the EUV luminosity declines substantially over time due to stellar spin-down and the consequent weakening of the magnetic dynamo. This means that certain orbits which are habitable at one point might not be at a later point in time, though this zone does not change drastically over the lifetime of the Solar System. Earth, for example, falls within the HZ for almost the entire timeline.

Looking at the first 25 Myr in Figure 3.9, we see that a 1 au orbit is closer than the ARD. At this point in time it is unlikely that the secondary atmosphere is fully formed yet. Over this short period, the integrated mass loss also only adds up to several tens of bars of atmosphere, which is likely less than the available atmospheric inventory. During this initial era, the planet could still be holding onto a primary atmosphere. The stripping of this atmosphere would be an interesting question, though this requires models with hydrogen-dominated atmospheres. Other studies, such as Kubyshkina et al. (2018) and Owen & Wu (2016) focus on the mass loss rates of hydrogen-dominated atmospheres.

The period immediately following this highly irradiated time would coincide with the estimated Moon-forming impact between 30 and $\sim$100 Myr (e.g., Hopkins et al. 2008; Yu & Jacobsen 2011; Fu et al. 2023). This impact would have resulted in a magma ocean, which is estimated to have led to an outgassing of 70 bars of CO_2 (Gebauer et al. 2020). Figure 3.9 shows that at this time, the mass-loss rate would still be of the order of 1 $M_{\mathrm{atm},\oplus}$/10 Myr. Throughout the remainder of the Hadean, until approximately 600 Myr, the losses decrease as the EUV luminosity decreases. Integrating the mass loss at Earth's distance from 100 Myr to 600 Myr, we find a total mass loss due to Jeans escape of the order of 3×10^{19} kg (around 5.5 $M_{\mathrm{atm},\oplus}$). This is well below the initial atmospheric mass, particularly if the Earth continues to release more volatiles, as discussed in the previous section.

This loss rate would leave the Earth with over 60 bar of CO_2 at the start of the Archean. Isotope measurements of quartz from the early-Archean ($\sim$600-1600 Myr) indicate that the surface pressure was only of the order of 1-2 bar (Marty et al. 2013). Gas bubbles in basalt also indicate the Earth would have had a partial CO_2 pressure of 0.23-0.5 bar by the late Archean ($\sim$1900 Myr) (Som et al. 2016). This shows that either the Jeans escape predicted by our model is likely not the dominant loss mechanism or the initial outgassing was not as large. The additional atmospheric mass compared to the geological record could have been lost to space through hydrodynamic escape (Tian et al. 2008), or non-thermal loss processes (Kislyakova et al. 2020; Grasser et al. 2023). Additionally, water and CO_2 would have been returned to the mantle through chemical weathering, dissolution into (magma) oceans, subduction, and sequestration into the crust (as summarised in Lammer et al. 2018). On Earth, the carbon and nitrogen cycles are strongly influenced by the oceans, plate tectonics, and life (Lammer et al. 2018, 2019). Estimates of atmospheric N_2 contents during the middle Archean (1100–1600 Myr) from fluid inclusions in quartz indicate a partial pressure between 0.5 and 1.1 bar (Marty et al. 2013). The partial CO_2 pressure is estimated to be lower than 0.7 bar, meaning the atmosphere reached a roughly 50%/50% CO_2/N_2 composition (Marty et al. 2013). It is interesting to note that this estimated chemical composition is dated to roughly the same time as the model of the 40% CO_2 atmosphere crosses 1 au. However, it is also important to realise that there are large uncertainties associated with indirect measurements of the early atmosphere.

Next, let us look at Venus, another rocky planet with a thick atmosphere, which experiences an even greater irradiance than Earth. Figure 3.9 shows Venus' orbital distance by the lower dashed line. At a distance of 0.73 au, Venus is closer in than the ARD up until 1000 Myr. Unfortunately, Venus has very limited geological (or cytherological, to introduce another adjective form of Venus based on Cythera, the birth island of the namesake goddess) data, thus we cannot constrain the early history of Venus as we can for Earth. Radar data of Venus indicates that the planet underwent extended resurfacing at ages between 3600 and 4400 Myr (i.e. 1 to 0.2 Gyr ago) (Kreslavsky et al. 2015). In the research by Kreslavsky et al. (2015), the authors also conclude that due to the size and distribution of craters, the atmospheric shielding must have remained similar throughout this period of Venus' history. The loss models we calculated here predict that the mass-loss rate during this period would be relatively low for a CO_2-dominated atmosphere. Other indirect methods have been used to constrain the earlier history of Venus, such as isotopic ratios (Avice et al. 2022). In particular, Venus' elevated isotopic ratio of D/H seems to indicate that it experienced greater atmospheric loss (Donahue et al. 1982). If we assume the largest mass loss rate over the period from 100 to 1000 Myr, the loss would amount to the order of 6×10^{20} kg (around 124 $M_{atm,\oplus}$). However, this would be a lower limit as the irradiance at 0.72 au at 100 Myr is 24 $F_{\mathcal{EUV}\oplus}$ and decreases to 13 $F_{\mathcal{EUV}\oplus}$, which is greater than the maximum modelled irradiance. This seems like a large loss, especially when we compare it to estimates of the 70 bar outgassed by Earth's magma oceans. The atmospheric losses during this early and highly irradiated time could be avoided if the secondary atmosphere only built up gradually over an extended amount of time (beyond 1000 Myr) rather than in a catastrophic outgassing event. Models such as those presented by Baumeister et al. (2023), which we discussed in Section 3.2.4, show that outgassing can continue for billions of years. Isotope ratios of argon in the Venusian atmosphere have also been used to demonstrate that a stagnant-lid model can explain the current environment of Venus (O'Rourke & Korenaga 2015).

These models demonstrate that there is a complicated interplay between the atmosphere and interiors of rocky planets. There are, however, many factors which leave us with great uncertainty when it comes to determining the early history of planets and the formation of secondary atmospheres, for example, the shielding by a primary atmosphere, the presence or absence of plate tectonics, etc. For Earth-like planets and orbital distances, global solidification is estimated to finalise between the ages of 0.1 to 100 Myr, although this cool-down period can be longer if the planet experiences higher irradiance (Lichtenberg et al. 2023). Because of this, and as we saw for Venus, the first 1000 Myr can be very uncertain. To make a more conservative estimate, when looking at other stellar masses, we will disregard the first 1000 Myr to determine reliable ARDs. This assumption encapsulates the possibility of early, very dense atmospheres which erode to thinner atmospheres in early stages (as we surmise for Earth) and significant outgassing over prolonged periods of time (as might be the case for Venus). We can, of course, think of scenarios where a planet could retain an atmosphere at an orbital distance closer to its host star than the ARD at some point in time. A planet could, for example, migrate inwards, or a giant impact could melt the surface again at a point after 1000 Myr. To keep the results as general as possible, we will assume that planets inside the ARD at 1000 Myr are unlikely to retain a significant atmosphere.

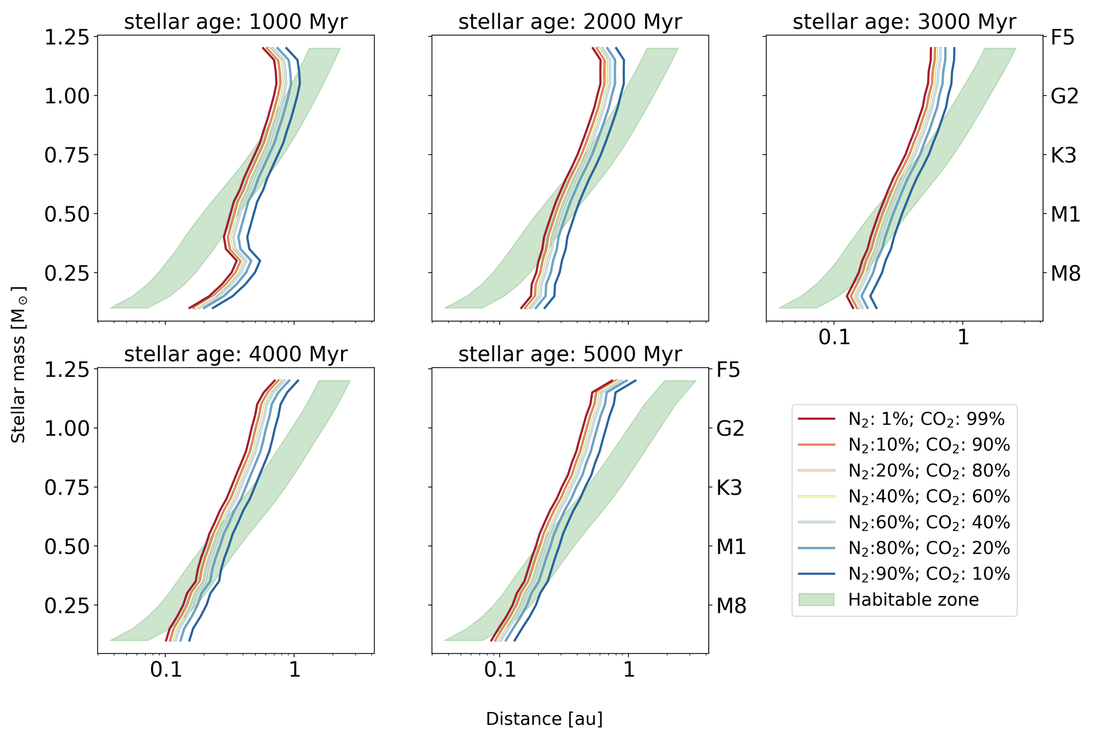

Figure 3.10: Atmosphere retention distances for different stellar masses, with different atmospheric compositions indicated by different colours. Right of these lines, atmospheres can be retained. The green shaded area indicates the habitable zone. Each panel indicates a different stellar age.

3.4 Stellar systems

3.4.1 Stellar mass

Now, let us move beyond the Solar System and focus on different stellar masses. Every panel of Figure 3.10 shows the orbital distance on the x-axis and the stellar mass on the y-axis. The HZ is indicated on each panel by the green shaded area, whilst the ARDs are indicated by different colours for atmospheric compositions. Because the distance is on the x-axis, contrary to Figure 3.9, a planet can retain its atmosphere to the right. Each panel of the figure indicates a different stellar age.

If we focus on the top left panel of Figure 3.10, we see the distances at a stellar age of 1000 Myr. The ARD of a CO_2-dominated atmosphere and outer HZ only cross for stars with a mass greater than 0.4 $M_{\odot}$. For N_2-dominated atmospheres, this only happens for stars with a mass greater than 0.6 $M_{\odot}$. Based on our knowledge of the inner solar system planets and volcanism, we expect that the atmospheres of young rocky planets in and near the HZ are CO_2-dominated. When we think back to the history of Earth's atmosphere that we discussed in Section 3.3, we can also see that these CO_2-dominated atmospheres can still evolve to N_2-dominated atmospheres if the surface conditions and tectonics allow for it. Because of this and the fact that CO_2-dominated atmospheres can keep the planet the coolest, we will focus on these atmospheres. In the first panel, we can see that the ARD of stars with a mass smaller than 0.35 $M_{\odot}$, does not follow the same trend as that of the higher mass stars. As discussed by Johnstone et al. (2021a), the difference in EUV luminosity is due to the much slower spin-down rate of fully convective stars. This results in an ARD at a larger orbital distance than the outer edge of the HZ.

In the second panel of Figure 3.10, we see the planetary systems at 2000 Myr. At this age, the entire HZ falls outside of the ARD for stars more massive than 0.6 $M_{\odot}$. Stars with masses between 0.6 $M_{\odot}$ and 0.3 $M_{\odot}$ have only a part of their HZ at a distance where the mass loss rate is small enough for the atmosphere to survive. Below this stellar mass range, the HZ is entirely closer than the ARD. A planet around such a low mass star would at this point have experienced 2 Gyr in an environment with a mass

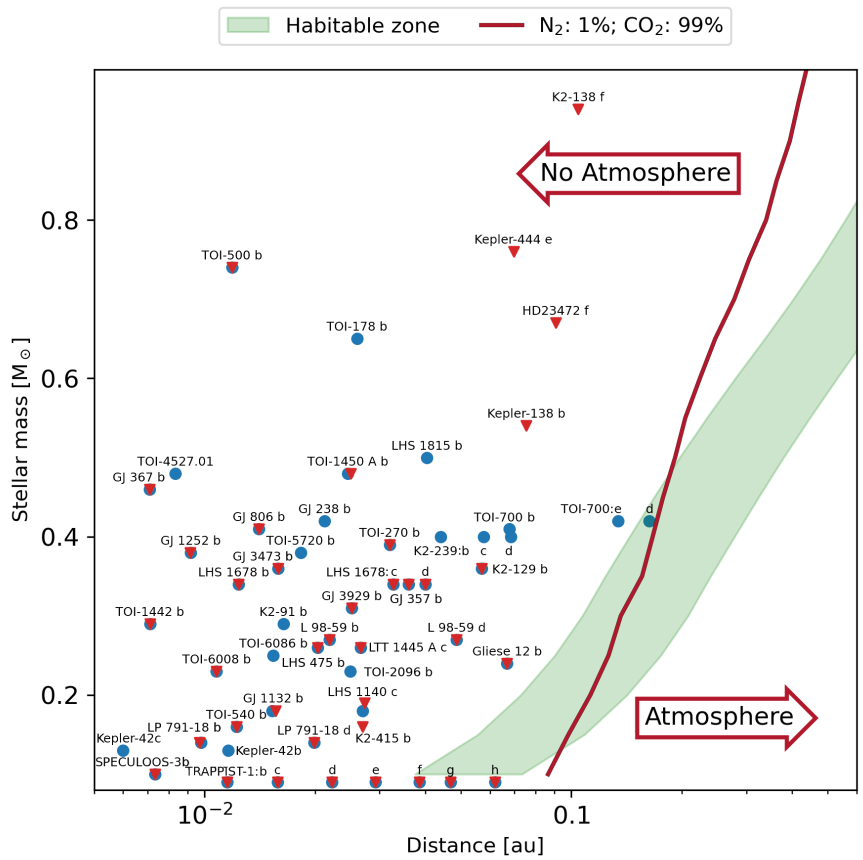

Figure 3.11: Atmosphere retention distances for different stellar masses for initially slowly rotating stars at an age of 5000 Myr. The green shaded area indicates the habitable zone. Blue circles indicate JWST observations, whilst the red triangles indicate the Ariel Candidate Sample. For clarity, some system names were not repeated, indicating the planet simply by its letter.

loss greater than the extreme mass loss rate we discussed in Section 3.2.4, making it very unlikely that these planets retain many volatiles in their atmospheres.

The remaining panels of Figure 3.10 show how the ARD moves inwards as the stellar rotation rate continues to spin down. Throughout these time steps, whilst the star remains on the main sequence, the HZ remains relatively stable. These panels can help limit the possible compositions of atmospheres. For example, we can take a closer look at the 4000 Myr panel, where on the one hand, around a 1 $M_\odot$ star, any composition would have negligible losses. On the other hand, around a star of 0.5 $M_\odot$ a nitrogen-dominated atmosphere such as Earth's, would be stable near the outer edge of the HZ, but not near the inner edge, although this does not necessarily imply the presence of significant amounts of nitrogen or liquid water. In Section 3.3, we saw that Venus falls both within the HZ and out of the N_2-dominated ARD, but its atmosphere contains neither significant amounts of N_2 or H_2O.

On top of constraining the possible parameter space searched in observational programmes and possibly providing priors to atmospheric retrievals, knowing the possible composition of atmospheres can give us insights into habitability, particularly when we look at more complex life. In their work, Catling et al. (2005) describe how a certain amount of free oxygen is likely required to provide sufficient energy for complex organic structures. The buildup of free atmospheric O_2 is linked to the capture of CO_2 back into the surface, which in turn is strongly linked to the oceans and tectonics on Earth (Alcott et al. 2024). Additionally, Stüeken et al. (2016) show that both high N_2 and O_2 levels together might be required for life. This makes the ARD of N_2-dominated atmospheres more important when considering the possibility of complex life.

Lastly, to illustrate the importance of the ARD, we can compare these results to scheduled observations from current and upcoming space missions. In an attempt to keep such a figure readable, we will focus on the CO_2-dominated atmospheres at an age of 5000 Myr. If a planet is left of ARD, the planet will have experienced 5 Gyr of very high mass loss, even if the atmosphere is composed of predominantly CO_2, making it unlikely they would retain their atmosphere. Another point we have to take into consideration is the mass of the planet. Rogers (2015) shows that the boundary between rocky planets and planets with extended gaseous envelopes lies at 1.6 $R_\oplus$ or about 4.1 $M_\oplus$ assuming an Earth-like density. As discussed in Section 3.2.3, the loss rates already change within the preliminary test range from 0.8 to 1.2 $M_\oplus$. To limit our conclusions to planets for which our models would be representative, we will only select planned observations of planets with masses below 2 $M_\oplus$. Figure 3.11 is a repetition of the panel at 5000 Myr of Figure 3.10, showing the distance against stellar mass with planets added. JWST observations are indicated with blue circles, whilst targets from the Ariel Mission Candidate Sample are indicated by red triangles. We can see that most planets in this sample orbit their host star much closer than the ARD. This is to be expected due to the observational bias towards short-period planets. Figure 3.11 indicates that it is unlikely that any of these planets would retain any atmosphere for an extended period of time unless it is rapidly replenished through continued and excessive outgassing. A detection of atmospheres around these objects would then indeed suggest strong outgassing activity as mentioned for 55 Cnc e in Section 1.5.

For stars at the low end of our mass range, the actual atmospheric loss rates are likely even greater than this figure indicates. Due to the relatively low luminosity of these stars, given their small surface area and effective temperature compared to, e.g., the Sun, their flares can reach luminosities similar to or greater than the bolometric luminosity of the star (e.g. Ealy et al. 2024). This sudden increase in flux, in particular in XUV, can change the chemical composition of the atmosphere, leading to an increased thermal loss rate (e.g. Segura et al. 2010; do Amaral et al. 2022). Though the short duration of flares leaves the long-term influence of large flares uncertain (e.g. Nicholls et al. 2023), it is important to keep in mind that factors not taken into account in this work might further influence these mass loss rates.

In Section 1.5, we saw that several planets have already been observed at the time of writing this thesis. Emission measurements of TRAPPIST-1 b (Greene et al. 2023) and TRAPPIST-1 c (Zieba et al. 2023), as well as transmission measurements of LHS 1140 c (Cadieux et al. 2024; Damiano et al. 2024), exclude the presence of thick atmospheres and are consistent with bare rocks. On Figure 3.11, all three of these planets fall clearly on the 'no atmosphere' side of the ARD. This seems to indicate that our models do not contradict observations.

The target closest to the ARD is TOI-700 d, a 1.72 $M_\oplus$ planet orbiting within the HZ of its host star (Suissa et al. 2020). On the one hand, as the mass of the planet is higher than our modelled mass, the actual ARD could be closer. On the other hand, because the star could be as young as 1.5 Gyr, the ARD could be much further out and closer to the ARD shown in the first panel on the right column of Figure 3.10. Additionally, a previous study on the target by Nishioka et al. (2023) found that the ion escape, a type of non-thermal loss, would erode a Venus-like atmosphere in the absence of a strong intrinsic magnetic field.

This figure seems to indicate that none of the roughly Earth-mass planets planned to be observed would be able to retain their atmosphere. Although only the observations will bring more certainty, models seem to indicate that these planets are unlikely to retain any atmosphere.

3.4.2 Stellar rotation

Another parameter to discuss is the initial rotation rate of the star. To this point, all models have assumed the stars to have slow initial rotation rates. Figure 3.12 shows the evolution of the ARD and the HZ over time. In this figure, we show the ARD for a planet of 1 $M_\oplus$ with an atmosphere composed of 99% CO_2 and 1% N_2. The different lines indicate the ARD for different initial rotation rates, with the slow rotator in red, the medium rotator in green, and the fast rotator in blue. Just as before, the HZ is shown by the green shaded area. The HZ remains the same for all initial rotation rates, as the bolometric luminosity is not affected in any significant way by the initial rotation rate. Each panel of the figure shows a different stellar mass, from a low mass M-type star to a Sun-like star. The various panels also demonstrate that the initial rotation rate is not equally important for each stellar mass.

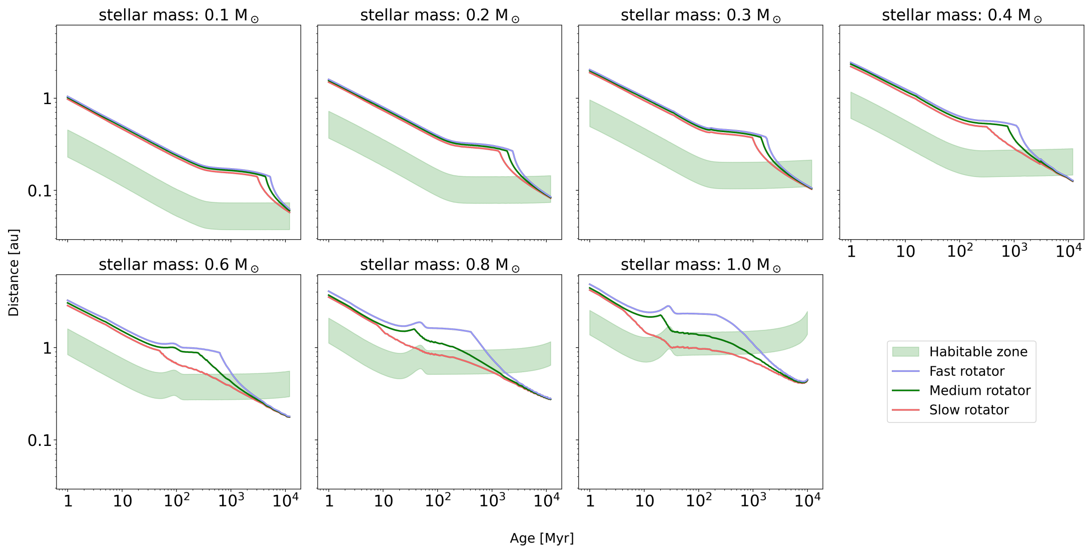

Figure 3.12: Atmosphere retention distances for slow rotators (red), medium rotators (green), and fast rotators (blue) for a 1 $M_\oplus$ planet with a 99% CO_2 atmosphere. Above these lines, atmospheres can be retained. The green shaded area indicates the habitable zone. Each panel indicates a different stellar mass.

Looking at the 1 $M_\odot$ case, we can see very different ARDs depending on the initial rotation rate. The red line for the slow rotator represents the same ARD as the 99% CO_2 case in Figure 3.9. The differences between the initial rotation rates were discussed in detail in Johnstone et al. (2021b), and using geological records of the Archean atmosphere, the authors concluded that the Sun must have formed as a slow to medium rotator. In the more generalised approach we have used here, we could conclude from this figure that only the outer half of the HZ of a fast-rotating Sun-like star would be hospitable for atmospheres between 1000 and 1500 Myr. For an intermediate rapidly rotating star, the entire inner edge of the HZ crosses the ARD at 1000 Myr. Therefore, if the Sun had started as an intermediate rotator, the Earth could still retain an atmosphere but would likely have followed an entirely different evolutionary path than the one indicated by geological records.

If we shift our focus to lower-mass stars, we can see that the division between different initial rotation rates occurs at increasingly later ages. In the panel for a 0.4 $M_\odot$ star, we can see that the ARD of the slowly rotating star overlaps with the outer edge of the HZ at 1000 Myr, meaning that a planet at this distance could hold onto an atmosphere. However, for a star of the same mass with a fast initial rotation rate, the ARD would only pass the outer edge of the HZ at 2000 Myr. A planet around such a star would experience a 1000 Myr of extreme mass loss, making it less likely to have retained an atmosphere.

For fully convective stars, i.e. those with masses below 0.35 $M_\odot$, this gap increases even further due to their slow spin-down rate. In the panel for a 0.1 $M_\odot$ star, the ARD crosses the outer edge of the HZ at 7000 Myr for an initially slowly rotating star and at 9000 Myr for an initially fast rotating star. Although in neither case the HZ planets of such a star are likely to have retained any atmosphere, this can become more important for planets on wider orbits.

We can look at the evolution of these low mass stars from a theoretical point beyond Figure 3.12. A 0.1 $M_\odot$ star takes about 1–2 Gyr to settle on the main sequence (Ramirez & Kaltenegger 2014). During this time, M dwarfs move vertically down the Hayashi track in the Hertzsprung-Russell diagram, and their initial bolometric and X-ray luminosities start out several orders of magnitude higher than after reaching the main sequence. We can see this reflected in Figure 3.12 in the initial slope before the different initial rotation rates diverge. Once on the main sequence, mid- to late-M dwarfs continue to be appreciably active. Their deep convection zones, combined with sufficiently fast rotation rates, lead to an efficient magnetic dynamo action (Johnstone et al. 2021a). The subsequent decline of its X-ray activity level due to spin-down is very slow and is only about one order of magnitude in several billion years, in contrast to a Sun-like main-sequence star that decays in X-rays by 2–3 orders of magnitude on the same timescale while on the main sequence (Johnstone et al. 2021a).

These results highlight that, even though the stellar mass has a greater impact on the ARD, the initial stellar rotation rate adds an additional layer of complexity to determining the likelihood of atmospheres' survival. This complexity is further increased by the fact that we can only observe the current rotation rate of a star, which does not necessarily allow us to determine the initial rotation rate and evolutionary path of the star. This is because all evolutionary tracks of rotation converge to nearly the same track at some evolutionary stage, making backwards tracing difficult (Tu et al. 2015). A way to overcome this constraint is to model, as we have done above, an atmosphere over time, including realistic outgassing rates and loss rates, for varying initial stellar rotation rates. The range of initial rotation rates leading to atmospheric properties observed today can then be used to model the planetary atmosphere in time, and equally all atmospheres in the same planetary system.

Chapter 4

Machine Learning Informed Initial Estimates

"There is a remarkably close parallel between the problems of the physicist and those of the cryptographer. The system on which a message is enciphered corresponds to the laws of the universe, the intercepted messages to the evidence available, the keys for a day or a message to important constants which have to be determined."

\- **Alan Turing**

Introduction

In Chapter 1, we saw how there is an ever-increasing number of planets being observed. Exoplanets also come in a much wider array of compositions and environments. This leaves us very uncertain when trying to model the conditions of the planet and draw conclusions about observations. To solve this issue, we can simply run a large number of possible solutions and see which ones work best for the observations. Running a large number of models tends to take a lot of time and computational resources.

In this chapter, we will take a look at a possible way to solve this issue. The model I will present here was made in collaboration with Axinya Tokareva and presented in her Master's thesis (Tokareva 2024), which I co-supervised. For transparency, I wish to clarify each of our contributions to this solution. My contribution to this solution includes coming up with the concept and general structure of the model (i.e. a cascade made up of a fully connected network and a convolutional neural network), as well as the creation of the training set and the connection back to the Kompot code. Tokareva (2024) implemented the solution (i.e. creating the networks in the cascade, refining their architecture, determining the hyperparameters of each network, adding features to optimise the results), tested the performance of the network, and created a framework for future expansion. These results will also be presented in an upcoming publication, which is currently in preparation.

4.1 Physical Models

In Chapter 2, we saw a description of the Kompot code, an example of a forward model. These models contain a lot of different physical effects which all influence each other. To capture this interplay of effects, many models take an iterative approach, updating values influencing one physical mechanism at a time until a steady state is reached. Of course, if more effects are taken into account, each interaction will take longer, and the number of iterations likely needs to increase as well. Retrievals (see Section 2.2) can require a million such models for a single observation. To make a model compatible with retrievals, and useful on any practical timescale, it requires a model to finish within a fraction of a second.

A first solution could be to simplify the model. If fewer calculations need to be done, the model will be faster and might require fewer iterations. An example could be to only consider equilibrium chemistry, which can be calculated nearly instantaneously, contrary to photochemistry. But as we saw in Section 1.5, photochemistry plays an important role in exoplanet atmospheres. Similarly, assuming a constant thermal profile would accelerate models greatly, but might result in unphysical combinations. So even though this is the most obvious solution, it might not be the ideal one.

A second solution would be to optimise the code itself, which can be done in several different ways. Depending on the coding language used, there are several optimisations that can influence the speed of a code, such as the compiler flags or even whether arrays are looped over row first or column first. This type of code optimisation is often very labour-intensive, very language-dependent, and, unfortunately, can only get you so far. A different approach to accelerate code is to parallelise certain calculations. For example, when calculating the chemistry throughout the atmosphere, the chemical composition at each altitude can be calculated at the same time, as these are not influenced by each other (assuming other physics, like diffusion, are handled in other steps of an iteration). Similarly, the radiative transfer of each wavelength bin can be calculated in parallel. Parallelisation of this kind can significantly accelerate a model, but it requires enough cores to divide the calculations between them, and it is still limited by the time required for a single calculation. In our model, for example, the calculation of chemistry takes the most time out of all steps, as it needs to solve a matrix which scales up by the number of included reactions (see Section 2.4.2), which cannot be solved in parallel as the different reactions can involve the same species. A third solution to run a model faster is to run the code on a Graphics Processing Unit (GPU). GPUs are, by design, exceptionally suited for parallel processing and matrix operations. Rewriting a code to run on a GPU can accelerate a model greatly (e.g. Vorobyov et al. 2023). Some downsides of using GPUs are that it requires additional hardware, namely the GPU, and specialised compilers, such as Nvidia's CUDA or AMD's ROCm. Additionally, rewriting code to run on GPU devices can require a significant amount of work to run efficiently, as moving data between the CPU and GPU unnecessarily can actually slow the code down.

Beyond these optimisations, we can look towards machine learning solutions to accelerate the model. In order to find the appropriate solution, we will take a step back to take a look at the type of problem we wish to solve. In Section 2.4, we saw that the model is made up of many different physical effects, including chemistry, heating, cooling, and diffusion. Most of these effects are calculated through systems of differential equations and, in essence, form a boundary condition problem. These boundaries are the incoming stellar radiation, the base temperature and density, and chemical composition at the lower boundary. Unfortunately, the large number of equations combined with the fact that several mechanisms (such as energy exchange) are approximated through analytical equations that do include asymptotic behaviours outside of their modelled parameter range, make it impossible to determine if solutions or unique solutions exist for a set of boundary conditions. However, the model we use in this work does not contain any stochastic processes, which makes a unique solution, and predicting said solution, possible. Additionally, we know that due to thermal conduction and diffusion, both the thermal profile and chemical profiles are continuous. These points will help us decide on the type and structure of a machine learning solution.

4.2 Existing Machine Learning Models

Within astrophysics and planetary science, there have already been several different machine learning approaches to speed up models. In this section, we will take a brief look at some examples, some of their advantages, disadvantages, and architectures.

A great advantage of machine learning solutions, and particularly neural networks, is their ability to produce near-instantaneous results. This comes at the cost of requiring a large amount of data, and most computational time is spent in training the network. Some examples of speeding up retrievals using neural networks include the FlopPITy code by Ardévol Martínez et al. (2024), the FASTER code by Lueber et al. (2025), or the models proposed in the Ariel Data Challenge (Yip et al. 2023). The former of these two uses sequential neural posterior estimation to retrieve the posterior distributions of the exoplanet parameters from a spectrum. An advantage is that this method retains a similar method to classical retrievals. The authors show that their approach results in a speed up of the retrieval between 2 and 10 times, but mention that the speed up is more efficient for a single observation rather than population studies. The method presented by Lueber et al. (2025) is more suited to analyse larger sets of observations. In that work, the posterior distributions are estimated directly through the use of a neural network and simulation-based inference. The main advantage is that the method allows for near-instantaneous results. On the other hand, the training of the network requires large amounts of synthetic models to train on and is rather model-dependent. Both of these machine learning solutions show incredible speed-ups in their respective codes. Unfortunately, both rely on relatively large data sets often made up of relatively simple forward models (e.g. isothermal profiles, limited number of chemical species).

A different approach would be to use a machine learning solution as a substitute for processes that prove to be bottlenecks in forward models. An example of such an approach is presented in Tahseen et al. (2024), where the radiative transfer in a GCM is replaced by a surrogate model. This surrogate model is made up of a recurrent neural network, a structure particularly suited for sequential data, in this case, how the spectrum changes throughout the atmosphere. These networks were trained on models produced by the code in which the surrogate needs to fit in. The authors use a surrogate model for long and short wavelength radiation, as these behave differently in atmospheres. This demonstrates how neural networks are more suited for specialised tasks than as a one-size-fits-all solution. The authors achieve an impressive speed-up of around 150 times. A limitation of this approach, just as before, is that the model is reliant on prior examples and works only within the parameter domain on which they were trained.

Another code focused on the influence of stellar radiation on planetary atmospheres is CHEXANET (Vojtekova et al. 2025). This paper describes a U-Net architecture with attention to estimate the steady-state chemical profile of an atmosphere from its equilibrium chemistry solution. This type of convolutional neural network is used predominantly in image segmentation and generation. In this case, the network takes a two-dimensional array, namely the vertical mixing ratio for a set of species in chemical equilibrium, and reduces the size of the array, extracting the most relevant information. This reduced array is then uncompressed back into a two-dimensional array representing the vertical mixing ratios of the species with disequilibrium chemistry. Using such a network allows the comparably slow calculation of disequilibrium chemistry to be estimated in just a second. The authors point out that the model is limited to the parameter range on which the model was trained. This can be expanded through so-called transfer learning, but requires additional models as examples.

Gebhard et al. (2024) propose a parameterisation of pressure-temperature profiles using neural networks. The concept in that work is that there is a function which can turn an array of pressures into a temperature profile. A parametric family of such functions then allows the authors to reproduce the modelled pressure-temperature profiles. As a training set, nearly 150000 profiles from two different codes were used to capture the large variety of possible shapes. The first step in training this model was to use an encoder structure to reduce the model profiles to a set of latent variables, which can be interpreted as the most determinant information of that profile. These variables are then used with an array of pressure points to train a network with a decoder structure to reconstruct the temperature at each of these points. In the introduction of Gebhard et al. (2024), the authors clarify some requirements that the parameterisation must satisfy for this approach to work. These requirements include that, ideally, the latent variables represent some physical variable, that the number of these latent variables is as small as possible (reducing the parameters that need to be retrieved), and that the mapping between the latent variables and the output profiles is smooth, such that small changes in the latent variable result in small changes in the profiles. We can imagine that this might be the case for atmospheric profiles where, for example, a slight change in the CO_2 content of an atmosphere can result in a change of the thermal profile (see Section 3.2.1). The main advantage of this approach is that more realistic and complex thermal profiles can be captured in just a few latent variables. This would limit the number of parameters a retrieval will need to estimate, making the retrieval process faster.

Throughout these examples, we can identify two points that recur in many of these models. First, training neural networks requires a lot of example data. This data usually comes in the form of thousands of models calculated using more traditional approaches. Training sets, therefore, tend to be very computationally expensive to build and inherit the biases and shortcomings of the models they were trained on. Any improvements to the model used to create the training set lead to, in the best case, a retraining of the network or, in the worst case, a redesign of the entire network. All this adds to the computational resources spent on finding faster solutions. A second point is that in most of the examples we have seen here, machine learning solutions provide a final solution in order to replace the classical calculation altogether. Though this certainly gives the fastest results, it requires us to have faith that these very complicated networks focus on the tasks we expect them to focus on. At times, neural networks will train on patterns in noise or pick up on features which might not be ideal for their purpose. This was demonstrated by Goodfellow et al. (2014) where the authors showed that adding near-invisible noise to an image convinced an image classification network that a panda became a gibbon. An example of possible unexpected patterns influencing networks is mentioned in the addendum to Wu & Zhang (2017), where photographs of different categories were taken in very different circumstances unrelated to the features they were trying to extract. This shows that neural networks can produce unexpected behaviours, especially when applied beyond the original training data. With these two points in mind, let us try to find a solution that will speed up our models whilst retaining as much flexibility and confidence in the model as possible.

4.3 Machine Learning Informed Initial Estimates

In Section 4.1, we saw that essentially, we want to solve a boundary condition problem. In a normal run with the Kompot code, an isothermal and homogeneous atmosphere is assumed as an initial solution, which is then adapted iteratively as described in Section 2.4 until a steady state is achieved. Reaching the steady state can easily require a million iterations and in highly irradiated cases where the isothermal initial estimate is very far from the true thermal profile, some of the solvers end up overcompensating, resulting in a failed simulation. A way to speed up the calculation of a model is to start from a solution closer to the final solution so that fewer iterations are required to reach the final state. By using a machine learning model to make an initial estimate, we can cut out a significant amount of early iterations. This result is then used in the full forward model to polish the results into the final atmospheric model. This approach harnesses in part the speed of machine learning solutions, whilst ensuring that the model is physically correct through the 'corrections' by the forward model.

4.3.1 Training data

Before we discuss the model, we should take a closer look at the available data to train on. In Chapter 3, we presented a grid of models that cover several planet sizes, atmospheric compositions, and instellation. Though these models do not represent an exhaustive list of possible atmospheres, they provide a range of possible atmospheres based on parameters which we know influence the thermal and chemical structure. In total, this set contains 194 models, of which 136 could be used as a training set for the neural network. The discarded models were those reaching the critical temperature where some of the analytical approximations are no longer valid. Using these models would give the critical temperature an unrealistic weight, as realistically, such an atmosphere would reach higher temperatures. This is by all means a very small training data set. In Section 4.2 we saw that most machine learning approaches use tens, if not hundreds of thousands of models in a training set. Unfortunately, each of our models represents around 6-8 hours of computational time, with the highly irradiated cases relying on the end results of the less irradiated cases. This makes it impossible to build up a large enough data set to train a model to make accurate and generalisable predictions. However, this is not as much of a problem as we might initially think, since the end goal is not to have a perfect prediction of the atmosphere, but rather an estimate that is as close as possible to reduce the number of iterations required to reach the final solution. As such, an imperfect result is acceptable and we can train our network on this small dataset as long as we keep in mind the danger of overfitting. This approach also has the advantage that the results the network produces can be used to make more models, which can be used to retrain the model with an expanded training set. This will have a snowball effect where more models result in better initial estimates, which will in turn allow new models to be calculated even faster.

The models cover several parameters, though not all of these parameters are independent. For example, the composition of the atmosphere only includes different abundances of N_2 and CO_2, which means that we can express the N_2 mixing ratio as one minus the CO_2 mixing ratio. Ideally, the dataset would contain other species as well, breaking the correlation between these two parameters. Another example of artificially correlated parameters in the data set is the mass and radius of the planet, since the radius was calculated to retain a density of 5.5 g/cm^3. Though this is a reasonable assumption for roughly Earth-sized rocky planets, it does not hold for planets of sizes closer to the radius valley. All of the models in the training set also use the Sun's spectrum, which we saw in Section 3.2, will not always result in the correct thermal profile if we use a different spectrum. Though these correlations will not prevent the model from working, they are important to note and keep in mind. The full range of parameters in the training set is summarised in Table 4.1.

Table 4.1: Parameters covered by the training data set.

Parameter	Covered values	Unit
Planet mass	0.8, 1.0, 1.2	$M_\oplus$
Atmospheric composition	10/90, 20/80, 40/60, 60/40, 80/20, 90/10, 99/1	% CO_2/% N_2
Irradiance	1 - 14	$F_{EUV,\oplus}$

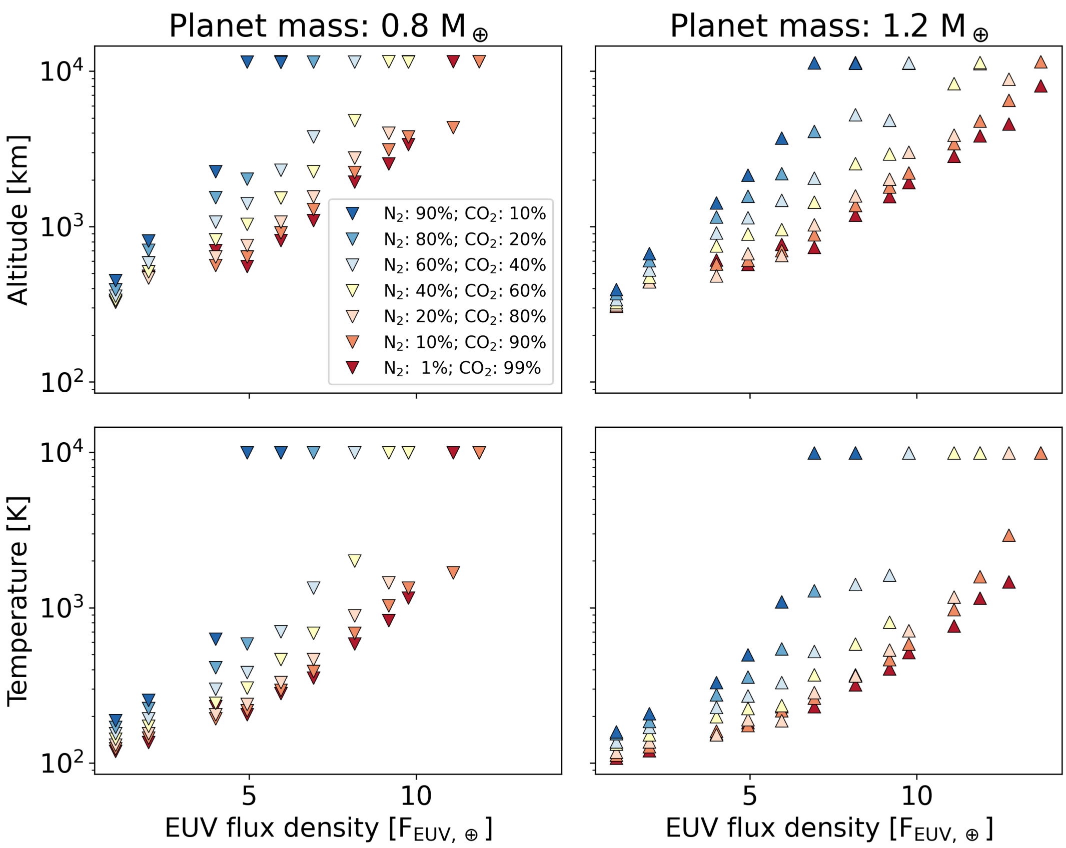

Figure 4.1: Exobase parameters at different flux densities. Top row: exobase altitude. Bottom row: exobase temperature. Left column: downwards triangles indicate a planet mass of 0.8 $M_{\oplus}$. Right column: upwards triangles indicate a planet mass of 1.2 $M_{\oplus}$. Colours indicate different chemical compositions of the atmosphere.

4.3.2 Model structure

To determine the most appropriate machine learning solution for our model, we will look at the section of the code that we would like to replace. One of the main strengths of the Kompot code, and reasons that a model requires so much time, is the self-consistent thermal profile. Estimating the entire thermal profile can be rather complicated, as many of the models have a varying number of cells, since the exobase altitude can change dynamically. So, rather than using a single complicated neural network, we propose to use a cascade of two light-weight networks, each specialised in particular tasks. The first network focuses on the conditions at the edges of the simulated domain. The output of this model is then passed to the second network, which fills in the profile between the end points.

By design, the lower boundary has a fixed temperature that is given as an input parameter. At the other end of the thermal profile, there is the exobase temperature. From the Solar System examples we saw in Section 2.5, we know that there are several parameters that can influence the exobase temperature. This includes the amount of received flux, the chemical composition of the atmosphere (in particular, the amount of CO_2), and the lower boundary conditions. Similarly, we can determine the altitude of the exobase, which also depends on the mass and radius of the planet. In Figure 4.1 we show how the exobase parameters of the models presented in Chapter 3 change as a function of some of these parameters. We briefly note here that different compositions all evolve towards a maximum temperature around 10000 K and altitude of 50000 km, at which point some analytical approximations are no longer valid (see also Section 3.2.3). Since these unphysical models would overrepresent this area of the parameter space, they were excluded from the training set, but are shown here to demonstrate the trends in the data. This figure illustrates that the exobase parameters form a smooth and continuous function with these input parameters. However, the number of dimensions of this hyperplane and the possible covariance of parameters make determining an analytical equation of this non-linear plane complicated. This is where a neural network can act as an approximation of this function. Since, in the usual context of machine learning problems, the function we aim to solve is relatively simple, we can use a simple feed-forward neural network. As mentioned in the previous section, there are many correlated variables due to the limited size of the training set. As such, the network takes in the three parameters listed in Table 4.1, which are also used in a normal Kompot model, and returns the exobase altitude and temperature.

An important reason to estimate the exobase altitude is that this altitude can vary strongly depending on the other parameters, as shown in the top row of Figure 4.1. This means that different models have different numbers of layers, which can be complicated for neural networks. To solve this, some normalisation of the training data is required. This can be done by rescaling each atmosphere between 0 and 1 by subtracting the lower boundary altitude and dividing by the exobase altitude. Neural networks can then be trained to produce these normalised thermal profiles with a set number of points. Using the predicted exobase altitude, the estimated normalised profile can then be turned into a full profile again.

With the lower and upper boundary temperatures and altitudes known, the next step is to connect the two temperatures. Throughout Chapters 2 and 3, we saw many examples of thermal profiles. These profiles all have an overall similar shape, often cooling down with increasing altitude from the lower boundary and then rapidly increasing towards the exobase. These shapes can be decomposed into several decreases in temperature, constant temperature, or increases in temperature with increasing altitude. From a physical perspective, we know that the thermal profile of the atmosphere must be a continuous curve, as each layer of the atmosphere influences the temperature of adjacent layers. A type of neural network particularly suited for continuous data made up of several shapes is called a convolutional neural network. This type of network optimises kernels rather than weights like a fully connected neural network. This has the advantage that the network usually needs fewer parameters and can retain the fact that neighbouring points influence each other, such as in time series predictions or image recognition. This convolutional neural network will take the same input parameters as the previous network and the predicted exobase values to produce an array of temperature values. This estimated thermal profile can then be used as a starting point for a full Kompot model instead of the isothermal estimate.

4.3.3 Results

Since the implementation of the neural networks was performed by Tokareva (2024), I refer the reader to that thesis or the upcoming paper Tokareva et al. (in prep) for a more in-depth discussion. Here we will briefly summarise the performance of the network.

Figure 4.2 shows the comparison of a thermal profile predicted by the cascading model compared to the actual profile. This model represents a planet with a mass of 1.0 $M_\oplus$ and an atmospheric composition of 40 % CO_2 and 60 % N_2. The planet in this scenario receives 8 $F_{\mathrm{EUV},\oplus}$. This model was part of the training set and is estimated very well by the machine learning model. This type of highly irradiated model requires around 12 hours of computation time (after code optimisation presented in Tokareva 2024), because the final profile is too far from an isothermal profile and requires several intermediate models. If we start a model from this thermal profile, the model requires closer to 6 hours of computation time, since no intermediate models are needed. On the other hand, a low irradiance model (like Earth) achieves similar accuracy, but only speeds up a model from 4.2 hours to 3.5 hours. Though this speed-up might not seem like a lot, it is important to notice that we have only replaced the thermal profile but still start the simulation with a homogeneous chemical composition. If the chemical composition is estimated as well, this initial estimate will again be closer, requiring fewer iterations to reach a final solution. This could be achieved through a first estimate with equilibrium chemistry calculations or another network similar to the approach presented by Vojtekova et al. (2025).

In general, the networks achieve predicted exobase values that are within 10% of the model values on the test set. These results are very good given that the training set only contains 136 models. The

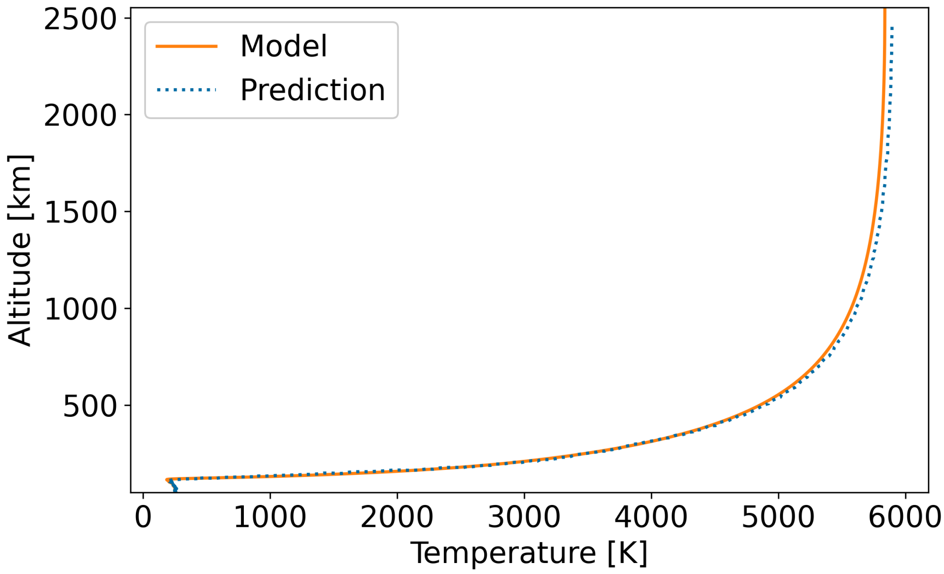

Figure 4.2: Comparison of the predicted altitude-temperature profile with the profile of the full model of an Earth-mass planet at 8 $F_{EUV,\oplus}$ with a composition of 40 % CO_2/60 % N_2.

test set falls within the parameter space shown in Figure 4.1. Since these models were not part of the training set, this demonstrates that the network did not overfit and learn the training examples 'by heart'. A goal of our approach is to be able to make some initial estimates for models outside of the parameter space to rapidly expand the training set.

Figure 4.3 shows the estimated profile for a planet with a 0.8 $M_\oplus$ mass, a CO_2 mixing ratio of 0.965, and 2 $F_{EUV,\oplus}$. This represents parameters similar to those of Venus so that we can compare to the model presented in Section 2.5. The Venus model still falls within the range of parameters the network was trained on. Contrary to the training set, however, the lower boundary temperature of the Venus model is much lower than the temperature fixed in the model at 273 K. In spite of this, the estimation follows the shape of the thermal profile reasonably well. The modelled atmosphere of Venus contains many more chemical species (see Table 2.2) than those included in the training set, which can explain part of the difference as well. Moving a bit further outside of the range of parameters covered by the training set, we can try to estimate the thermal profile of Earth. Though the mass and irradiance are within the trained parameter set, the atmospheric composition lies well outside of it. Earth has a CO_2 mixing ratio of 4.0×10^{-4}, which is an extrapolation of the parameters the network knows. On the other hand, the model has mixing ratios of 6.0×10^{-6} H_2 and 0.20955 O_2, which affect the thermal structure through infrared heating and cooling, respectively. Figure 4.4 shows how the neural network estimates the Earth's thermal profile compared to the full model, which was presented in Section 2.5. We can see that the estimator strongly underestimates the exobase temperature and altitude, whilst overestimating the cooling near the bottom of the simulated domain. Normally, such a result would be completely unusable, but since our current goal is to get closer to the final thermal profiles than isothermal, this estimate can still be used. The calculation of the Earth model starting from a homogeneous and isothermal profile requires a bit over 2 hours to reach a steady state. Keeping all parameters the same, the model starting from the homogeneous profile with the estimated thermal profile requires 1.6 hours to reach the same steady state solution. Though this is only a marginal reduction in computation time, this model demonstrates that it is possible to push models towards other parameters, in this case, the mixing ratios of O_2 and H_2O.

Generally, the approach results in a speed up by a factor of 1.2 to 2, despite the very small training set used. Though this difference might not seem like a lot, since models still require hours to finish, we only provided an estimate of the thermal profiles. If a similar estimate is made of the chemical profile, the starting point will be even closer to the final result.

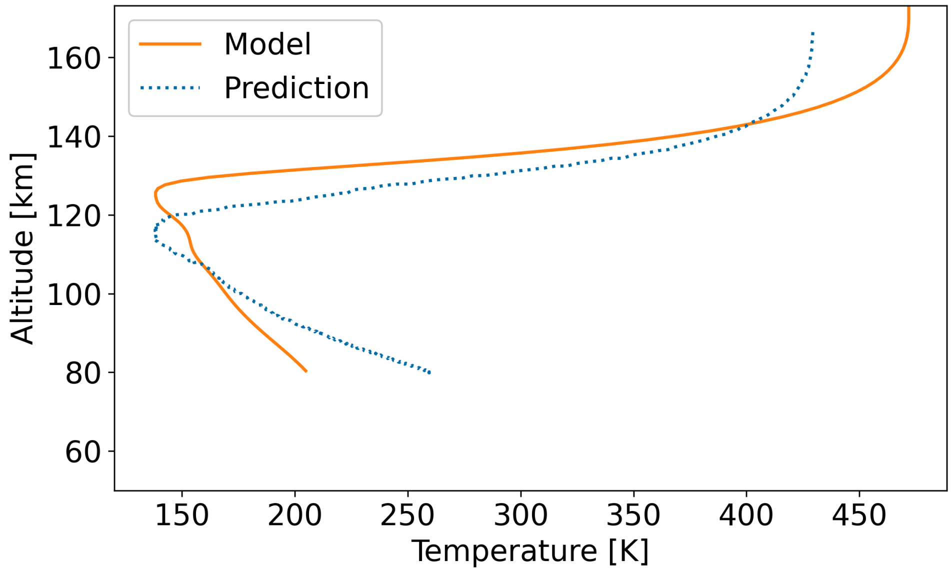

Figure 4.3: Comparison of the predicted altitude-temperature profile with the profile of Venus.

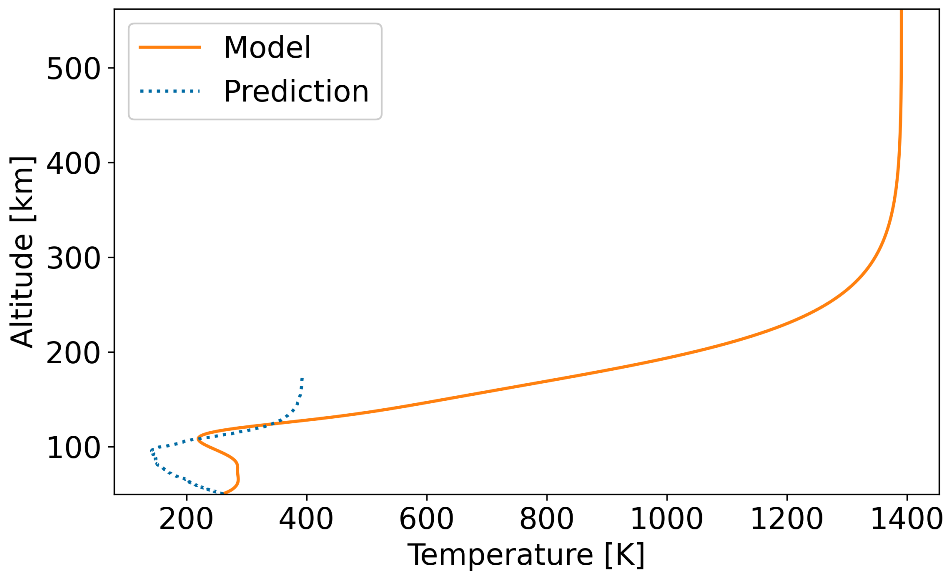

Figure 4.4: Comparison of the predicted altitude-temperature profile with the profile of Earth.

4.3.4 Limitations

The machine learning solution discussed here was mostly written as a proof of concept within the context of a Master's thesis (Tokareva 2024), which means that it has certain limitations. Most of these limitations stem from the very limited dataset which was available to train the model on. This caused several parameters, which we know have an impact on the thermal profile from a physical perspective, to not be included as input for the network due to their correlation with other variables. This includes, for example, the mixing ratios of species other than CO_2. Making sure that the architecture of a neural network is future-proof for the addition of chemical species at a later point is exceedingly complicated. A possible way to circumvent this would be to use the relative abundances of elements rather than those of molecular species, similar to the approach of many equilibrium chemistry codes (e.g. Woitke et al. 2018; Stock et al. 2018). With the addition of a fully connected layer, the neural network could learn the importance of relative elemental abundances to combine them into molecular abundances.

In the previous section, we saw in the Venus model that the lower boundary conditions did not match up. In Section 3.1.1, we discussed how the lower boundary temperature influences the layers in the lower section of the modelled domain, but except for an offset of the thermal inversion, has little impact on the upper half of the model. Within this work, focused on atmospheric losses, the choice of the lower boundary temperature is of little consequence. However, if we wish to future-proof the structure of the neural network, we should use the lower boundary temperature as an additional parameter. This becomes increasingly important once we start looking at lower altitudes for radiative transfer or to make the connection with the lower atmosphere.

Another limitation of the limited size of the dataset is the stellar spectrum. In Section 3.1.2, we saw that the exact shape of the incoming spectrum can have quite an impact on the thermal profile of the atmosphere. Since all models in the training set used the solar spectrum, the entire influence of the star could be captured in a single value, namely the irradiance, since the entire spectrum is scaled in the same way. Ideally, the network could make more accurate predictions for different spectral types. This could be captured by using the irradiance of several spectral bins rather than a single value. Of course, if more bins are used, a more accurate result will be possible, however, this means there are more parameters the network has to learn. For an initial estimate, around 10 bins can be enough to distinguish different stellar types and activity levels. To properly capture the interplay of spectrum and atmospheric compositions, quite an extension of the training set is required, which could probably be a thesis in itself. Lastly, a factor which likely has quite an important impact on warm-Neptunes and hot-Jupiters is the density of the planet. Though this falls outside of the scope of this work, it is interesting to keep in mind that not only the mass, but also the radius, is important for the determination of the scale height.

Chapter 5

Conclusion and future work

"Now you can rest.
Humanity could burn a million million books and inevitably would use that to tell a trillion stories more,"

\- **Timothy Hickson**, "The Funeralists; or Hate in Five Parts"

Summary

New observatories, both on the ground and in space, keep opening new avenues of study and discovery. A Dutch proverb tells us that "a warned person counts as two" or its English equivalent, "forewarned is forearmed." Knowing what observations to expect and where to look for these observations is invaluable when observational time is limited. This is particularly true for rocky exoplanets and the study of their atmospheres. Using models based on physics and chemistry can help us understand and predict different planets and their environments. This understanding can help inform observational strategies in exoplanet observations and the search for worlds like Earth. Unfortunately, model atmospheres tend to be complicated and computationally intensive, requiring either hours per simulation or simplifications or parameterisations.

A point of particular interest in the observations of exoplanets in the age of JWST is the detection of atmospheres around rocky exoplanets. A divide between Solar System bodies with and without atmospheres, named the cosmic shoreline (Zahnle & Catling 2017), was proposed to also apply to exoplanet systems. This divide relates the instellation to the gravitational acceleration to balance the thermal velocity of particles against the gravity of the planet. So far, observations of exoplanets have not been able to determine this relation outside of the Solar System.

In this work, we showed that the relation between planetary atmospheres and their host stars is more complicated. To prove this, we made use of the Kompot code (Johnstone et al. 2018), a code that self-consistently models upper atmospheres, to model atmospheric losses of different planets. This allowed us to estimate which planets are likely to hold onto an atmosphere for extended periods of time. We achieved this through the calculation of Jeans escape, a type of thermal escape, based on the parameters at the exobase that the code provides. These atmospheric models were then combined with stellar evolution models to determine the distance at which an atmosphere would be lost.

A second aspect we explored in this thesis was the use of machine learning solutions to speed up the calculation of these forward models. We presented an approach which combines the speed of neural networks with the physical accuracy of an atmospheric code by using the result of the network as an initial estimate for the full model.

5.1 Atmospheric retention distance

In Chapter 3, we presented a grid of model atmospheres. This grid covered planets with masses from 0.8 $M_\oplus$ to 1.2 $M_\oplus$ and atmospheric compositions varying from 10% CO_2 and 90% N_2 to 99% CO_2 and 1% N_2. This range covers Earth-like planets and the most common atmospheric compositions of rocky exoplanets. All of these planets have also been modelled with irradiances ranging from 1 to 14 times Earth's irradiance. This grid of models allowed us to get some insights into the thermal mass loss rates and their dependence on various parameters.

First and unsurprisingly, we saw that planets with a higher mass retain their atmosphere better, since the additional mass results in a stronger gravity. Though the grid only covered a small range of planetary masses, this effect was already prominently visible. Next, we saw that planets with a higher CO_2 mixing ratio manage to remain cooler and lose less mass due to the strong cooling line of CO_2 at 15μm. As CO_2 is one of the main components of volcanic outgassing, this is a good sign for the longevity of an atmosphere. In Section 3.2.4, we discussed other studies focused on the geological aspect of rocky planets, both inside the Solar System and outside of it. These studies tell us that planets can continue to outgas material over several gigayears at a rate of about 1.4×10^4 kg/s. With this, we defined a catastrophic mass loss rate of 1.6×10^4 kg/s (or Earth's atmosphere within 10 Myr), where the thermal mass loss rate is higher than the outgassing rate. It is important to note that in these models, we only calculate the Jeans escape of an atmosphere, and thus, they represent a lower limit of the total mass loss a planet would experience.

Reversing the grid, we used the irradiance at which the catastrophic loss occurs for each planet to determine the closest distance to a star where a planet could retain its atmosphere. To validate this Atmospheric Retention Distance (ARD), we applied it to the Solar System by using the EUV luminosity (10-92 nm) from stellar evolution models (Johnstone et al. 2021a). This showed us that at the time of the Moon-forming impact (30-100 Myr), when the secondary atmosphere likely first formed, the Earth was at the position of the ARD for a 99% CO_2 atmosphere. By the early Archean (600-1600 Myr), the oldest geological records indicate that the Earth had a surface pressure around 1-2 bar, of which CO_2 is estimated to contribute at most 0.7 bar. At this point in time, Earth's orbit crossed the ARD for a 40% CO_2 atmosphere according to our model, making it consistent with the few observational data we currently have to compare it to. The earliest geological record of Venus indicates the planet underwent extended resurfacing around 3600-4400 Myr. At this time, the orbit of Venus is further out than the ARD of all modelled compositions. Our model indicates that Venus' orbit only crossed the 99% CO_2 ARD at about 1000 Myr, but since it still has an atmosphere today, we can assume that atmospheres can still form at this point or have a large enough reservoir to mitigate early losses.

Next, we calculated the Habitable Zone (HZ) and ARDs for stars of different stellar masses at various ages. These models showed that at an age of 1000 Myr, the HZ is closer in than the ARD of any composition for stars with masses below 0.4 $M_\odot$. On the other end of the mass range, the HZ is entirely further out than the ARD for stars with masses above 0.8 $M_\odot$. Stars with masses less than 0.35 $M_\odot$ are fully convective and have a much slower spindown rate, causing them to maintain a higher EUV luminosity over a longer period of time. As the stars evolve on the main sequence, the HZ remains relatively constant. The ARD evolves with the stellar EUV luminosity and thus moves inwards as the star spins down. At an age of 5000 Myr, the HZ of stars with masses below 0.15 $M_\odot$ still falls entirely closer than the ARD of any composition. Using these models, we showed that none of the Earth-sized planets scheduled for observation with JWST or in the Ariel Mission Candidate Sample have an orbital distance where they could retain their atmospheres under the model conditions we used here.

Lastly, we looked at the impact of the initial rotation rate of the star on the ARD. Stars with a greater initial rotation rate require longer to spin down, leading their ARDs to remain further out for longer for all stellar masses. These higher rotation rates further reduce the probability that a planet can hold on to its atmosphere. Different rotational tracks merged again at later ages, making it impossible to assess the early environment of the stellar system, adding another layer of complexity.

5.2 AI informed initial estimates

In Chapter 4 of this thesis, we also looked at methods to accelerate the calculation of atmospheric models. In essence, we can describe our atmospheric models as complicated, non-linear boundary problems. These kinds of problems are solved iteratively, starting from some initial estimate, which in our case is an isothermal atmosphere or a Parker-wind solution. Many studies have tried to reach a final solution using machine learning methods, often achieving near-instantaneous results at the cost of physical accuracy and explainability. We proposed a combination of a cascading set of neural networks to approximate the thermal structure of an atmosphere and use it as an initial estimate for our full forward model. This approach allows us to reduce the number of required iterations to reach a steady state solution by taking advantage of the speed of machine learning solutions, whilst retaining the physical accuracy of a forward model.

The first part of the solution proposed in this work consists of a neural network which estimates the exobase altitude and temperature. The exobase parameters can be estimated using a small set of physical parameters normally used as input for the full model. These estimated parameters, together with the input parameters, are then passed to a convolutional neural network to predict the thermal profile of the atmosphere. This profile is then used as a starting point for our forward model. This results in a speed up by a factor of 1.2 to 2 and an increase of stability for models with a high irradiance. By using a cascading approach, we were able to use small networks with architectures more suitable for the specific task they needed to solve, rather than using a single large network to solve the entire problem at once.

There are several important advantages to our proposed solution. Since the output of the neural network is only used as a starting point for the forward model, the results of the network do not need to be perfect. This allowed us to train our network on a very small training set. The initial estimate of the model, even if imperfect, can then be used to create more full forward models in a shortened amount of time, which can in turn be used to update the model to make better predictions. This allows for a snowball effect where the expanding training set results in increasingly better estimates to further expand the training set. In Section 4.3.3, we demonstrated that the initial estimates can even be applied to atmospheric compositions that fall outside of the parameter range of the training set. Though the initial estimate was far off from the final thermal profile, it still resulted in a speed-up of the calculation of the model. This shows that the snowball effect also applies to parameters not previously considered.

5.3 Outlook and future works

5.3.1 Atmospheric models

In this work, we demonstrated that the complexity of atmospheric retention goes well beyond that implied by the cosmic shoreline through the use of the ARD. We primarily focused on Earth-sized planets and found that, in part due to observational bias and limitation, all roughly Earth-sized planets scheduled for observations are unlikely to have retained any atmosphere. However, a large portion of scheduled planets have masses greater than 2 $M_{\oplus}$. As we saw in Section 3.2.3, more massive planets can retain their atmospheres more effectively, making these super-Earths the most logical first extension of the ARD calculations. The study of more massive rocky planets also poses the interesting question of whether there is an optimal mass for a planet where its gravity is high enough to prevent thermal escape, whilst being low enough to allow for outgassing.

A second parameter to extend our study along would be the inclusion of more varied atmospheric compositions. In the current work, we focused on varying CO_2 and N_2 compositions as they form the most common atmospheric constituents for the Solar System rocky bodies. However, H_2O is also associated with volcanic outgassing and possibly forms in large amounts in the early stages of planet formation. Though on Earth, atmospheric water is mostly contained within the lower atmosphere, it is a strong greenhouse gas and a light-weight molecule, meaning it can influence the thermal profile of atmospheres and drag along heavier particles when it is being lost. The possibility of steam atmospheres in the early stages of a planet has also been suggested. Beyond H_2O, CH_4 is also an interesting candidate to extend the parameter space into. This molecule shares many properties with water and is also present in large amounts in the atmosphere of Titan. If planets with such atmospheres are able to retain their atmosphere over longer periods of time, they could provide an interesting, more exotic environment for possible life to form.

Taking a step back from the results of the models, another area of future work would be further development of our code. As is commonly said, "all models are wrong, but some are useful". The detection of photochemical products in exoplanet atmospheres has demonstrated that increasingly complex models are required to accurately reproduce observational data. In order to make sure that models remain useful and become slightly less wrong, more physical processes need to be included. In the case of this work, an example of such an addition would be a more complete treatment of radiative cooling mechanisms. As discussed in Nakayama et al. (2022), conditions which are not present within our Solar System could lead to certain cooling pathways to become more dominant than the observed mechanisms included in the Kompot code. Though we do not believe that the results will drastically change the results we presented here, it might move certain ARDs closer to the host star. An additional benefit of calculating the radiative cooling profile of an atmosphere is that it can provide a section of the emission spectrum of the planet. Another process currently missing from our model is the formation of clouds and hazes. Observations of larger exoplanets have already demonstrated that clouds can cause dampening of spectral features, evening-morning terminator asymmetries, and possibly temporal variations in the spectrum. The inclusion of cloud formation and precipitation can also give us insights into the evolution of atmospheres and their chemical composition.

5.3.2 Machine learning solution

Unfortunately, the addition of more processes in the calculation of the models will inevitably make them slower. Our proposed solution to use cascading neural networks to provide an estimated solution as a starting point already makes a first step in that direction. The most obvious future work in this aspect is expanding the training set beyond the meagre 136 models of the original training set. An extended training set would particularly improve the estimates of parameters that were not yet covered. This will result in a snowball effect where more models mean more accurate estimates, which in turn will allow us to run new models even faster. The expansion of the data set is also not limited to the parameters that we covered in the initial data set, but we can expand our data set along previously unexplored parameters. However, it is important to keep some limitations in mind. Just as some models become unstable if the isothermal solution is too far away from the final solution, if we select parameters that are too far from the trained range (for example, an atmosphere composed fully of H_2O), it might result in a very poor initial estimate.

Our approach results in a speed up by a factor of 1.2 to 2, despite the very small training set used. Though this difference might not seem like a lot, since models still require hours to finish, we only provided an estimate of the thermal profiles. If a similar estimate is made of the chemical profile, the starting point will be even closer to the final result. In the normal set-up of a Kompot model, the chemistry is not updated at each step, as it is one of the more computationally intensive steps and large changes in both chemistry and thermal profile can lead to instabilities. Since the thermal profile is already close to the final result, we could optimise the interval at which chemistry, and particularly photochemistry, is calculated to reduce the total number of required iterations.

An advantage of using the output of a neural network as an initial solution rather than a final result is that if additional factors are added to the forward model, the estimations or previous Kompot models are still useful. For example, the network presented here was trained on a set of models before the addition of sulfur-bearing species to the network. The estimated thermal profile demonstrated for Venus could still be used as a starting point for a model affected by sulfur chemistry. This means that with each added factor, the estimate might become less accurate, but it will not become obsolete. Once the additional factors start to result in large deviations from the estimator, a new training set can be created using the initial estimates from the neural network or the previous library of models. The network can then be retrained on these updated models to account for the newly included physics or chemistry.

Lastly, an interesting application to work towards would be the use of the Kompot code in atmospheric retrievals. In its current state, the code still requires orders of magnitude too much time per model to be effectively used in retrievals. This could be achieved by finding more ways to accelerate the code (e.g. through GPU usage) or by expanding the cascading neural networks. If the neural networks achieve a high enough accuracy, they could be used for a rapid scan of the parameter space before using the forward model on the narrowed-down parameter space. Though this would once more require both a larger training set and the code to be faster.

Bibliography

Al-Refaie, A. F., Venot, O., Changeat, Q., & Edwards, B. 2022, FRECKLL: Full and Reduced Exoplanet Chemical Kinetics distiLLed

Alcott, L. J., Walton, C., Planavsky, N. J., Shorttle, O., & Mills, B. J. W. 2024, Nat. Geosci., 17, 458

Amerstorfer, U. V., Gröller, H., Lichtenegger, H., et al. 2017, Journal of Geophysical Research: Planets, 122, 1321

Ardévol Martínez, F., Min, M., Huppenkothen, D., Kamp, I., & Palmer, P. I. 2024, Astronomy and Astrophysics, 681, L14

Avice, G., Parai, R., Jacobson, S., et al. 2022, Space Sci Rev, 218, 60

Barabash, S., Fedorov, A., Sauvaud, J. J., et al. 2007, Nature, 450, 650

Barstow, J. K. & Heng, K. 2020, Space Sci Rev, 216, 82

Barstow, J. K. & Irwin, P. G. J. 2016, Monthly Notices of the Royal Astronomical Society, 461, L92

Bauer, S. J. & Lammer, H. 2004, Planetary Aeronomy (Springer)

Baumeister, P., Tosi, N., Brachmann, C., Grenfell, J. L., & Noack, L. 2023, Astronomy and Astrophysics, 675, A122

Benner, S. 2010a, in Water and Life: The Unique Properties of H2O (CRC Press), 157–175

Benner, S. A. 2010b, Astrobiology, 10, 1021

Benner, S. A., Ricardo, A., & Carrigan, M. A. 2004, Current Opinion in Chemical Biology, 8, 672

Boro Saikia, S., Jin, M., Johnstone, C. P., et al. 2020, A&A, 635, A178

Buccino, A. P., Lemarchand, G. A., & Mauas, P. J. D. 2006, Icarus, 183, 491

Cadieux, C., Doyon, R., MacDonald, R. J., et al. 2024, The Astrophysical Journal, 970, L2

Carr, M. H. & Head, J. W. 2010, Earth and Planetary Science Letters, 294, 185

Catling, D. C., Glein, C. R., Zahnle, K. J., & McKay, C. P. 2005, Astrobiology, 5, 415

Catling, D. C. & Kasting, J. F. 2017, Atmospheric Evolution on Inhabited and Lifeless Worlds, 1st edn. (Cambridge University Press)

Charbonneau, D., Brown, T. M., Noyes, R. W., & Gilliland, R. L. 2002, The Astrophysical Journal, 568, 377

Chatterjee, R. D. & Pierrehumbert, R. T. 2024, Novel Physics of Escaping Secondary Atmospheres May Shape the Cosmic Shoreline

Claire, M. W., Sheets, J., Cohen, M., et al. 2012, Astrophysical Journal, 757, 95

Cleland, C. E. & Chyba, C. F. 2002, Orig Life Evol Biosph, 32, 387

Corsetti, F. A., Awramik, S. M., & Pierce, D. 2003, Proceedings of the National Academy of Sciences, 100, 4399

Council, N. R. 2007, The Limits of Organic Life in Planetary Systems (Washington, D.C.: National Academies Press)

Csizmadia, S., Pasternacki, T., Dreyer, C., et al. 2013, A&A, 549, A9

Damiano, M., Bello-Arufe, A., Yang, J., & Hu, R. 2024, The Astrophysical Journal, 968, L22

de Wit, J., Wakeford, H. R., Gillon, M., et al. 2016, Nature, 537, 69

Demory, B.-O., Gillon, M., Madhusudhan, N., & Queloz, D. 2016, Monthly Notices of the Royal Astronomical Society, 455, 2018

Diamond-Lowe, H., Berta-Thompson, Z., Charbonneau, D., & Kempton, E. M. R. 2018, The Astronomical Journal, 156, 42

do Amaral, L. N. R., Barnes, R., Segura, A., & Luger, R. 2022, ApJ, 928, 12

Donahue, T. M., Hoffman, J. H., Hodges, R. R., & Watson, A. J. 1982, Science, 216, 630

Dorn, C. & Lichtenberg, T. 2021, The Astrophysical Journal, 922, L4

Dorn, C., Noack, L., & Rozel, A. B. 2018, A&A, 614, A18

Drążkowska, J., Bitsch, B., Lambrechts, M., et al. 2023, in ASP Conference Series, Vol. 534, Protostars and Planets VII (eprint: arXiv:2203.09759: San Francisco: Astronomical Society of the Pacific), 717

Ealy, J. N., Schlieder, J. E., Komacek, T. D., & Gilbert, E. A. 2024, The Astronomical Journal, 168, 173

Edwards, B., Changeat, Q., Mori, M., et al. 2021, The Astronomical Journal, 161, 44

Edwards, B., Changeat, Q., Tsiaras, A., et al. 2023, Astrophys. J. Suppl. Ser., 269, 31

Eistrup, C., Walsh, C., & van Dishoeck, E. F. 2018, A&A, 613, A14

Elkins-Tanton, L. T. 2008, Earth and Planetary Science Letters, 271, 181

Erkaev, N. V., Lammer, H., Odert, P., et al. 2013, Astrobiology, 13, 1011

Feroz, F. & Hobson, M. P. 2008, Monthly Notices of the Royal Astronomical Society, 384, 449

Fichtinger, B., Güdel, M., Mutel, R. L., et al. 2017, Astronomy and Astrophysics, 599, A127

Fontenla, J. M., Linsky, J. L., Garrison, J., et al. 2016, ApJ, 830, 154

Franz, H. B., Trainer, M. G., Malespin, C. A., et al. 2017, Planetary and Space Science, 138, 44

Frick, L., Mac Neela, J. P., & Wolfenden, R. 1987, Bioorganic Chemistry, 15, 100

Fu, H., Jacobsen, S. B., & Sedaghatpour, F. 2023, Commun Earth Environ, 4, 1

Fulton, B. J. & Petigura, E. A. 2018, The Astronomical Journal, 156, 264

Gardner, J. P., Mather, J. C., Abbott, R., et al. 2023, Publications of the Astronomical Society of the Pacific, 135, 068001

Gardner, J. P., Mather, J. C., Clampin, M., et al. 2006, Space Science Reviews, 123, 485

Gebauer, S., Grenfell, J. L., Lammer, H., et al. 2020, Astrobiology, 20, 1413

Gebhard, T. D., Angerhausen, D., Konrad, B. S., et al. 2024, Astronomy and Astrophysics, 681, A3

Gillon, M., Triaud, A. H., Demory, B. O., et al. 2017, Nature 2017 542:7642, 542, 456

Gonzalez, G., Brownlee, D., & Ward, P. 2001, Icarus, 152, 185

Goodfellow, I. J., Pouget-Abadie, J., Mirza, M., et al. 2014, Generative Adversarial Networks

Grasser, N., Kislyakova, K., Scherf, M., Lammer, H., & Van Looveren, G. 2023, Earth and Planetary Science Letters, 623, 118442

Greene, T. P., Bell, T. J., Ducrot, E., et al. 2023, Nature, 618, 39

Gronoff, G., Arras, P., Baraka, S., et al. 2020, Journal of Geophysical Research: Space Physics, 125, e2019JA027639

Grundnig, T. & Van Looveren, G. in prep.

Guillot, T. 2010, A&A, 520, A27

Guimond, C. M., Noack, L., Ortenzi, G., & Sohl, F. 2021, Physics of the Earth and Planetary Interiors, 320, 106788

Gunell, H., Maggiolo, R., Nilsson, H., et al. 2018, Astronomy & Astrophysics, 614, L3

Hart, M. H. 1979, Icarus, 37, 351

Hazra, G., Vidotto, A. A., Carolan, S., Villarreal D'Angelo, C., & Manchester, W. 2022, Monthly Notices of the Royal Astronomical Society, 509, 5858

Heldmann, J. L., Toon, O. B., Pollard, W. H., et al. 2005, Journal of Geophysical Research: Planets, 110

Henning, W. G., O'Connell, R. J., & Sasselov, D. D. 2009, ApJ, 707, 1000

Herbort, O., Woitke, P., Helling, Ch., & Zerkle, A. 2020, Astronomy and Astrophysics, 636, A71

Herbort, O., Woitke, P., Helling, Ch., & Zerkle, A. L. 2022, Astronomy and Astrophysics, 658, A180

Hopkins, M., Harrison, T. M., & Manning, C. E. 2008, Nature, 456, 493

Horinouchi, T., Hayashi, Y.-Y., Watanabe, S., et al. 2020, Science, 368, 405

Howard, W. S., Kowalski, A. F., Flagg, L., et al. 2023, Characterizing the Near-infrared Spectra of Flares from TRAPPIST-1 During JWST Transit Spectroscopy Observations

Hu, R., Bello-Arufe, A., Zhang, M., et al. 2024, Nature, 630, 609

Huang, S.-S. 1959, Publications of the Astronomical Society of the Pacific, 71, 421

Huebner, W. F. & Mukherjee, J. 2015, Planetary and Space Science, 106, 11

Jackson, B., Barnes, R., & Greenberg, R. 2008, Monthly Notices of the Royal Astronomical Society, 391, 237

Jakosky, B. M., Brain, D., Chaffin, M., et al. 2018, Icarus, 315, 146

Johnson, R. E., Schnellenberger, D., & Wong, M. C. 2000, Journal of Geophysical Research: Planets, 105, 1659

Johnstone, C. P. 2020, The Astrophysical Journal, 890, 79

Johnstone, C. P., Bartel, M., & Güdel, M. 2021a, A&A, 649, 96

Johnstone, C. P., Güdel, M., Lammer, H., & Kislyakova, K. G. 2018, Astronomy & Astrophysics, 617, A107

Johnstone, C. P., Khodachenko, M. L., Lüftinger, T., et al. 2019, Astronomy & Astrophysics, 624, L10

Johnstone, C. P., Lammer, H., Kislyakova, K. G., Scherf, M., & Güdel, M. 2021b, Earth and Planetary Science Letters, 576, 117197

JWST Transiting Exoplanet Community Early Release Science Team, Ahrer, E.-M., Alderson, L., et al. 2023, Nature, 614, 649

Kasting, J. F. 1988, Icarus, 74, 472

Kasting, J. F. & Pollack, J. B. 1983, Icarus, 53, 479

Kasting, J. F., Whitmire, D. P., & Reynolds, R. T. 1993, Icarus, 101, 108

Kempton, E. M.-R. & Knutson, H. A. 2024, Reviews in Mineralogy and Geochemistry, 90, 411

Khodachenko, M. L., Alexeev, I., Belenkaya, E., et al. 2012, The Astrophysical Journal, 744, 70

Kislyakova, K. G., Güdel, M., Koutroumpa, D., et al. 2024, Nat. Astron., 8, 596

Kislyakova, K. G., Holmström, M., Lammer, H., Odert, P., & Khodachenko, M. L. 2014, Science, 346, 981

Kislyakova, K. G., Johnstone, C. P., Scherf, M., et al. 2020, JGRA, 125, e27837

Kislyakova, K. G., Noack, L., Johnstone, C. P., et al. 2017, Nature Astronomy, 1, 878

Kite, E. S. & Barnett, M. N. 2020, Proceedings of the National Academy of Sciences, 117, 18264

Kite, E. S., Mischna, M. A., Fan, B., et al. 2022, Science Advances, 8, eabo5894

Kite, E. S., Sneed, J., Mayer, D. P., & Wilson, S. A. 2017, Geophysical Research Letters, 44, 3991

Koll, D. D. B., Malik, M., Mansfield, M., et al. 2019, The Astrophysical Journal, 886, 140

Kopparapu, R., Ramirez, R. M., Schottelkotte, J., et al. 2014, The Astrophysical Journal Letters, 787, 29

Kopparapu, R., Wolf, E. T., Haqq-Misra, J., et al. 2016, ApJ, 819, 84

Kopparapu, R. K., Ramirez, R., Kasting, J. F., et al. 2013, The Astrophysical Journal, 765, 131

Kraus, D., Vorberger, J., Pak, A., et al. 2017, Nat Astron, 1, 606

Kreidberg, L., Koll, D. D. B., Morley, C., et al. 2019, Nature, 573, 87

Kreidberg, L., Line, M. R., Bean, J. L., et al. 2015, ApJ, 814, 66

Kreslavsky, M. A., Ivanov, M. A., & Head, J. W. 2015, Icarus, 250, 438

Krissansen-Totton, J., Garland, R., Irwin, P., & Catling, D. C. 2018, The Astronomical Journal, 156, 114

Kubyshkina, D., Fossati, L., Erkaev, N. V., et al. 2018, Astronomy and Astrophysics, 619, A151

Lammer, H., Sproß, L., Grenfell, J. L., et al. 2019, Astrobiology, 19, 927

Lammer, H., Zerkle, A. L., Gebauer, S., et al. 2018, The Astronomy and Astrophysics Review 2018 26:1, 26, 1

Lavie, B., Ehrenreich, D., Bourrier, V., et al. 2017, A&A, 605, L7

Leblanc, F., Chassefière, E., Johnson, R. E., et al. 2007, Planetary and Space Science, 55, 1069

Lebrun, T., Massol, H., Chassefière, E., et al. 2013, Journal of Geophysical Research: Planets, 118, 1155

Li, C.-H. 2022, Acta Geochim, 41, 650

Lichtenberg, T., Schaefer, L. K., Nakajima, M., & Fischer, R. A. 2023, Protostars and Planets VII, 534, 907

Lillis, R. J., Deighan, J., Fox, J. L., et al. 2017, Journal of Geophysical Research: Space Physics, 122, 3815

Limaye, S. S., Lebonnois, S., Mahieux, A., et al. 2017, Icarus, 294, 124

Loftus, K., Luo, Y., Fan, B., & Kite, E. S. 2024, Extreme Weather Variability on Hot Rocky Exoplanet 55 Cancri e Explained by Magma Temperature-Cloud Feedback

Lopes, R. M. C. & Spencer, J. R. 2007, Io After Galileo: A New View of Jupiter's Volcanic Moon (Springer Berlin, Heidelberg)

Lueber, A., Karchev, K., Fisher, C., et al. 2025, Near-Instantaneous Atmospheric Retrievals and Model Comparison with FASTER

Luque, R., Coy, B. P., Xue, Q., et al. 2024, A Dark, Bare Rock for TOI-1685 b from a JWST NIRSpec G395H Phase Curve

Lustig-Yaeger, J., Meadows, V. S., & Lincowski, A. P. 2019, The Astronomical Journal, 158, 27

Macintosh, B., Graham, J. R., Barman, T., et al. 2015, Science, 350, 64

Madhusudhan, N., Piette, A. A. A., & Constantinou, S. 2021, ApJ, 918, 1

Madhusudhan, N., Sarkar, S., Constantinou, S., et al. 2023, Carbon-Bearing Molecules in a Possible Hycean Atmosphere

Mak, M. T., Sergeev, D. E., Mayne, N., et al. 2024, Monthly Notices of the Royal Astronomical Society, 529, 3971

Marty, B., Zimmermann, L., Pujol, M., Burgess, R., & Philippot, P. 2013, Science, 342, 101

Mayer, L., Quinn, T., Wadsley, J., & Stadel, J. 2002, Science, 298, 1756

Mayor, M., Lovis, C., & Santos, N. C. 2014, Nature, 513, 328

Mayor, M. & Queloz, D. 1995, Nature, 378, 355

McKay, C. 2000, Geophysical Research Letters, 27, 2153

Miguel, Y. 2019, Monthly Notices of the Royal Astronomical Society, 482, 2893

Min, M., Dullemond, C. P., Kama, M., & Dominik, C. 2011, Icarus, 212, 416

Montmessin, F., Bertaux, J.-L., Quémerais, E., et al. 2006, Icarus, 183, 403

Moran, S. E., Stevenson, K. B., Sing, D. K., et al. 2023, ApJL, 948, L11

Morbidelli, A., Tsiganis, K., Crida, A., Levison, H. F., & Gomes, R. 2007, AJ, 134, 1790

Morley, C. V., Kreidberg, L., Rustamkulov, Z., Robinson, T., & Fortney, J. J. 2017, The Astrophysical Journal, 850, 121

Morrison, H., van Lier-Walqui, M., Fridlind, A. M., et al. 2020, Journal of Advances in Modeling Earth Systems, 12, e2019MS001689

Mugnai, L. V., Modirrousta-Galian, D., Edwards, B., et al. 2021, The Astronomical Journal, 161, 284

Nakayama, A., Ikoma, M., & Terada, N. 2022, The Astrophysical Journal, 937, 72

Nicholls, H., Hébrard, E., Venot, O., Drummond, B., & Evans, E. 2023, Monthly Notices of the Royal Astronomical Society, 523, 5681

Nishioka, T., Seki, K., Sakata, R., et al. 2023, Journal of Geophysical Research: Space Physics, 128, e2023JA031405

Nixon, C., Lorenz, R., Achterberg, R., et al. 2018, Planetary and Space Science, 155, 50

Noack, L., Rivoldini, A., & Van Hoolst, T. 2017, Physics of the Earth and Planetary Interiors, 269, 40

Öberg, K. I., Murray-Clay, R., & Bergin, E. A. 2011, The Astrophysical Journal, 743, L16

Ogihara, M., Kokubo, E., Suzuki, T. K., & Morbidelli, A. 2018, A&A, 615, A63

Öpik, E. J. 1963, Geophysical Journal, 7, 490

O'Rourke, J. G. & Korenaga, J. 2015, Icarus, 260, 128

Owen, J. E. & Wu, Y. 2016, ApJ, 817, 107

Patel, J. A., Brandeker, A., Kitzmann, D., et al. 2024, Astronomy and Astrophysics, 690, A159

Pfalzner, S., Steinhausen, M., & Menten, K. 2014, The Astrophysical Journal, 793, L34

Picone, J. M., Hedin, A. E., Drob, D. P., & Aikin, A. C. 2002, Journal of Geophysical Research: Space Physics, 107, SIA 15

Pierrehumbert, R. & Gaidos, E. 2011, ApJL, 734, L13

Piso, A.-M. A. & Youdin, A. N. 2014, The Astrophysical Journal, 786, 21

Pollack, J. B., Hubickyj, O., Bodenheimer, P., et al. 1996, Icarus, 124, 62

Presa, A., Driessen, F. A., & Vidotto, A. A. 2024, Monthly Notices of the Royal Astronomical Society, 534, 3622

Rackham, B. V., Apai, D., & Giampapa, M. S. 2018, ApJ, 853, 122

Ramirez, R. M. & Kaltenegger, L. 2014, The Astrophysical Journal, 797, L25

Raymond, S. N., O'Brien, D. P., Morbidelli, A., & Kaib, N. A. 2009, Icarus, 203, 644

Rimmer, P. B., Jordan, S., Constantinou, T., et al. 2021, Hydroxide Salts in the Clouds of Venus: Their Effect on the Sulfur Cycle and Cloud Droplet pH

Rogers, J. G., Schlichting, H. E., & Young, E. E. 2024, Fleeting but Not Forgotten: The Imprint of Escaping Hydrogen Atmospheres on Super-Earth Interiors

Rogers, L. A. 2015, ApJ, 801, 41

Ruiz-Mirazo, K., Peretó, J., & Moreno, A. 2004, Orig Life Evol Biosph, 34, 323

Sandu, A., Verwer, J. G., Blom, J. G., et al. 1997, Atmospheric Environment, 31, 3459

Schlaufman, K. C. 2018, The Astrophysical Journal, 853, 37

Schleich, S., Boro Saikia, S., Changeat, Q., et al. 2024, Astronomy and Astrophysics, 690, A336

Segura, A., Walkowicz, L. M., Meadows, V., Kasting, J., & Hawley, S. 2010, Astrobiology, 10, 751

Shematovich, V. I., Bisikalo, D. V., & Gérard, J. C. 1994, Journal of Geophysical Research: Space Physics, 99, 23217

Shematovich, V. I. & Marov, M. Y. 2018, Phys.-Usp., 61, 217

Simon, C., Lilensten, J., Moen, J., et al. 2007, Annales Geophysicae, 25, 661

Som, S. M., Buick, R., Hagadorn, J. W., et al. 2016, Nature Geosci, 9, 448

Stock, J. W., Kitzmann, D., Patzer, A. B. C., & Sedlmayr, E. 2018, Monthly Notices of the Royal Astronomical Society, 479, 865

Stofan, E. R., Elachi, C., Lunine, J. I., et al. 2007, Nature, 445, 61

Stökl, A., Dorfi, E. A., Johnstone, C. P., & Lammer, H. 2016, The Astrophysical Journal, 825, 86

Struve, O. 1952, The Observatory, 72, 199

Stüeken, E. E., Kipp, M. A., Koehler, M. C., et al. 2016, Astrobiology, 16, 949

Suissa, G., Wolf, E. T., kumar Kopparapu, R., et al. 2020, AJ, 160, 118

Swain, M. R., Vasisht, G., Tinetti, G., et al. 2008, ApJ, 690, L114

Tahseen, T. P. A., Mendonça, J. M., Yip, K. H., & Waldmann, I. P. 2024, Monthly Notices of the Royal Astronomical Society, 535, 2210

Tian, F., Kasting, J. F., Liu, H. L., & Roble, R. G. 2008, Journal of Geophysical Research: Planets, 113, 5008

Tokareva, A. 2024, Master's thesis, University of Vienna, Vienna

Tokareva, A., Van Looveren, G., & Güdel, M. in prep

Tóth, G., Sokolov, I. V., Gombosi, T. I., et al. 2005, Journal of Geophysical Research (Space Physics), 110, A12226

Toupance, G., Bossard, A., & Raulin, F. 1977, Origins Life Evol Biosphere, 8, 259

Trenberth, K. E. & Smith, L. 2005, Journal of Climate, 18, 864

Tsai, S.-M., Lee, E. K. H., Powell, D., et al. 2023, Nature, 617, 483

Tsai, S.-M., Malik, M., Kitzmann, D., et al. 2021, ApJ, 923, 264

Tsiganis, K., Gomes, R., Morbidelli, A., & Levison, H. F. 2005, Nature, 435, 459

Tu, L., Johnstone, C. P., Güdel, M., & Lammer, H. 2015, Astronomy & Astrophysics, 577, L3

Turbet, M., Fauchez, T. J., Sergeev, D. E., et al. 2022, Planet. Sci. J., 3, 211

Turner, J. D., Zarka, P., Grießmeier, J.-M., et al. 2021, Astronomy & Astrophysics, 645, A59

Tyler, R. H., Henning, W. G., & Hamilton, C. W. 2015, The Astrophysical Journal Supplement Series, 218, 22

Van Looveren, G., Boro Saikia, S., Herbort, O., et al. 2025, A&A, 694, A310

Van Looveren, G., Güdel, M., Boro Saikia, S., & Kislyakova, K. 2024, Astronomy and Astrophysics, 683, A153

Venot, O., Hébrard, E., Agúndez, M., Decin, L., & Bounaceur, R. 2015, Astronomy & Astrophysics, 577, A33

Venturini, J., Guilera, O. M., Haldemann, J., Ronco, M. P., & Mordasini, C. 2020, A&A, 643, L1

Vidal-Madjar, A., des Etangs, A. L., Désert, J.-M., et al. 2003, Nature, 422, 143

Vojtekova, A., Waldmann, I., Yip, K. H., et al. 2025, Monthly Notices of the Royal Astronomical Society, 538, 1690

Vorobyov, E. I., McKevitt, J., Kulikov, I., & Elbakyan, V. 2023, Astronomy and Astrophysics, 671, A81

Wahl, S. M., Hubbard, W. B., Militzer, B., et al. 2017, Geophysical Research Letters, 44, 4649

Wakelam, V., Herbst, E., Loison, J. C., et al. 2012, The Astrophysical Journal Supplement Series, 199, 21

Wang, Y.-C., Luhmann, J. G., Leblanc, F., et al. 2014, Journal of Geophysical Research: Planets, 119, 93

Wheatley, P. J., Louden, T., Bourrier, V., Ehrenreich, D., & Gillon, M. 2017, Monthly Notices of the Royal Astronomical Society: Letters, 465, L74

Wilson, D. J., Froning, C. S., Duvvuri, G. M., et al. 2021, ApJ, 911, 18

Withers, P. & Smith, M. D. 2006, Icarus, 185, 133

Woitke, P., Helling, Ch., Hunter, G. H., et al. 2018, Astronomy and Astrophysics, 614, A1

Wolf, E. T. & Toon, O. B. 2015, Journal of Geophysical Research: Atmospheres, 120, 5775

Wood, B. E., Müller, H.-R., Redfield, S., & Edelman, E. 2014, Astrophys. J., 781, L33

Wu, X. & Zhang, X. 2017, Responses to Critiques on Machine Learning of Criminality Perceptions (Addendum of arXiv:1611.04135)

Yang, J., Boué, G., Fabrycky, D. C., & Abbot, D. S. 2014, ApJL, 787, L2

Yang, J., Cowan, N. B., & Abbot, D. S. 2013, The Astrophysical Journal, 771, L45

Yang, J., Ji, W., & Zeng, Y. 2020, Nature Astronomy, 4, 58

Yip, K. H., Waldmann, I., Morvan, M., et al. 2023, in AAS/Division for Planetary Sciences Meeting Abstracts #55, Vol. 55, 109.02

Yoshida, T. & Kuramoto, K. 2020, Icarus, 345, 113740

Young, E. D., Shahar, A., & Schlichting, H. E. 2023, Nature, 616, 306

Yu, G. & Jacobsen, S. B. 2011, Proceedings of the National Academy of Sciences, 108, 17604

Zahnle, K. J. & Catling, D. C. 2017, ApJ, 843, 122

Zhang, M., Hu, R., Inglis, J., et al. 2024, ApJL, 961, L44

Zieba, S., Kreidberg, L., Ducrot, E., et al. 2023, Nature

Zsom, A., Seager, S., de Wit, J., & Stamenković, V. 2013, ApJ, 778, 109

Acknowledgments

The authors acknowledge the support of the Austrian Research Promotion Agency (FFG) Project 873677 "CONEX". The project was partially funded by the European Union (ERC, EASE, 101123041). Views and opinions expressed are, however, those of the author(s) only and do not necessarily reflect those of the European Union or the European Research Council Executive Agency. Neither the European Union nor the granting authority can be held responsible for them. The project benefited from the Chicago-Vienna International Grant Program titled "The Atmospheric Evolution of Mars: Combining Geological and Astrophysical Perspectives". The results of this work were partially achieved at the Vienna Scientific Cluster (VSC). We acknowledge the Community Coordinated Modeling Center (CCMC) at Goddard Space Flight Center for the use of the Instant Run System of the NRLMSIS model, https://kauai.ccmc.gsfc.nasa.gov/instantrun/nrlmsis/.

∼

Welcome to the behind-the-scenes of this thesis, where I get to let my ramblings run wild and be sappy about the past three and a half years.

First, I want to thank my three supervisors: Manuel, Sudeshna, and Kristina (no need for silly titles here). I am very grateful that you have given me, and keep on giving me, the opportunity to prove my worth as a researcher. You were always ready to give support when I needed it, even with the complicated situations of a sabbatical and parental leave. All three of you have also always looked after me, ensuring that I take the right opportunities. You made sure that I am as prepared as possible to continue in research whilst having realistic expectations of this career choice. For all this and likely many other things that I indubitably am forgetting, I am very grateful. (P.S. Sorry for making you read this thesis over and over, even though you are all already swamped in work.)

I would like to thank the colleagues I have met along the way who have rapidly become good friends. You have made me feel welcome and at home, which is invaluable when moving to a new country. I know it sounds vague and generic, but I do not wish to waffle on for pages on end (especially since the PDF is now exactly 100 pages, feels good). Perhaps I will do something unusual (me doing something unusual must be shocking) and send around individual thank-you letters to people. Here, I do still want to thank Yanina and Simon for the fun times and the support you have given me throughout the bad ones as well. May our *three-person-group-chat* continue to flourish with random knowledge and silly poppycock.

Of course, I cannot write thanks without addressing my family. Without your support throughout the years, I would never have been able to reach this point, both in the sense of my studies and of my life. Thank you for always lending me your ears, often for hours on end. Thank you for sharing your interests, passions and knowledge with me, preventing me from becoming a one-trick pony. In essence, thank you for being you and allowing me to be me. I love you all a lot.

To conclude, I wish to say that even though I had planned on getting away with a simple cumulative thesis, I am happy to have written this work. The last couple of months have been more intense than what could be considered healthy, but in this time, I have taken a second look at both my own work and that of the community. Writing this thesis has been a rewarding experience. But for now, I quoth

"Nevermore".

" Step.
Just once.
Marking the start
of a unique journey
towards horizons beyond your view.

Go.
Just try.
Into the unknown
by strange new paths
into experiences untried and new.

Stay.
Just briefly.
In this moment
and this other place
considering this change long overdue.

Become.
Just be.
Who you are
and want to be
and know to be true."